DECEMBER 1966
VOLUME XXVII
NUMBER 4

RCA REVIEW

PRINTED IN U.S.A.

RCA REVIEW, published quarterly in March, June, September, and December by RCA Laboratories, Radio Corporation of America, Princeton, New Jersey 08540. Entered as second class matter July 3, 1950 under the Act of March 3, 1879. Second-class postage paid at Princeton, New Jersey, and at additional mailing offices. Subscription price in the United States and Canada: one year \$2.00, two years \$3.50, three years \$4.50; in other countries, one year \$2.40, two years \$4.30, three years \$5.70. Single copies up to five years old \$1.00. For copies more than five years old, contact Walter J. Johnson, Inc., 111 Fifth Ave., New York, N. Y. 10003.

RCA REVIEW

a technical journal

Published quarterly by
RCA LABORATORIES
in cooperation with all subsidiaries and divisions of
RADIO CORPORATION OF AMERICA

VOLUME XXVII DECEMBER 1966 NUMBER 4

CONTENTS

RCA REVIEW is regularly abstracted and indexed by *Abstracts of Photographic Science and Engineering Literature, Applied Science and Technology Index, Bulletin Signalétique des Télecommunications, Chemical Abstracts, Electronic and Radio Engineer, Mathematical Reviews, and Science Abstracts* (I.E.E.-Brit.).

RCA REVIEW

BOARD OF EDITORS

Chairman
R. S. Holmes
RCA Laboratories

A. A. Barco
RCA Laboratories

E. D. Becken
RCA Communications, Inc.

G. H. Brown
Radio Corporation of America

A. L. Conrad
RCA Service Company

E. W. Engstrom
Radio Corporation of America

A. N. Goldsmith
Honorary Vice President, RCA

J. Hillier
RCA Laboratories

E. C. Hughes
Electronic Components and Devices

E. O. Johnson
Electronic Components and Devices

E. A. Laport
Radio Corporation of America

H. W. Leverenz
RCA Laboratories

H. R. Lewis
RCA Laboratories

G. F. Maedel
RCA Institutes, Inc.

L. S. Nergaard
RCA Laboratories

H. F. Olson
RCA Laboratories

K. H. Powers
RCA Laboratories

J. A. Rajchman
RCA Laboratories

F. D. Rosi
RCA Laboratories

D. F. Schmit
Radio Corporation of America

L. A. Shotliff
RCA International Division

C. P. Smith
RCA Laboratories

W. M. Webster
RCA Laboratories

Secretary
C. C. Foster
RCA Laboratories

Republication and Translation

Original papers published herein may be referenced or abstracted without further authorization provided proper notation concerning authors and source is included. All rights of republication, including translation into foreign languages, are reserved by RCA Review. Requests for republication and translation privileges should be addressed to *The Manager*.

THE HOLOGRAM — PROPERTIES AND APPLICATIONS

BY

E. G. RAMBERG

RCA Laboratories
Princeton, N. J.

***Summary**—A hologram is the record of an interference pattern between the temporally coherent light wave from an object and a reference beam derived from the same source, i.e., with the same temporal coherence. When a similar reference beam is incident on the hologram, it is diffracted so as to give rise to (1) the original object wave, thus producing a faithful three-dimensional virtual image, and, (2) under appropriate conditions, to a wave converging to a mirror image of the object, thus forming a depth-inverted three-dimensional real image.*

This paper describes various forms of plane and three-dimensional holograms and interprets their properties in terms of Fresnel–Kirchoff diffraction theory. It indicates the rather stringent requirements to be fulfilled in the recording of holograms as well as the much smaller demands to be met in image reconstruction. Some applications of holography are discussed briefly.

INTRODUCTION

ACCORDING to the originator of the term, Dennis Gabor,[1] a hologram is a record that "contains the *total* information for reconstructing (an) object, which can be two-dimensional or three-dimensional." The hologram record is a recording of the standing-wave pattern formed by temporally coherent light from the object to be reproduced and from a reference source. Light from an identical reference source incident on the developed record gives rise to a diffracted wave identical in amplitude and phase distribution with the original wave from the object. Thus, with illumination from an appropriate reference beam, the object can either be photographed or viewed directly by looking through the hologram.

Gabor demonstrated the feasibility of holography in 1948,[2] using pinholes illuminated by filtered radiation from a mercury arc to provide the required coherence. His primary objective was, however, to over-

---

[1] D. Gabor, "Microscopy by Reconstructed Wave-fronts," *Proc. Roy. Soc.* (London), Vol. A197, p. 454, July 1949.

[2] D. Gabor, "A New Microscopic Principle," *Nature*, Vol. 161, p. 777, May 15, 1948.

come the limitations imposed by spherical aberration on the resolution of the electron microscope.[2,3] In essence, the procedure suggested by him was to place the specimen in front of a fine electron probe formed by electron lenses with their inherent aberration and to record an electron hologram on a plate placed at some distance from the specimen. This was then to be scaled up in the ratio of the light wavelength to the electron wavelength and to be illuminated by a reference source of light with the same aberration as the electron source, scaled up in the same proportion. The specimen should then be visible through the hologram (scaled up in the ratio of the wavelengths or by a factor of about 100,000) in a location corresponding to the original specimen position.

Efforts by Haine and Mulvey[4] to exceed the resolution of the conventional electron microscope by a refined version of this technique were defeated by excessive demands on the coherence of the electron source and the stability of the entire system, as well as by difficulties in reconstruction. In attempts by Baez[5] and El Sum[6] to utilize holography for x-ray microscopy, even greater difficulties were encountered. However, the advent of the laser, providing light sources of extraordinary monochromaticity and coherence length, gave new impetus to the field of holography. The introduction of a separate, oblique reference beam and of diffuse illumination of the object (or diffuse scattering by the object) by Leith and Upatnieks[7,8] were particularly important steps in extending the potentialities of holography.

The early work of Gabor was concerned entirely with plane holograms, i.e., records that could be regarded as planar sections through the standing-wave pattern. Three-dimensional holograms, formed in a recording medium with a depth large compared to the separation of the surfaces of constructive or destructive interference, have quite

---

[3] D. Gabor, "Microscopy by Reconstructed Wave Fronts: II," *Proc. Phys. Soc.* (London), Vol. B64, p. 449, June 1951.

[4] M. E. Haine and T. Mulvey, "The Formation of the Diffraction Image with Electrons in the Gabor Diffraction Microscope," *Jour. Opt. Soc. Amer.*, Vol. 42, p. 763, Oct. 1952.

[5] A. V. Baez, "A Study in Diffraction Microscopy with Special Reference to X-rays," *Jour. Opt. Soc. Amer.*, Vol. 42, p. 756, Oct. 1952.

[6] H. M. A. El-Sum, *Reconstructed Wavefront Microscopy*, Ph.D. Thesis, Stanford Univ., Nov. 1952.

[7] E. N. Leith and J. Upatnieks, "Wavefront Reconstruction with Continuous-tone Objects," *Jour. Opt. Soc. Amer.*, Vol. 53, p. 1377, Dec. 1963.

[8] J. Upatnieks and E. N. Leith, "Lensless, Three-dimensional Photography by Wavefront Reconstruction," *Jour. Opt. Soc. Amer.*, Vol. 54, p. 579, April 1964.

distinctive properties, as pointed out by Denisyuk[9] and investigated in more detail by Van Heerden.[10] It will be convenient to consider these two types of holograms separately.

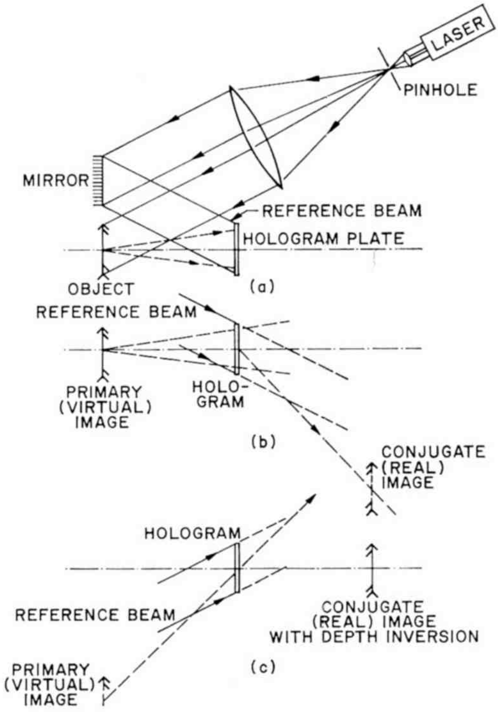

Fig. 1—Fresnel hologram: (a) recording of hologram, (b) reconstruction of aberration-free virtual image, and (c) reconstruction of aberration-free real image with depth inversion.

PLANE HOLOGRAMS

Figure 1 illustrates the recording of a plane hologram and the reconstruction of an image by means of it. In Figure 1(a) the radiation from a laser, after passing through a pinhole diaphragm, falls partly on a mirror that directs it onto the hologram plate and partly on a diffusely reflecting object whose image is to be recorded. The hologram pattern is the interference pattern that the directly reflected

---

[9] Yu. N. Denisyuk, "Photographic Reconstruction of the Optical Properties of an Object in Its Own Scattered Radiation Field," *Soviet Physics—Doklady*, Vol. 7, p. 543, Dec. 1962.

[10] P. J. van Heerden, "Theory of Optical Information Storage in Solids," *Appl. Optics*, Vol. 2, p. 393, April 1963.

reference beam and the diffusely reflected radiation from the object form on the hologram plate, which is commonly a high-resolution photographic plate. After development, the hologram plate may be replaced in its original position (Figure 1(b)), with the object removed from the path of the laser beam. Light diffracted by the hologram will then permit a viewer looking through the hologram to observe a perfect image of the object. Furthermore, if the hologram is large enough, this image, when viewed from different directions, has the three-dimensional aspect of the original object.

In addition to the primary "virtual image" of the object behind the hologram, the observer will see a real image, the "conjugate image," on the other side of the reference beam, suspended in space in front of the hologram. This conjugate image will, in general, exhibit lack of sharpness, and some displacement will be observed with a change in the viewing direction. However, if we change the position of the reference source so that the light path of the reference beam forms a mirror image, with respect to the hologram plane, of the reference-beam light path during recording, a perfect real three-dimensional mirror image of the object appears in front of the hologram (along with an imperfect virtual image on the other side of the reference beam), as shown in Figure 1(c). This conjugate real image differs from any image formed by lenses or mirrors in that the dimensions in a direction perpendicular to the hologram are inverted. Looking at it we see, e.g., the illuminated surface of a human face from the inside. It is possible, however, to generate a three-dimensional real image without depth inversion by forming a second hologram from the conjugate image formed by a first one and observing the conjugate image formed by the second hologram (see Figure 2), as demonstrated by H. J. Gerritsen* and by Rotz and Friesem.[11] It should be noted that both the primary (virtual) and conjugate (real) images are completely aberration-free for the same conditions of illumination only if the reference beam is parallel and has normal incidence on the hologram plate.

TRANSPARENCY HOLOGRAM

A hologram can also be prepared in which the object is a transparency transmitting the laser beam, without any diffusing element in the path of the object illumination. This situation, with parallel

---

* Private communication.

[11] F. B. Rotz and A. A. Friesem, "Holograms with Nonpseudoscopic Real Images," *Appl. Phys. Letters*, Vol. 8, p. 146, 1966.

reference beam, is illustrated in Figure 3. The holograms formed in this fashion and the images reconstructed from them exhibit essential differences from those for a diffusely reflecting or diffusely illuminated object. If we view the images directly, we see only a tiny portion at a time, corresponding to the intersection with the image plane of the cone extending from the (infinitely) distant point source to the pupil of the observer's eye, just as we would in observing the original transparency with parallel illumination. A more important distinction is that in the hologram prepared with a diffusely emitting object, light from any part of the object is equally distributed to all parts of the hologram, whereas in the transparency hologram this is not the case. As a consequence, any part of the hologram of a diffusely emitting object can serve to reproduce the entire image (albeit with resolution limited by diffraction in the same manner as in the image formed by a lens of the same size as the hologram and at the same distance from

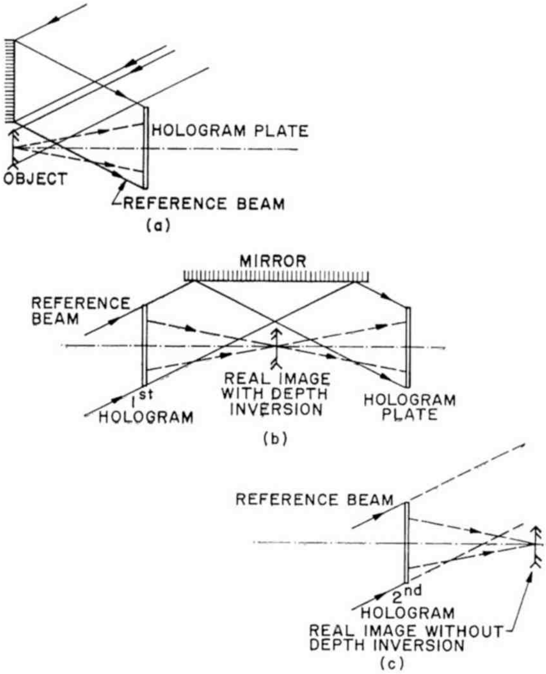

Fig. 2—Reconstruction of real image without depth inversion (H. J. Gerritsen): (a) recording of 1st hologram, (b) recording of 2nd hologram, and (c) reconstruction of real image without depth inversion.

the image as the hologram). With a transparency hologram, removal of a portion of the hologram results in the removal of a corresponding portion of the image. Thus damage to a portion of the hologram of a diffusely reflecting object has only a minor effect (similar to that of inflicting similar damage to the surface of a lens forming an image) in reducing the brightness and contrast of the image; for a transparency hologram, damage and dust on the hologram (as well as imperfections in other portions of the optical path) produce undesirable image distortions.

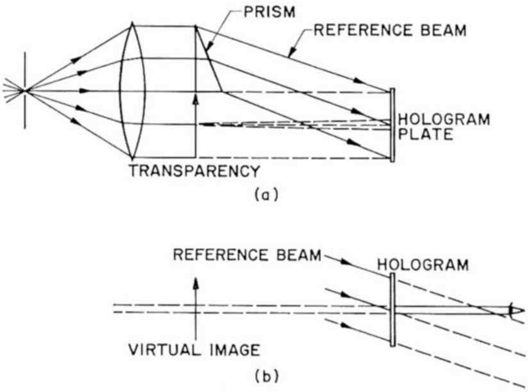

Fig. 3—Hologram of transparency prepared with undiffused illumination: (a) recording and (b) viewing of virtual image.

On the other hand, images formed by transparency holograms do not exhibit the granular appearance known as "speckle," observed, e.g., in the spot formed by a laser beam falling on a diffusing surface. The apparent dimensions of the speckle grain lie close to the diffraction limit of resolution of the imaging system. For direct observation of hologram images of diffusing objects, this limit is established by the pupil of the eye and its distance from the image; the speckle is hence invariably prominent. This image speckle may be rendered insignificant, however, by increasing the aperture subtended by the hologram in the image plane until the effective speckle dimensions are smaller than the resolution capacity of the recording medium or the observer.

FOURIER TRANSFORM HOLOGRAMS

We have already noted that the reference beam may be parallel or may converge or diverge. The hologram formed by a nearby object and a parallel reference beam has been designated as a Fresnel hologram. There are two other special conditions of recording and reconstruction which merit mention. One of these results in a "Fraunhofer hologram"[12] (see Figure 4); the reference source and (plane) object are placed in the focal plane of a lens and thus, effectively, at an infinite distance from the hologram plate. In the reconstruction, both the primary and the conjugate images are formed in the focal plane of a second lens, magnified or reduced by a factor equal to the ratio of the focal lengths of the two lenses.

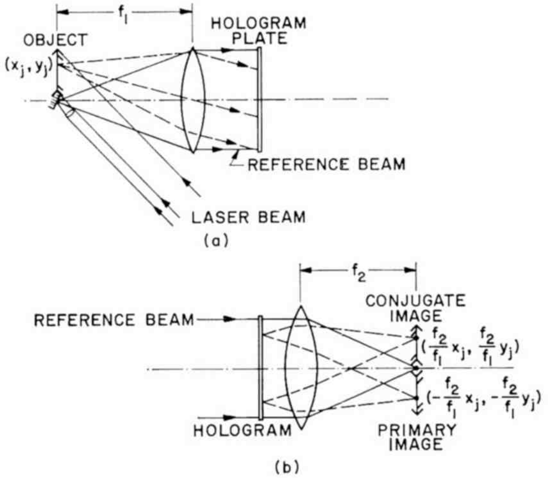

Fig. 4—Fraunhofer hologram: (a) recording and (b) image reconstruction.

The parallel light beam originating from a point (x_j, y_j) of the object forms an interference pattern with the parallel reference beam (assumed perpendicular to the hologram plane). This pattern, in the hologram plane, corresponds to a sinusoidal intensity variation with a space period

$$\frac{\lambda}{\sin \theta_j} = \frac{\lambda f_1}{\sqrt{x_j^2 + y_j^2}} \tag{1}$$

and an azimuthal direction

---

[12] E. N. Leith and J. Upatnieks, "Wavefront Reconstruction with Diffused Illumination and Three-dimensional Objects," *Jour. Opt. Soc. Amer.*, Vol. 55, p. 1295, 1965.

$$\phi_j = \arctan\ (y_j/x_j). \qquad (2)$$

θ_j is the angle of incidence on the hologram plane of the beam from the point (x_j, y_j). Thus, every object point in a half-plane is represented uniquely on the hologram by a two-dimensional Fourier component whose amplitude corresponds to the amplitude of the light wave emitted by the point in question. The hologram pattern is thus a Fourier transform of the object pattern. This is also true, to a close approximation, if the point source of the reference beam is placed in the plane of the object and the lens is omitted (see Figure 5). The differences in the direction cosines of the interfering beams for the x- and y-direction, which determine the orientation and spacing of the interference fringes in the hologram plane, are very nearly constant over the hologram surface, thus justifying the designation of such a hologram as a "Fourier-transform hologram".[13]

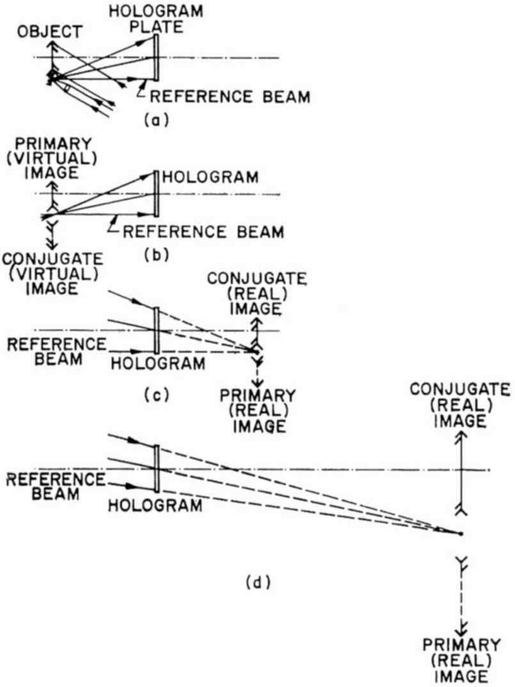

Fig. 5—Fourier-transform hologram: (a) recording, (b) reconstruction of aberration-free virtual image, (c) reconstruction of aberration-free real image, and (d) reconstruction of magnified real image.

---

[13] G. W. Stroke, D. Brumm, and A. Funkhouser, "Three-dimensional Holography with 'Lensless' Fourier-transform Holograms and Coarse P/N Polaroid Film," *Jour. Opt. Soc. Amer.*, Vol. 55, p. 1327, Oct. 1965.

With such a Fourier-transform hologram, an aberration-free primary virtual image is formed when the reconstruction reference beam diverges from the recording reference source (see Figure 5(b)) and a conjugate real image is formed when the reference beam converges at a mirror image of the reference source (see Figure 5(c)). Furthermore, with the reference source right at the edge of the image field, the angles between the interfering reference rays and object rays are less (and hence the spacings of the hologram patterns to be recorded larger) than for any other disposition of the reference beam that permits separation of the reference beam from the image field. Finally, if the reference beam during reconstruction is caused to converge at a point $(Mx_0, My_0, -Mz_0)$, assuming the reference source during recording to be located at (x_0, y_0, z_0), a real image of the object magnified by a factor M will be formed in the plane $z = -Mz_0$ (see Figure 5(d)). This image will be free from distortion, but will not be stigmatic. Some idea of the quality of the image can be inferred from the fact that, for large M, the maximum number of lines that can be resolved in the image is of the order of $(z_0/\lambda)^{1/2}$, where λ is the wavelength of the light used. This is realized if the half-angle subtended by the image field at the hologram is

$$\beta \geqq 0.4\ (\lambda/z_0)^{1/4} \text{ radian.} \tag{3}$$

The hologram itself should then be so dimensioned that the half angle subtended by the hologram at the object is, approximately,

$$\theta = \frac{0.4}{\beta}\ (\lambda/z_0)^{1/2} \text{ radian.} \tag{4}$$

These results are obtained by balancing the image diffusion by diffraction (which decreases with increasing hologram size) against image diffusion by geometrical aberrations (which has the opposite trend). It is thus clear that, by using long distances between the object and the hologram, it is possible to utilize holography for high-resolution lensless microscopy.[14]

MATHEMATICAL ANALYSIS

It is instructive to give some mathematical basis for the phenomena observed in holography. If we call the plane of the hologram plate

---

[14] E. N. Leith and J. Upatnieks, "Microscopy by Wavefront Reconstruction," *Jour. Opt. Soc. Amer.*, Vol. 55, p. 569, May 1965.

the x, y plane, we can describe the amplitude in this plane of the lightwave emitted by the object by

$$B(x,y)\exp\{j[\phi(x,y)-\omega t]\} \tag{5}$$

and that of the reference beam by

$$A(x,y)\exp\{j[\phi_r(x,y)-\omega t]\}. \tag{6}$$

The amplitude functions $B(x,y)$ and $A(x,y)$ and the phase functions $\phi(x,y)$ and $\phi_r(x,y)$ are here real functions.* Furthermore $A(x,y)$ is a slowly variable function (it is a constant for a plane reference wave, but for a spherical wave it varies as the reciprocal of distance from the reference source to different points on the hologram). The reference wave may also be a distorted spherical wave, as formed by a lens with geometrical aberrations. The amplitude function of the object wave, $B(x,y)$, is materially smaller than $A(x,y)$.

The exposure, or intensity integrated over the time, on the hologram plate will be

$$\begin{aligned} It &= \text{const}\,[A^2+B^2+2AB\cos(\phi-\phi_r)] \\ &= \text{const}\,[A^2+B^2+AB(\exp\{j(\phi-\phi_r)\}+\exp\{-j(\phi-\phi_r)\}]. \end{aligned} \tag{7}$$

We shall assume that the density D on the developed hologram plate is given by

$$\frac{dD}{d\log(It)} = -\frac{d\log T}{d\log(It)} = \gamma, \quad T=\overline{T}\left(\frac{It}{\overline{It}}\right)^{-\gamma}. \tag{8}$$

Here T is the transmission and γ is the "gamma" of the plate, which depends both on the plate itself and on its development. The amplitude transmission T_A, which is the square root of the transmission, is thus given by

$$T_A = \text{const}\,[A^2+B^2+AB(\exp\{j(\phi-\phi_r)\}+\exp\{-j(\phi-\phi_r)\}]^{-\gamma/2}$$

---

* This scalar treatment does not take account of polarization effects. However, it is always possible to split the object wave into two components, one with the electric vector in the plane containing the electric vector and the direction of propagation of the reference ray and the other with the electric vector perpendicular to this plane. Only the first component contributes to the interference pattern on the hologram and hence to the reconstructed image.

$$= \text{const}\,[A^2+B^2]^{-\gamma/2}\left[1-\frac{\gamma}{2}\frac{AB}{A^2+B^2}\left(\exp\{j(\phi-\phi_r)\}+\exp\{-j(\phi-\phi_r)\}\right)\right.$$
$$\left.+\frac{\gamma(\gamma+2)}{8}\left(\frac{AB}{A^2+B^2}\right)^2\left(\exp\{j(\phi-\phi_r)\}+\exp\{-j(\phi-\phi_r)\}\right)^2+\cdots\right]$$

For picture reconstruction we now let a reference wave

$$A'\exp\{j[\phi_r'(x,y)-\omega t]\}$$

be incident on the hologram. Just beyond the hologram the wave amplitude is then

$$T_A A'\exp\{j(\phi_r'-\omega t)\} = \text{const}\,A'[A^2+B^2]^{-\gamma/2}\left[\exp\{j(\phi_r'-\omega t)\}\right.$$
$$-\frac{\gamma}{2}\frac{AB}{A^2+B^2}\left(\exp\{j(\phi+\phi_r'-\phi_r-\omega t)\}+\exp\{-j(\phi-\phi_r'-\phi_r+\omega t)\}\right)$$
$$+\frac{\gamma(\gamma+2)}{8}\left(\frac{AB}{A^2+B^2}\right)^2\left(2\exp\{j(\phi_r'-\omega t)\}+\exp\{j(2\phi+\phi_r'-2\phi_r-\omega t)\}\right.$$
$$\left.\left.+\exp\{-j(2\phi-\phi_r'-2\phi_r+\omega t)\}\right)+\cdots\right] \qquad (10)$$

We now make use of the principle of Fresnel–Kirchhoff diffraction theory, according to which the wave field beyond an aperture is fully determined by the amplitude and phase distribution within that aperture, which here corresponds to the hologram area. In view of the linear superposition of wavefields, we can interpret every term in Equation (10) as corresponding to a wave entering image space.

Let us first assume that the reference beam during reconstruction is identical with that during recording,

$$A'\exp\{j\phi_r'\} = A\exp\{j\phi_r\}. \qquad (11)$$

The first term is then simply the reference beam attenuated (since $B^2 \ll A^2$) by a term proportional to $A^{-\gamma}$. If the reference beam is not a plane wave the first term corresponds to the average shading of the hologram, and the second term becomes simply

$$-\frac{\gamma}{2}A^{-\gamma}B\exp\{j(\phi-\omega t)\}, \tag{12}$$

which corresponds simply to the object wave, multiplied by the same shading factor as for the reference beam. We infer from the character of the second term that, looking through the hologram illuminated by the reference beam, we should see the object in its original position, just as though the hologram were a slightly shaded window. The third term

$$-\frac{\gamma}{2}A^{-\gamma}B\exp\{-j(\phi-2\phi_r+\omega t)\} \tag{13}$$

is somewhat more difficult to interpret. It can readily be verified that the function $B\exp\{-j(\phi+\omega t)\}$ corresponds to a wave converging to the mirror image of the object. Furthermore, in the specific case that the reference wave is a plane wave with an angle of incidence α in the x,z plane, ϕ_r becomes simply $(2\pi x/\lambda)\sin\alpha$. Accordingly, for a plane reference wave the third term corresponds to a wave converging toward a mirror image of the object whose center is angularly displaced by $\arcsin(2\sin\alpha)$ in the x,z plane. A more careful examination of the phase term shows that this displacement varies for different parts of the hologram, so that the real image in question is not aberration-free.

The higher-order terms are generally small enough to be neglected. In part they contribute to the images already described, in part they correspond to complex light distributions that bear little relation to an image of the object. For the special case $\gamma=-2$ (positive transparency with an overall γ-factor equal to 2) the higher-order terms are entirely absent.

Consider next the circumstance that the reference beam during reconstruction is a mirror image of the reference beam during recording;

$$A'\exp\{j\phi_r'\}=A\exp\{-j\phi_r\}. \tag{14}$$

Now the first term once again represents the attenuated reference beam, whereas the second term

$$-\frac{\gamma}{2}A^{-\gamma}B\exp\{j(\phi-2\phi_r-\omega t)\} \tag{15}$$

represents (for a parallel reference beam) a wave diverging from an unsharp displaced virtual image. However, the third term now becomes simply

$$-\frac{\gamma}{2} A^{-\gamma} B \exp\{-j(\phi + \omega t)\}, \tag{16}$$

which represents a wave converging to a mirror image of the object.

PHASE HOLOGRAMS

Thus far we have considered absorption holograms, in which light is absorbed in correspondence with exposure during recording. It is, however, also possible to produce phase holograms, in which the phase of the incident light is changed in correspondence to the exposure during recording. Furthermore, phase holograms may be transmission or reflection holograms. A transmission phase hologram may be prepared, e.g., from an absorption hologram by bleaching out the silver grains. What remains is an internal variation of refractive index as well as modulation of the surface contour resulting from differential swelling of the emulsion during development. A reflection hologram results when a thin reflecting film is deposited on top of the developed emulsion. As an alternative, the reflecting film may be formed on an exposed and heat-developed thermoplastic film forming a sandwich with a photoconductor.[15] Phase holograms have also been prepared with photoresists.*

Consider a transmission phase hologram. If we assume that the change in the product of refractive index and thickness, $\Delta(\mu d)$ (and hence the change in phase, $\Delta\phi$, which it produces) is proportional to the logarithm of the exposure,

$$\frac{d(\Delta\phi)}{d(\log(It))} = \gamma, \quad \Delta\phi = \gamma \log \frac{It}{\overline{It}}\,; \quad \Delta\phi = \frac{2\pi}{\lambda}\Delta(\mu d), \tag{17}$$

then the amplitude just beyond the hologram when it is illuminated by a reference beam $A' \exp\{j(\phi_r' - \omega t)\}$ becomes

$$A' \exp\{j(\phi_r' + \Delta\phi - \omega t)\} = A' \exp\{j(\phi_r' - \omega t)\}\left[1 + j\gamma \frac{It - \overline{It}}{\overline{It}} \log_{10} e - (j + \gamma \log_{10} e)\frac{\gamma}{2} \log_{10} e \left(\frac{It - \overline{It}}{\overline{It}}\right)^2 + \cdots\right]$$

---

[15] J. C. Urbach and R. W. Meier, "Thermoplastic Xerographic Holography," *Appl. Optics*, Vol. 5, p. 666, April 1966.

* Private communication by F. Letton and H. J. Gerritsen.

$$= A' \left[\exp\{j(\phi_r' - \omega t)\} + 0.43j\gamma \frac{AB}{A^2+B^2} (\exp\{j(\phi + \phi_r' - \phi_r - \omega t)\} \right.$$
$$\left. + \exp\{-j(\phi - \phi_r' - \phi_r + \omega t)\} + \cdots \right] \tag{18}$$

Comparison with the corresponding Expression (10) for absorption holograms shows that the significant zero and first-order terms are the same in form in the two cases. However, there is no choice of γ for which the higher-order terms disappear altogether.

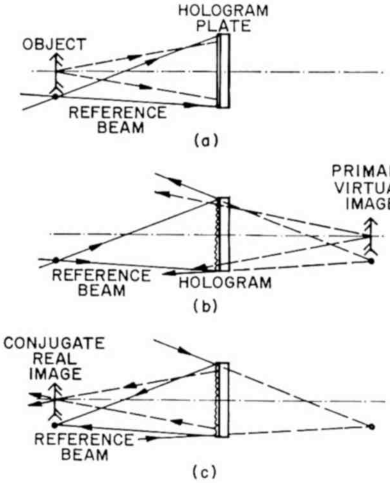

Fig. 6—Mirror hologram: (a) recording, (b) reconstruction of mirror-reversed aberration-free virtual image, and (c) reconstruction of mirror-reversed depth-inverted aberration-free real image.

The advantage of the phase hologram over the absorption hologram is that a greater fraction of the incident reference beam intensity may be utilized for the desired image. For a typical phase hologram this may be of the order of 4%, whereas for a comparable amplitude hologram it is likely to be less than 1%.* This difference corresponds to the well-known difference in the diffraction efficiency of absorption and phase gratings; a sinusoidal absorption grating utilizes at most 1/16 of the incident radiation for one of the first-order diffracted beams, whereas for a sinusoidal phase grating the maximum fraction utilized is slightly greater than 1/3.

For a reflection hologram (Figure 6) prepared by depositing a

---

* According to measurements by D. Greenaway.

thin reflecting film on top of the developed hologram, primary (virtual) and conjugate (real) aberration-free images can be obtained just as for a conventional hologram, with the distinction that these images are mirror-reversed. If a replica is prepared from such a surface hologram by pressing, the images reproduced from the replica exhibit no mirror reversal.

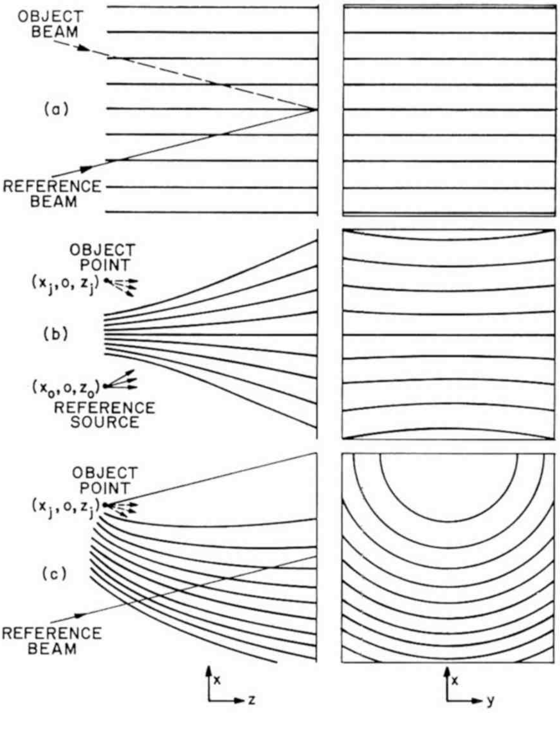

Fig. 7—Standing-wave pattern in front of hologram plate and lines of maximum intensity on hologram plate for point object (approximately every 10^4-th line is indicated): (a) Fraunhofer hologram, (b) Fourier-transform hologram, and (c) Fresnel hologram.

PROPERTIES OF HOLOGRAPHIC RECORDINGS

Many of the properties of the hologram pattern, as well as basic requirements for the recording of holograms, can be inferred from a consideration of the time-integrated intensity variation in the plane of the hologram plate, as expressed by Equation (7). It is instructive to consider the nature of this intensity pattern for a single object point (x_j,y_j,z_j) (Figure 7). For a Fraunhofer hologram, with the reference source at $(x_0,0,z_j)$ and a lens of focal length f_1, we have

$$\phi = -\frac{2\pi}{\lambda}\left(\frac{xx_j}{f_1}+\frac{yy_j}{f_1}\right)+C_j, \quad \phi_r = -\frac{2\pi}{\lambda}\frac{xx_0}{f_1}+C_0, \qquad (19)$$

so that the cosine term in Equation (7) becomes

$$\cos\left\{\frac{2\pi}{\lambda}\left(\frac{x_j-x_0}{f_1}x+\frac{y_j}{f_1}y\right)+C_j'\right\}. \qquad (20)$$

As already pointed out in Equations (1) and (2), this is simply a sinusoidal grating pattern with space period $\lambda f_1/\sqrt{(x_j-x_0)^2+y_j^2}$ and azimuth $\arctan(y_j/(x_j-x_0))$.

For a Fourier-transform hologram, we have instead

$$\begin{aligned}\phi &= \frac{2\pi}{\lambda}\sqrt{(x-x_j)^2+(y-y_j)^2+z_j^2}+C_j\\ &= -\frac{2\pi}{\lambda}\left(\frac{xx_j}{r_j}+\frac{yy_j}{r_j}-\frac{x^2+y^2}{2r_j}+\cdots\right)+C_j'\\ \phi_r &= \frac{2\pi}{\lambda}\sqrt{(x-x_0)^2+y^2+z_0^2}+C_0\\ &= -\frac{2\pi}{\lambda}\left(\frac{xx_0}{r_0}-\frac{x^2+y^2}{2r_0}+\cdots\right)+C_0', \qquad (21)\end{aligned}$$

where r_j and r_0 are the distances of the object point and the reference source, respectively, from the center of the hologram plate. If we omit higher-order terms and put $r_0 = r_j$ (object point and reference source equally distant from hologram), the intensity pattern once more becomes a sinusoidal grating pattern, as for the Fraunhofer hologram. More precisely, the lines of equal intensity are hyperbolas formed by the intersection with the hologram plane of hyperboloids of revolution having the object point and reference point as common foci (see Figure 7(b)).

Consider, finally, a hologram of an object at a finite distance formed with a parallel reference beam with an angle of incidence α in the z,x plane (Fresnel hologram). We now have

$$\phi = \frac{2\pi}{\lambda}\sqrt{(x-x_j)^2+(y-y_j)^2+z_j^2}+C_j$$

$$\phi_r = -\frac{2\pi}{\lambda} x \sin\alpha + C_0. \tag{22}$$

The lines of constant intensity are now the intersections with the hologram plane of paraboloids of revolution whose focus is the object point and whose axis is the line through the object point in the direction of propagation of the reference wave (see Figure 7(c)). These lines are, in general, elliptical. For $\alpha = 0$ (normal incidence of the reference beam) they become circles and the intensity pattern corresponds to that of a zone plate with sinusoidal intensity variation. Thus, the line spacing varies widely over the hologram, being smallest where the rays from the object point form the largest angle with the reference ray at the hologram plane and greatest where the angle is least. Normally, to permit separation of the reference beam from the fainter image beam, the angle between these two rays is made appreciable throughout. Thus, the center of the zone plate pattern does not appear on the hologram plate and the lines of maximum intensity of the pattern, spaced by $\lambda/\sin\theta_j$, cannot be resolved anywhere by the naked eye—this spacing is substantially less than 0.01 mm even for $\theta_j = 5°$!

For an actual object, the hologram becomes a complex of superposed grating or zone-plate patterns that appears visually as a uniformly fogged plate, and even microscopically exhibits a chaotic granular structure. However, the smallest dimensions of this significant "grain" are of the order of

$$D_{\min} = \frac{\lambda}{\{\sqrt{(l_j - l_0)^2 + (m_j - m_0)^2}\}_{\max}}, \tag{23}$$

where (l_j, m_j, n_j) and (l_0, m_0, n_0) are the direction cosines of the object and reference rays, respectively, at any point on the hologram plate. For a round image field subtending a half-angle θ_p at the center of the hologram and a hologram small compared to the image field, we have

$$D_{\min} = \frac{\lambda}{\sin\alpha + \sin\theta_p} \leq \frac{\lambda}{2\sin\theta_p}. \tag{24}$$

For a square image field, with θ_p designating the angle subtended by half a side of the square, we find

$$D_{\min} = \frac{\lambda}{\sqrt{5}\sin\theta_p}. \tag{25}$$

The hologram plate must be capable of resolving $1/D_{\min}$ line pairs per unit length. Thus it could, if used to record a photographic image directly, record

$$N_p = \left(\frac{a}{D_{\min}} \right)^2 . \tag{26}$$

barely resolvable picture elements, where a is the length of the side of the plate. If the same plate were used to form a holographic image, the limiting resolution in the latter would be given by $\lambda z_j/a$, and the length of the side of the image can be put equal to $2z_j \sin \theta_p$, (for large θ_p, $\sin \theta_p$ would have to be replaced by $\tan \theta_p$; however, this would require a parallel increase in the least resolved separation). Thus, the number of barely resolvable picture elements in the hologram image is

$$N_h = \left(\frac{2z_j \sin \theta_p}{\lambda z_j/a} \right)^2 = \left(\frac{2a}{\sqrt{5}\, D_{\min}} \right)^2 = \frac{4N_p}{5} . \tag{27}$$

The reduction in efficiency in storing picture elements in holography by the factor of 4/5 may be ascribed in part to the fact that an off-axis beam is employed to effect separation from the undesired image. The actual loss in storage efficiency is greater owing to a decrease in hologram image intensity as the full resolution capability of the plate is utilized.

Sine-wave response is a more satisfactory measure of the resolution capability of a photographic plate than limiting resolution. For a medium with limited sine-wave response $k(D)$, the sinusoidal terms in the amplitude transmission of the recorded hologram (Figure (9)) must be multiplied by $k(D)$, where, as in Equation (23),

$$D = \frac{\lambda}{\sqrt{\sin^2\theta_j + \sin^2\alpha - 2 \sin \theta_j \sin \alpha \cos \phi_j}} , \tag{28}$$

where θ_j, ϕ_j specify the direction of incidence of a ray from object point (x_j, y_j, z_j) on the hologram. Expressing the object wave as a superposition of the waves from the object points we can thus write the principal term in Equation (9):

$$AB[\exp\{j(\phi - \phi_r)\} + \exp\{-j(\phi - \phi_r)\}] \rightarrow \tag{29}$$

$$\sum_j \frac{A_1 B_j}{r_0 r_j} k[D(x_j, y_j, z_j; x, y; x_0, z_0)] \, [\exp\{jk(r_j - r_0 + c_j\} + \exp\{-jk(r_j - r_0 + c_j)\}],$$

with

$$r_j = \sqrt{(x-x_j)^2 + (y-y_j)^2 + z_j^2}, \quad r_0 = \sqrt{(x-x_0)^2 + y^2 + z_0^2}.$$

A_1 and B_j are amplitude constants and c_j fixed path differences. For Fraunhofer and (to a close approximation) for Fourier-transform holograms, the spacing D is independent of the coordinates (x,y) in the hologram plane. The position of the reference source $(x_0,0,z_0)$ serves as a fixed parameter for D.

Since $k(D)$ enters as a factor in the amplitude of the diffracted wave for any object point, the image intensity of the point is reduced by a factor $k^2(D)$. According to R. C. Jones,[16]

$$k(D) \cong \frac{1}{1+(d_0/D)^2}, \tag{30}$$

where d_0 is a parameter of the emulsion and its development. Since the image intensity drops off very rapidly when D becomes less than d_0, substitution of d_0 for $D_{\min}$ in Equation (24) or (25) should give a valid indication for the angular image field that can be covered with a hologram prepared with a prescribed material. d_0 is, of course, considerably larger than the limiting resolution. Thus, for Kodak Tri-X panchromatic film, d_0 was found to be about 40 microns, as compared to a limiting resolution of 17 microns. For Kodak high-resolution plates, or the comparable red-sensitized Kodak spectroscopic plates, type 649-F, with a sensitivity about 1/10,000 that of Tri-X film, a limiting resolution is cited that is better by a factor of more than 30, so that d_0 may be expected to be of the order of 1 micron. Thus field angles of the order of 40° or more should be acceptable with such plates, in agreement with experiment.

While reduction in sine-wave response (effecting reduction in image brightness) is the primary adverse effect of "grain" in photographic plates, a second drawback is scattered background radiation, which tends to reduce contrast in the image. The latter effect could be expected to be materially less in a structurally more uniform material, such as thermoplastic film, for which Urbach and Meier[15] have reported satisfactory recordings in a range from 200 to 1000 cycles/mm. Both sensitivity and resolution capacity of suitable thermoplastic film photoconductor sandwiches were found to be intermediate between those of Kodak high-resolution plates and conventional photographic materials.

---

[16] R. C. Jones, "Information Capacity of Photographic Film," *Jour. Opt. Soc. Amer.*, Vol. 51, p. 1159, Nov. 1961.

RECORDING CONDITIONS

The nature of the hologram places stringent requirements on the conditions of recording. If there is transverse motion of the hologram plate relative to the object by half a pattern spacing (of the order of 1 micron) during exposure, the hologram pattern may be largely washed out. The sensitivity to longitudinal object displacements is comparable. Since exposure times for 4×5 in^2 holograms with a conventional 10-milliwatt helium–neon c-w laser ($\lambda = 6328$ Å) on Kodak 649-F plates are of the order of 1 minute,* great mechanical stability during recording is essential. If moving objects are to be recorded, the time of exposure should be made short enough that the object displacement during exposure will be of the order of 1 micron or less. For a velocity of 10^2 cm/sec (corresponding to a person walking), the exposure should thus be less than 10^{-6} sec. Q-switched ruby lasers satisfy this condition and supply quite adequate power for the exposure of a hologram. It should be noted, however, that the pulse period should not be too short, since it limits the maximum permissible path difference, Δd, between the interfering rays,

$$\Delta d = \frac{\lambda}{2} \frac{\lambda}{\Delta\lambda} = \frac{\lambda}{2} \frac{cT}{\lambda}. \tag{31}$$

Here c is the velocity of light and $\Delta\lambda$ the "natural line width" corresponding to a pulse duration T. For $T = 10^{-6}$, $\Delta d = 1.5 \times 10^4$ cm or about 500 feet. More generally, Equation (31) indicates the monochromatism of the source required for a prescribed maximum path difference; e.g., if the latter is 1 cm, $\Delta\lambda/\lambda$ should be no greater than about 3×10^{-5}.

The requirements on the reference source (as well as on mechanical stability) during reconstruction are much less stringent. The reference source size must subtend an angle at the hologram that is no greater than the angle subtended by the smallest separation $d_{\min}$ to be resolved in the image. For a television picture with a total field angle of 15°, this is of the order of 2′ of arc. The permissible wavelength spread is

$$\frac{\Delta\lambda}{\lambda} = \frac{d_{\min}}{z_j(\sin\theta_p + \sin\alpha)} \cong \frac{1}{N}, \tag{32}$$

---

* With an argon laser emitting in the range of 4,579 to 5,145 Å. exposure may be less by one or two orders of magnitude.

where N is the number of lines to be resolved along a picture diagonal. Thus, the required monochromatism for an image with the resolution of a television picture ($\Delta\lambda/\lambda \cong 0.002$) could be achieved with a gas discharge source and a suitable line-selecting filter, or from a continuous source with an interference filter. However, a laser solves the problem of obtaining a source with sufficient monochromatism and sufficient brightness (luminous flux per unit area per unit solid angle) in the most satisfactory fashion.

OTHER PROPERTIES OF PLANE HOLOGRAMS

Other properties of the plane hologram that merit consideration are its ability to record and reproduce patterns with enormous dynamic range, to convey the full three-dimensional aspect of an object, and to store numerous images in superposition.

The first property becomes obvious when we consider an object field corresponding to a single light-emitting point source on a dark background. At the hologram plane, the intensity may vary by only a few percent, corresponding to the interference pattern between the reference beam and the light from the object. This may be recorded by a plate with very limited dynamic range. In the image, on the other hand, all of the diffracted light is concentrated in a diffraction disk corresponding to the point source, with the background illuminated by random scattering from the emulsion. Under these circumstances, a dynamic range in the image of 100 db is quite reasonable.

The ability of the hologram to present the full three-dimensional aspect of an object can be realized only by greatly increasing the size, and hence the information storage, in the hologram. Assume that a hologram of diameter d_p (corresponding to the pupil of the eye) permits viewing the object with an angular resolution of 2′ (6×10^{-4} radian). Then

$$1.22\,\frac{\lambda}{d_p} = 6 \times 10^{-4}, \quad d_p = \frac{\lambda}{5 \times 10^{-4}}\ (\cong 1\ \text{mm}). \qquad (33)$$

To view the object at a distance z_j from the hologram throughout a cone of half-angle ω (Figure 8), would require a hologram with an area increased by a factor

$$F = \frac{2\pi(1 - \cos\omega)}{\pi(d_p/2z_j)^2} = 8(1 - \cos\omega)\left(\frac{5 \times 10^{-4}}{\lambda}\,z_j\right)^2. \qquad \mathbf{(34)}$$

For $\omega = 30°$ and a normal viewing distance $z_j = 250$ mm, the factor F is of the order of 5×10^4. If the hologram information were to be transmitted electrically, the bandwidth of the transmission channel would have to be 5×10^4 times as large to transmit the indicated three-dimensional information in place of the two-dimensional information conveyed by the 1-mm diameter hologram.

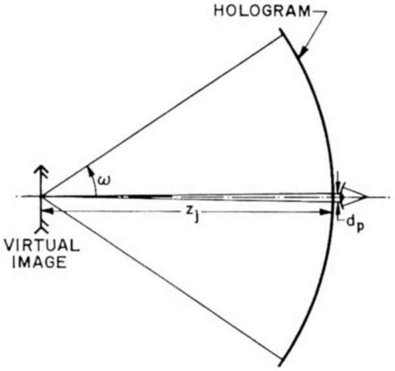

Fig. 8—Hologram for viewing image over wide angular range.

The possibility of storing numerous pictures in superposition can be realized by changing either the wavelength or the direction of the reference beam during recording. However, with plane holograms, the necessity of avoiding overlap between the desired images and spurious images formed by the superposed patterns greatly restricts the angular extent of any one image or the number of images that can be stored. We shall see that conditions are far more favorable for multiple storage in three-dimensional holograms. There is, however, an interesting possibility, predicted by Van Heerden[17] and pointed out very clearly by Gabor,[18] which consists of treating part of the image field as the reference beam. We must then expect exposure of the hologram to the coherent radiation from part of the object to reproduce the entire original object. This has been demonstrated for both transparency and diffuse illumination holograms by Pennington and Collier[19] and

---

[17] P. J. van Heerden, "A New Optical Method of Storing and Retrieving Information," *Appl. Optics*, Vol. 2, p. 387, April 1963.

[18] D. Gabor, "Character Recognition by Holography," *Nature*, Vol. 208, p. 422, 1965.

[19] K. S. Pennington and R. J. Collier, "Hologram-generated Ghost-Image Experiments," *Appl. Phys. Letters*, Vol. 8, p. 14, 1966.

G. W. Stroke and associates.[20] Gabor suggests recording many patterns in superposition and using a portion of each pattern as a key to recover the remainder of the pattern.

THREE-DIMENSIONAL HOLOGRAMS

The distinctive feature of three-dimensional holograms, as compared with plane holograms, is that one and only one image is formed for discrete directions of incidence uniquely related to the wavelength of the incident beam. Thus, if a hologram of an object is formed in precisely the same manner as a plane hologram, with the sole distinction that the thickness of the hologram medium is very large in comparison with the wavelength of light, a perfect three-dimensional *virtual* image is obtained in the position of the original object if the reference beam during reconstruction is identical with the reference beam during recording, and a perfect (depth-inverted) three-dimensional *real* image is formed in the position of the object if the reference beam is simply reversed in direction* (Figure 9). If we deal entirely

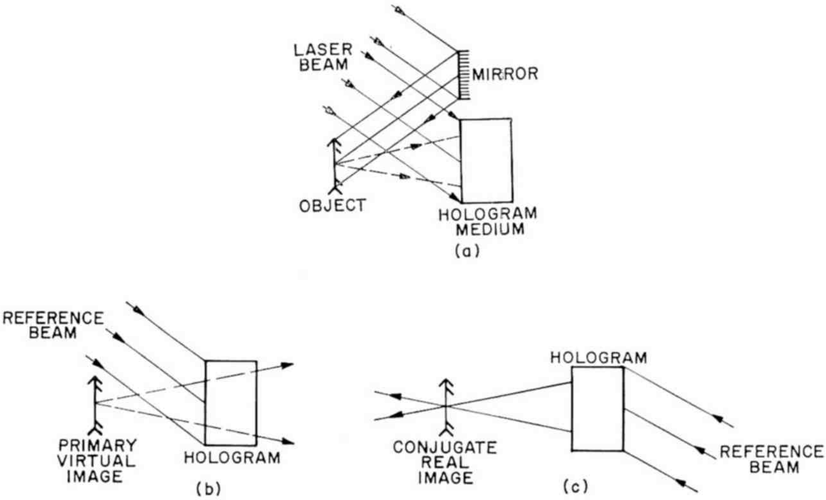

Fig. 9—Three-dimensional hologram: (a) recording, (b) reconstruction of virtual image, and (c) reconstruction of real image.

---

[20] G. W. Stroke, A Funkhouser, and D. Brumm, "Resolution-retrieving Compensation of Source Effects by Correlative Reconstruction in High-resolution Holography," *Phys. Letters*, Vol. 18, p. 274, 1965.

* Interchange of direction of a particular object-wave component and the reference beam will produce a diffracted beam in the direction of the reference beam during recording, but not a complete image.

with plane waves (as is appropriate for Fraunhofer holograms), the interference of the reference beam with the wave originating from any one object point results in a set of equally spaced planes of reinforcement. Designating the direction cosines of the object wave and the reference wave by (l_j,m_j,n_j) and (l_0,m_0,n_0), the direction ratios of the normal to the planes become $(l_j-l_0,\ m_j-m_0,\ n_j-n_0)$ and the spacing

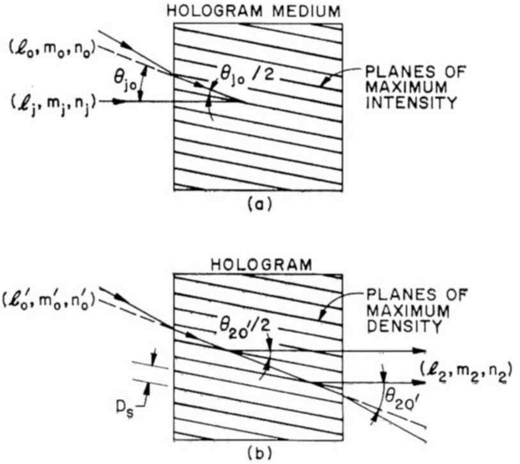

Fig. 10—Standing-wave pattern in three-dimensional hologram for single plane object wave: (a) generation of pattern during recording and (b) reflection of reference beam by pattern in reconstruction.

$$D_s=\frac{\lambda}{\sqrt{(l_j-l_0)^2+(m_j-m_0)^2+(n_j-n_0)^2}}=\frac{\lambda}{2\sin(\theta_{j0}/2)}. \tag{35}$$

If, in reconstruction, a reference wave with direction (l_0',m_0',n_0') and wavelength λ' is incident on the hologram, appreciable intensity will be radiated in the direction (l_2,m_2,n_2) only if both the reflection condition at the planes of reinforcement,

$$\begin{aligned} l_2&=l_0'-2(l_j-l_0)\frac{l_0'(l_j-l_0)+m_0'(m_j-m_0)+n_0'(n_j-n_0)}{(l_j-l_0)^2+(m_j-m_0)^2+(n_j-n_0)^2}\\ m_2&=m_0'-2(m_j-m_0)\frac{l_0'(l_j-l_0)+m_0'(m_j-m_0)+n_0'(n_j-n_0)}{(l_j-l_0)^2+(m_j-m_0)^2+(n_j-n_0)^2}, \end{aligned} \tag{36}$$

and the Bragg condition, that reflections at successive planes be in phase, are fulfilled (Figure 10). For the first order of reflection, the latter can be written, with the value of D_s given by Equation (35),

$$\frac{l_0'(l_j - l_0) + m_0'(m_j - m_0) + n_0'(n_j - n_0)}{(l_i - l_0)^2 + (m_i - m_0)^2 + (n_i - n_0)^2} = \mp \frac{\lambda'}{2\lambda}. \tag{37}$$

Substitution of Equation (37) in Equation (36) leads to

$$\begin{aligned} l_2 &= l_0' \pm (l_j - l_0)(\lambda'/\lambda) \\ m_2 &= m_0' \pm (m_j - m_0)(\lambda'/\lambda) \\ n_2 &= n_0' \pm (n_j - n_0)(\lambda'/\lambda). \end{aligned} \tag{38}$$

We can designate the unit vector in the direction of the object-wave normal as e_j, image-wave normal as e_2, recording reference-wave normal as e_0, and reconstruction reference-wave normal as e_0'. Following Leith et al,[21] we can then write Equation (38) as a single vector equation:

$$e_2 - e_0' \mp (\lambda'/\lambda)(e_j - e_0) = 0. \tag{39}$$

As shown in Figure 11(a), for $\lambda' = \lambda$ and $e_0' = e_0$ (reference beams identical during reconstruction and recording),

$$e_2 = e_j,$$

i.e., there is a virtual image coinciding with the original object; for $e_0' = -e_0$ (reference beam during reconstruction reversed in direction from that during reconstruction),

$$e_2 = -e_j,$$

i.e., the rays from the hologram converge toward a real image coinciding with the original object.

It is also possible (Figure 11(b)) to close the vector quadrangle as required by Equation (39) for $e_0' = e_j$ and $e_2 = e_0$. However, with this choice of the reference beams, Equation (39) is satisfied for only a linear range of directions of e_j. Thus, no complete image is formed corresponding to this condition (assuming, as we do here, that the thickness of the hologram is very large in comparison to the wavelength of the light).

---

[21] E. N. Leith, A. Kozma, J. Upatnieks, J. Marks, and N. Massey, "Holographic Data Storage in Three-dimensional Media," *Appl. Optics*, Vol. 5, p. 1303, Aug. 1966.

If the wavelength during reconstruction differs from that during recording (Figure 11(c)), it is indeed possible to find, for any orientation of e_j and e_0 (object ray and reference ray during recording), specific directions of e_0' and corresponding directions of the image ray e_2 that satisfy Equation (39), provided only that

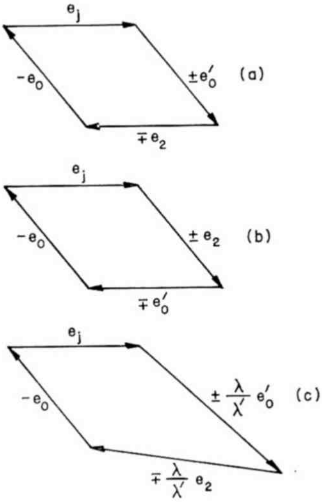

Fig. 11—Relation between unit vectors in direction of propagation of object wave e_j, reference wave during recording e_o, reference wave during reconstruction e_o', and image wave e_2: (*a*) direction of reference wave during recording and reconstruction equal or opposite, (b) reference wave during reconstruction and object wave equal or opposite, (c) different wavelength in recording and reconstruction. Only condition (a) leads to a two-dimensional image for a thick three-dimensional hologram.

$$\frac{\lambda'}{\lambda} < \sqrt{1/2(1 - l_jl_0 - m_jm_0 - n_jn_0)}\,. \tag{40}$$

However, no complete image is formed, since the Equation (39) cannot be fulfilled for a two-dimensional range of directions of e_j when e_0 and e_0' have fixed directions.

If, in the course of the development, the hologram medium shrinks or expands uniformly, images reduced in scale by the shrinkage factor are obtained if the wavelength for reconstruction is reduced by the same factor with respect to the wavelength during recording. However, if the shrinkage is nonuniform, e.g., takes place only in the direction normal to the plane of the emulsion, no true image can, in general, be formed. In this case, the endpoints of the vectors corresponding to e_j and e_0 lie on an ellipsoid of revolution instead of on a sphere, while those corresponding to $-(\lambda/\lambda')e_0'$, $-(\lambda/\lambda')e_2$ must lie on a common sphere if Equation (39) is to be fulfilled. Closure is again achieved only for a linear family of e_j vectors for fixed orientations of the e_0 and e_0' vectors and any fixed wavelength ratio.

All the above conclusions apply only if the hologram is very thick. If this condition is not satisfied, there will be a range of angles of the reference beam during reconstruction for which appreciable intensity is transmitted even though Equation (39) is not satisfied exactly; similarly, for $\lambda'/\lambda \neq 1$, there will be a considerable range of angles of the object ray (about that for which Equation (39) is fulfilled exactly) for which light is emitted in an optimal direction e_2, so that a visible image is formed. To derive an expression for the variation of the intensity with departures from Equation (39), we consider a reference wave of amplitude A_0', wave constant $k' = 2\pi/\lambda'$, and direction of incidence $(l_0'm_0',n_0')$ on the exposed and developed hologram medium. The hologram is pictured as a block of width a, height b, and depth c. We consider, for the sake of convenience, the Fraunhofer case where the object and image are infinitely distant from the hologram (with origin of coordinates at its center), so that a plane wave with direction (l_j,m_j,n_j) corresponds to an object point (x_j,y_j,z_j). In the course of recording and development, exposure to the light from the object and from a plane reference wave with direction (l_0,m_0,n_0) has resulted in a variation in absorption or refractive index given by

$$\text{const}\left(1 + c\sum B_j[\exp\{jk((l_j - l_0)x + (m_j - m_0)y + (n_j - n_0)z + c_j)\}\right.$$
$$\left. + \exp\{-jk((l_j - l_0)x + (m_j - m_0)y + (n_j - n_0)z + c_j)\}] + \cdots\right. \quad (41)$$

Here, c is a constant inversely proportional to the reference beam amplitude. Every element of the hologram scatters an incident wave in proportion to the quantity given by Equation (41). Assuming that the total absorption or scattering of the incident wave by the hologram is small, we find the amplitude at a very great distance $r_2(x_2,y_2,z_2)$ in the direction (l_2,m_2,n_2) by summing the amplitudes contributed by all the elements of the hologram: Confining attention to the first-order terms in Equation (41), we find

$$\frac{\text{const}}{r_2}\sum_{\pm,j} B_j \int_{-a/2}^{a/2} dx \int_{-b/2}^{b/2} dy \int_{-c/2}^{c/2} dz$$

$$\exp\{\pm jk[(l_j - l_0)x + (m_j - m_0)y + (n_j - n_0)z + c_j]\}$$
$$\exp\{jk'[l_0'x + m_0'y + n_0'z]\}$$
$$\exp\{jk'[l_2(x_2 - x) + m_2(y_2 - y) + n_2(z_2 - z)]\}$$

$$= \text{const}\frac{abc}{r_2}\exp\{jk'[l_2x_2 + m_2y_2 + n_2z_2]\}$$

$$\sum_{\pm,j} B_j \exp\{\pm jkc_j\}\frac{\sin\alpha}{\alpha}\frac{\sin\beta}{\beta}\frac{\sin\gamma}{\gamma}, \tag{42}$$

where
$$\alpha = \frac{a}{2}[k'(l_2 - l_0') \mp k(l_j - l_0)],$$

$$\beta = \frac{b}{2}[k'(m_2 - m_0') \mp k(m_j - m_0)],$$

$$\gamma = \frac{c}{2}[k'(n_2 - n_0') \mp k(n_j - n_0)].$$

It should be noted that the direction cosines and the wavelengths λ and λ' pertain to the interior of the hologram medium. If we indicate values outside of the medium by the subscript a and the refractive index of the medium by μ, we find

$$\lambda_a = \mu\lambda, \quad l_{ja} = \mu l_j, \quad m_{ja} = \mu m_j,$$
$$n_{ja} = \sqrt{1 - \mu^2(l_j^2 + m_j^2)} = \sqrt{\mu^2 n_j^2 - \mu^2 + 1.} \tag{43}$$

The total intensity radiated corresponding to a particular object point (x_j,y_j,z_j) is obtained by integrating the square of the absolute value of the corresponding terms in the sum in Equation (42) over l_2 and m_2, since

$$dl_2dm_2 = \cos\theta_2 \sin\theta_2 d\theta_2 d\theta_2. \tag{44}$$

For example, for $(l_0',m_0',n_0') = (l_0,m_0,n_0)$ and $k' = k$ (identical reference beams during recording and reconstruction), we find

$$I_0 = \frac{\text{const}^2 (abc)^2 \lambda^2}{ab \cos \theta_j}, \tag{45}$$

since the limits of the two integrals of the type

$$\int \frac{\sin^2 x}{x^2}\, dx$$

are effectively $-\infty$ and ∞. The last term is practically unity at those points where the other two terms take on appreciable values.

More generally, if a, b, and c are very large compared to λ, the diffracted intensity becomes appreciable only if there is a direction of the image ray (l_2, m_2, n_2) that causes the coefficients of a/λ, b/λ, c/λ in Equation (42) to vanish. This condition leads directly to Equation (39). Furthermore, if the thickness c of the hologram is small compared with its lateral extent, we can quite generally treat the square of the last term in Equation (42) as a constant, substituting for $n_2 = \sqrt{1 - l_2^2 - m_2^2}$ the values for l_2 and m_2 given by the first two equations of Equations (38). We thus find for the relative intensity for different choices of wavelength and direction of the reference beam during reconstruction

$$\frac{I}{I_0} = \left\{ \frac{\sin \dfrac{c}{2} [k'(n_2 - n_0') \mp k(n_j - n_0)]}{\dfrac{c}{2} [k'(n_2 - n_0') \mp k(n_j - n_0)]} \right\}^2, \tag{46}$$

with

$$\begin{aligned} k'(l_2 - l_0') \mp k(l_j - l_0) &= 0 \\ k'(m_2 - m_0') \mp k(m_j - m_0) &= 0. \end{aligned} \tag{47}$$

The vanishing of I/I_0 in Equation (46) indicates, e.g., the minimum angular displacement of the reference beam during recording that will permit the successive recording of two pictures in the hologram so that either can be read out separately without appreciable disturbance from the first. This condition is shown in Figure 12, for a refractive index 1.5 of the hologram medium. The smallest permissible angular displacement (in the x,z plane) is seen to be least for angles between the reference beam and the object beam of the order of 50° and 130°.

by Van Heerden[10] from general considerations. Thus, one limiting factor on the signal-to-noise ratio is the square root of the number of stored pictures; another is the square root of the number of scattering elements (which may be generated by the exposure) in a cell of volume λ_a^3.

The recording media for thick holograms proposed or used up to the present are discolored alkali halide crystals that are partially bleached by the exposure; fine-grained emulsions; and photochromic glasses. Thick photographic emulsions present special problems because of the penetration of the developer throughout the emulsion and because of the very considerable shrinkage as a result of development and fixation. These problems have been discussed by Leith and his associates.[21]

APPLICATIONS

The most striking characteristic of holograms—that of permitting the storage of three-dimensional information in a plane—has been utilized to only a limited extent. One such application is the recording of aerosols with Q-switched lasers and the subsequent measurement of the particle distribution by optical sectioning of the hologram image.[23] A more widely employed application is the preparation of interferograms of objects with arbitrary surface contours.[24,25] In one such procedure, a hologram of an object is exposed, developed, and reinserted in place. When the object is strained, the viewer will see the hologram image superposed on the object with interference contours indicating where the strain has caused the imaging rays to experience a change in path length by odd multiples of $\lambda/2$. The application of holograms for character recognition[26] and coding[27] has also been demonstrated. The correction of the aberrations of optical sys-

---

[23] B. J. Thompson, J. Ward, and W. Zinky, "Application of Hologram Techniques for Particle-Size Determination," *Jour. Opt. Soc. Amer.*, Vol. 55, p. 1566, Nov. 1965.

[24] K. A. Stetson and R. L. Powell, "Interferometric Hologram Evaluation and Real-time Vibration Analysis of Diffuse Objects," *Jour. Opt. Soc. Amer.*, Vol. 55, p. 1694, Dec. 1965.

[25] K. A. Haines and B. P. Hildebrand, "Surface-Deformation Measurement Using the Wavefront Reconstruction Technique," *Appl. Optics*, Vol. 5, p. 595, April 1966.

[26] A. Vander Lugt, "Signal Detection by Complex Spatial Filtering," *IEEE Trans. Inform. Theory*, Vol. IT-10, p. 139, April 1964.

[27] E. N. Leith and J. Upatnieks, "Holographic Imagery Through Diffusing Media," *Jour. Opt. Soc. Amer.*, Vol. 56, p. 523, April 1966.

tems[28] by holography is implicit in Gabor's early work. Its use for x-ray photography remains attractive in spite of great basic difficulties. Finally, the three-dimensional hologram offers the possibility of extraordinarily compact information storage coupled with a relatively simple read-out technique. The comprehensive bibliography on holograms recently published by Chambers and Courtney–Pratt[29] serves as a valuable guide to these and many other aspects of holography.

ACKNOWLEDGMENT

The author has been greatly aided in all aspects of this study by H. J. Gerritsen and his associates who have carried on research on holography at RCA Laboratories.

---

[28] J. Upatnieks, A. Vander Lugt, and E. Leith, "Correction of Lens Aberrations by Means of Holograms," *Appl. Optics*, Vol. 5, p. 589, April 1966.

[29] R. P. Chambers and J. S. Courtney-Pratt, "Bibliography on Holograms," *Jour. S.M.P.T.E.*, Vol. 75, p. 373, April 1966.

ANALYSIS OF PARAMETRIC ACTION IN BACK-BIASED P-N JUNCTIONS CARRYING INJECTED CURRENT*

BY

F. STERZER

RCA Electronic Components and Devices
Princeton, N. J.

Summary—*Photoparametric amplifiers, photoparametric frequency converters, transistor parametric amplifiers, and transistor frequency doublers are analyzed, with both the diffusion and the depletion layer capacitance of the junction of the photodiodes and of the base–collector junction of the transistors taken into account. The analysis shows that the diffusion capacitance, which was neglected in previous analyses, plays an important part in determining the performance of all these devices, and that it can be used to produce new and useful effects such as effective current multiplication in photoparametric and transistor parametric amplifiers.*

INTRODUCTION

THE CAPACITANCE of a back-biased p-n junction carrying injected current is the sum of a diffusion capacitance and of a depletion-layer capacitance.[1,2] Parametric action caused by the depletion-layer capacitance has been analyzed by many authors.[3,4] However, no analysis of parametric action caused by the diffusion capacitance has as yet been published, even though reverse-biased p-n junctions with significant diffusion capacitances are a part of several important parametric devices, e.g., photoparametric amplifiers and transistor parametric amplifiers.

In this paper, parametric action in reverse-biased p-n junctions

---

* The work reported here was supported by the Electronic Technology Division, Air Force Avionics Laboratory, Air Force Systems Command, United States Air Force.

[1] R. Zuleeg, "Effective Collector Capacitance in Transistors," *Proc. IRE*, Vol. 46, pp. 1878-1879, November 1958.

[2] J. R. Collard and F. Sterzer, "Current Dependence of the Depletion-Layer Capacitance of Reverse-Biased P-N Junctions," *Appl. Phys. Letters*, Vol. 5, pp. 165-167, 15 October 1964.

[3] L. A. Blackwell and K. L. Kotzebue, *Semiconductor-Diode Parametric Amplifiers*, Prentice-Hall, Inc., Englewood Cliffs, N. J., 1961.

[4] P. Penfield, Jr. and R. P. Rafuse, *Varactor Applications*, The M.I.T. Press, Cambridge, Mass., 1962.

that carry injected current is analyzed, taking into account both the diffusion and the depletion-layer capacitance of the junctions. General expressions are derived for the currents flowing in a p-n junction that carries injected currents in the presence of an r-f junction voltage. These general expressions are then used to analyze photoparametric amplifiers, photoparametric frequency converters, transistor parametric amplifiers, and transistor doublers. The analysis shows that significant improvements in the performance of all these devices can often be achieved by optimizing the effects of the diffusion capacitance.

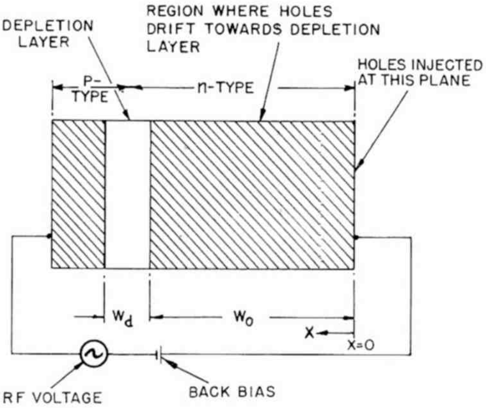

Fig. 1—One-dimensional model of p-n junction used in analysis. This model corresponds to a back-biased p-n photojunction carrying photon-generated minority carriers, or to a transistor base–collector junction carrying injected current from the emitter.

General Analysis

In this section expressions for the currents flowing through an idealized reverse-biased p-n junction that carries injected minority-carrier current in the presence of a junction r-f field are derived. The geometry of the junction to be analyzed is shown in Figure 1. Holes are injected on the n-type side of the junction at a distance W_0 from the n-side edge of the depletion layer. All current flow is assumed to be one-dimensional.

The injected minority-carrier current I_{in} at $x = 0$ in Figure 1 can be written in terms of its Fourier components as follows:*

---

* The form $a = [A\exp\{j\omega t\} + A^*\exp\{-j\omega t\}]/2$ is used throughout this paper for sinusoidally varying quantities, rather than the form $a = A_0 \cos(\omega t + \theta)$. Note that $A = A_0\exp\{j\theta\}$.

$$I_{in} = \sum_{n=0}^{\infty} \frac{(I_{in})_n \exp\{j\omega_n t\} + (I_{in})_n^* \exp\{-j\omega_n t\}}{2}$$
$$= \sum_{n=0}^{\infty} \frac{(i_{in})_n + (i_{in})_n^*}{2}. \qquad (1)$$

For values of x between zero and W_0, the hole density $p_n(x)$ caused by the injected-current component $(i_{in})_n$ is given by[5]

$$p_n(x) = \frac{(i_{in})_n W_0 \sinh\left[\sqrt{j2\omega_n\tau}\left(1 - \frac{x}{W_0}\right)\right]}{A\, qD_p \sqrt{j2\omega_n\tau} \cosh\sqrt{j2\omega_n\tau}}, \qquad (2)$$

where A is the area of the junction, q is the electronic charge, D_p is the hole-diffusion constant, and $\tau = W_0^2/(2D_p)$ is the average transit time through the n-type region of the injected holes, and where it is assumed that W_0 is much smaller than a diffusion length and that the injection level is low. For values of x between W_0 and $W_0 + W_d$, where W_d is the width of the depletion layer, the hole density is nearly zero, because the holes are subjected to the depletion-layer electric field and generally move with the limiting velocity.

The total hole charge Q_{pn} present in the n-type side of the junction as a result of the injected hole current $(i_{in})_n$ is given by

$$Q_{pn} = \int_0^{W_0} qAp_n(x)\, dx = \frac{(i_{in})_n}{j\omega_n}\left[1 - \operatorname{sech}\left(\sqrt{\frac{j\omega_n}{D_p}}\, W_0\right)\right]. \qquad (3)$$

The hole current $(i_{out})_n$ injected into the depletion layer at $x = W_0$ is given by

$$(i_{out})_n = (i_{in})_n - \frac{dQ_{pn}}{dt}$$
$$= (i_{in})_n \left[\operatorname{sech} a_n - \frac{W_0}{D_p a_n}\frac{dW_0}{dt} \tanh a_n \operatorname{sech} a_n\right. \qquad (4)$$

---

[5] R. P. Nanavati, *An Introduction to Semiconductor Electronics*, McGraw-Hill, 1963, Ch. 7.

where

$$a_n = \sqrt{j2\omega_n\tau}. \tag{5}$$

Since there can be no electron current at the edge of the depletion layer, $(i_{out})_n$ is the component of the *total* diffusion current due to $(i_{in})_n$ injected into the depletion layer.

If the junction is abrupt and heavily doped on the n-type side, the differential of W_0 with respect to time is given by[6]

$$\frac{dW_0}{dt} = -\frac{dW_d}{dt} = -\left[\frac{\epsilon}{2NqV}\right]^{1/2}\frac{dV}{dt}, \tag{6}$$

where ϵ is the dielectric constant of the semiconductor, N is the donor density of the n-type material, and V is the voltage across the depletion layer. If the junction is linearly graded, the differential becomes[6]

$$\frac{dW_0}{dt} = -\left(\frac{\epsilon}{18qlV^2}\right)^{1/3}\frac{dV}{dt}, \tag{7}$$

where l is the charge-density gradient in the transition region.

Equations (4) through (7) show that modulation of the voltage across the depletion layer causes a modulation of the diffusion current. The physical reason for this effect is as follows. The transit time of the injected carriers through the n-type region is a function of the depletion-layer width because the carriers move by diffusion (and therefore relatively slowly) outside the depletion layer, but move under the influence of the junction electric field (and therefore, generally, with the limiting velocity) in the depletion layer. Thus, if the depletion layer is widened, the transit time decreases; similarly, if the depletion layer is shortened, the transit time increases. As shown in Equations (6) and (7), the width of the depletion layer is a function of bias voltage. Therefore, modulation of the bias voltage leads to a modulation of the transit time of the injected carriers; as a result, current flows at the sum and difference frequencies of the modulation frequencies of the injected carriers and the r-f bias frequency and its harmonics.

In addition to the minority-carrier current, there is also a displace-

---

[6] See Reference (5), Chapter 3.

ment current i_D flowing across the depletion layer. This current is given by

$$i_D = A\frac{\partial D}{\partial t} = C\frac{dV}{dt}, \tag{8}$$

where D is the electric displacement in the depletion layer, and C has the following values for abrupt and graded junctions:[6]

$$C = A\left(\frac{\epsilon q N}{2V}\right)^{1/2} \text{ for abrupt junction heavily doped on p-type side,} \tag{9}$$

$$C = A\left(\frac{q l \epsilon^2}{12V}\right)^{1/3} \text{ for graded junction.} \tag{10}$$

The total diode current I is the sum of the hole current injected into the depletion layer and the displacement current:

$$\begin{aligned} I &= \sum_{n=0}^{\infty} \frac{I_n \exp\{j\omega_n t\} + I_n^* \exp\{-j\omega_n t\}}{2} \\ &= \sum_{n=0}^{\infty} \frac{(i_{out})_n + (i_{out})_n^*}{2} + C\frac{dV}{dt}. \end{aligned} \tag{11}$$

D-C INJECTED CURRENT

If the injected minority-carrier current is a direct current, the diffusion current flowing in the diode can be determined from Equations (4) and (5) as follows:

$$(i_{out})_0 = (i_{in})_0\left[1 - \frac{W_0}{D_p}\frac{dW_0}{dt}\right] = (i_{in})_0 + C_I\frac{dV}{dt}, \tag{12}$$

where C_I, the intrinsic diffusion capacitance at constant injected current, has the following values for abrupt and graded junctions:*

$$C_I = \left(\frac{\epsilon\tau}{NqD_pV}\right)^{1/2}(i_{in})_0 \text{ for abrupt junction heavily doped on p-type side,} \tag{13}$$

$$C_I = \frac{W_0}{D_p}\left(\frac{\epsilon}{18qlV^2}\right)^{1/3}(i_{in})_0 \text{ for graded junction.} \tag{14}$$

---

* For an experimental verification of Equation (13), see Reference (2).

For an abrupt junction, the current density J_0 for which $C_I = C$ is, from Equations (9) and (13), given by

$$J_0 = qN \left(\frac{D_p}{2\tau} \right)^{1/2}. \tag{15}$$

Current densities of this order of magnitude are often encountered in practice. For example, a 2N1309 p-n-p germanium transistor has a base doping of about $7 \times 10^{14}/\text{cm}^3$, an average base transit time of about 10^{-8} sec, and a junction area of about 2×10^{-3} cm^2. The diffusion constant for holes in germanium at room temperature is approximately 44 cm^2/sec; therefore $J_0 \sim 5.25$ amperes/cm^2, and the corresponding current is approximately 10.5 milliamperes. The maximum rating for the collector current of this transistor is 300 milliamperes.

A-C INJECTED CURRENT

In this section, Equation (11) is solved for the case where the minority-carrier current injected into the diode has a-c components. Two cases are treated: (1) three-frequency parametric amplifiers and frequency converters, and (2) frequency doublers. Only abrupt, highly unsymmetrical junctions are considered.

Three-frequency Parametric Amplifiers and Frequency Converters

In three-frequency parametric amplifiers and frequency converters, voltages at only the following three frequencies (in addition to the d-c bias voltage) are allowed to exist across the p-n junction: (1) the signal frequency f_1, (2) the idler frequency f_2, and (3) the pump frequency f_3, where $f_3 = f_1 + f_2$. In amplifiers, both the input and the output are at frequency f_1; in frequency converters, the input is at frequency f_2 and the output is taken at frequency f_1.

The total voltage across the junction can be written as

$$\begin{aligned} V = V_B + \frac{1}{2} [&V_1 \exp\{j\omega_1 t\} + V_1^* \exp\{-j\omega_1 t\} \\ &+ V_2 \exp\{j\omega_2 t\} + V_2^* \exp\{-j\omega_2 t\} \\ &+ V_3 \exp\{j\omega_3 t\} + V_3^* \exp\{-j\omega_3 t\}]. \end{aligned} \tag{16}$$

Substitution of this expression into Equations (6) and (9), and using

Equations (4), (5), and (11), yields the following equations for the currents at the signal and idler frequencies:

$$I_1 = j\omega_1 \left[C(V_B) + E_0 (I_{in})_0\right] V_1 - \left[\frac{j\omega_1 V_3 C(V_B)}{4V_B} + \frac{j\omega_2 E_3 (I_{in})_3}{2}\right] V_2^* + \frac{j\omega_3 E_2^* (I_{in})_2^* V_3}{2} + (I_{in})_1 \operatorname{sech} a_1, \tag{17}$$

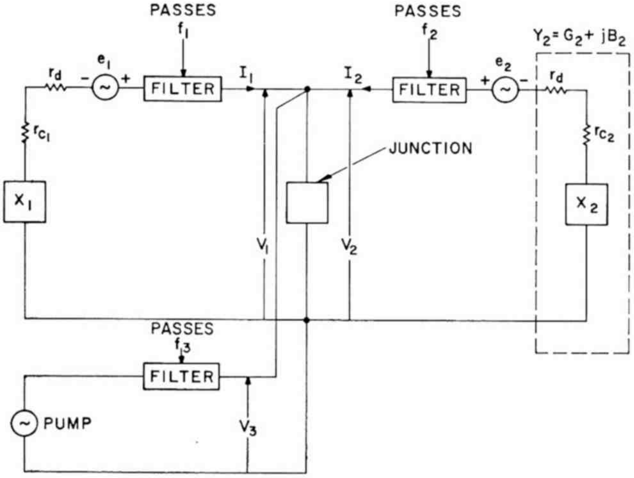

Fig. 2—Circuit arrangement for a three-frequency parametric device (r_d = series resistance of diode).

$$I_2^* = -j\omega_2 \left[C(V_B) + E_0 (I_{in})_0\right] V_2^* + \left[j\omega_2 V_3^* \frac{C(V_B)}{4V_B} + \frac{j\omega_1 E_3^* (I_{in})_3}{2}\right] V_1 - \frac{j\omega_3 E_1 (I_{in})_1 V_3^*}{2} + (I_{in})_2^* \operatorname{sech} a_2^*, \tag{18}$$

where

$$E_n = \frac{W_0}{D_p a_n} \left[\frac{\epsilon}{2NqV_B}\right]^{1/2} \tanh a_n \operatorname{sech} a_n. \tag{19}$$

In deriving Equations (17) and (18), it was assumed that I_{in} has a-c components only at frequencies f_1, f_2, and f_3, and that the d-c component of the junction voltage, V_B, is much larger than the sum of all the a-c components of the junction voltage.

Figure 2 shows the circuit for a three-frequency parametric device.

This circuit indicates the positive directions assumed for the currents and voltages of Equations (17) and (18), and also shows the circuit elements at the three frequencies of interest. Because we derive expressions for signal-to-noise ratios, the noise voltages associated with the series resistance of the junction and with the resistance of the idler load are also indicated.

Figure 2 shows that the value of V_2 is given by

$$V_2 = e_2 - (I_2/Y_2). \qquad (20)$$

If Equation (20) is combined with Equations (17) and (18), the following expression is obtained for the current at the signal frequency:

$$I_1 = Y_{d1}V_1 + \alpha(I_{in})_1 + \beta(I_{in})_2{}^* + \gamma e_2{}^*, \qquad (21)$$

where

$$Y_{d1} = j\omega_1\,[C(V_B) + E_0(I_{in})_0] - \frac{\dfrac{1}{4}\left[\dfrac{\omega_1 V_3}{2V_B}C(V_B) + \omega_2 E_3(I_{in})_3\right]\left[\dfrac{\omega_2 V_3{}^*}{2V_B}C(V_B) + \omega_1 E_3{}^*(I_{in})_3\right]}{G_2 - j\,\{B_2 + \omega_2[C(V_B) + E_0(I_{in})_0]\}} \qquad (22)$$

$$\alpha = \operatorname{sech} a_1 + \frac{\dfrac{1}{4}\left[\dfrac{\omega_1 V_3}{2V_B}C(V_B) + \omega_2 E_3(I_{in})_3\right]\left[\omega_3 E_1 V_3{}^*\right]}{G_2 - j\,\{B_2 + \omega_2[C(V_B) + E_0(I_{in})_0]\}} \qquad (23)$$

$$\beta = \frac{j}{2}\left\{\omega_3 E_2{}^* V_3 + \frac{\left[\dfrac{\omega_1 V_3}{2V_B}C(V_B) + \omega_2 E_3(I_{in})_3\right]\operatorname{sech}^* a_2}{G_2 - j\,\{B_2 + \omega_2[C(V_B) + E_0(I_{in})_0]\}}\right\} \qquad (24$$

$$\gamma = \frac{-\dfrac{j}{2}\left[\omega_1 V_3\dfrac{C(V_B)}{2V_B} + \omega_2 E_3(I_{in})_3\right](G_2 - jB_2)}{G_2 - j\,\{B_2 + \omega_2[C(V_B) + E_0(I_{in})_0]\}}. \qquad (25)$$

Equations (22) through (25) show that Y_{d1}, α, β, and γ are modified if the transit time of the injected carriers is finite (i.e., if $W_0 > 0$). The most dramatic modification occurs in α, which is always equal to or less than unity when W_0 is zero, but which can be larger than unity if W_0 is greater than zero. For values of W_0 greater than zero, therefore, the output current at the signal frequency can be larger than the injected signal-frequency current.

Physically, this multiplication of the injected signal current can be explained as follows. The minority carriers are injected into the junction with a modulation at frequency ω_1. While traversing the n-type region of the junction, the carriers receive an additional modulation of frequency ω_3 (i.e., their transit time is varied at a rate ω_3 by the pump voltage), and an idler current at frequency $\omega_2 = \omega_3 - \omega_1$ is generated. This idler current flows through the idler load and generates a voltage at frequency ω_2; this voltage, in turn, mixes with the pump voltage in the nonlinear capacitance of the junction to generate additional current flow at the signal frequency ω_1.

Equations (22) through (25) can be simplified significantly if the following assumptions are made:

1. The injected direct current $(I_{in})_0$ is so small that

$$(I_{in})_0 \ll \frac{C(V_B)}{E_0}. \tag{26}$$

2. The injected current at the pump frequency is so small that it can be neglected, i.e.,

$$(I_{in})_3 \ll \frac{C(V_B)\,V_3}{2V_B\,E_3}. \tag{27}$$

3. The susceptance B_2 of the idler circuit is selected to tune out the "unpumped" reactance of the p-n junction, i.e.,

$$B_2 = -\omega_2 C(V_B). \tag{28}$$

4. The Q of the idler circuit is so high that

$$|B_2| \gg G_2, \tag{29}$$

where G_2 is the conductance of the idler circuit.

5. The series resistance of the idler circuit r_{c2} is much smaller than the series resistance of the junction r_d, so that

$$R_2 \sim r_d, \tag{30}$$

where R_2 is the total series resistance at the idler frequency.

When these assumptions are used, Equations (22) through (25) become

$$Y_d = j\omega_1 C(V_B) - \frac{1}{16 r_d}\left(\frac{\omega_1}{\omega_2}\right)\frac{|V_3|^2}{V_B^2}, \tag{31}$$

$$\alpha = \operatorname{sech} a_1 + \frac{\pi}{4} E_1 f_c \left(\frac{\omega_1 \omega_3}{\omega_2^2}\right)\frac{|V_3|^2}{V_B}, \tag{32}$$

$$\beta = \frac{jV_3}{2}\left(\omega_3 E_2^* + \frac{\omega_1 \pi f_c}{V_B \omega_2^2}\operatorname{sech} a_2\right), \tag{33}$$

$$\gamma = \frac{1}{4 r_d}\left(\frac{\omega_1}{\omega_2}\right)\left(\frac{V_3}{V_B}\right) - j\omega_1 \frac{C(V_B)}{4}\left(\frac{V_3}{V_B}\right), \tag{34}$$

where f_c is the cutoff frequency of the junction and is given by

$$f_c = \frac{1}{2\pi r_d C(V_B)}. \tag{35}$$

Photoparametric Amplifier

In a photoparametric amplifier, the input is an injected photocurrent at the signal frequency, and the output is taken from a load resistor in the signal circuit.[7-12] In the analysis of such an amplifier,

---

[7] S. K. Saito, K. Kurokawa, Y. Fujii, T. Kimura, and Y. Uno, "Detection and Amplification of the Microwave Signal in Laser Light by a Parametric Diode," *Proc. IRE*, Vol. 50, pp. 2369-2370, November 1962.

[8] D. E. Sawyer, "A Nondegenerate Photoparametric Amplifier," *Proc. IEEE*, Vol. 51, p. 1238, September 1963.

[9] S. Saito and Y. Fujii, "On the Noise Performance of a Photoparametric Amplifier," *Proc. IEEE*, Vol. 52, pp. 978-979, August 1964.

[10] J. R. Collard and F. Sterzer, "Current-Pumped Photo-Parametric Amplifier," 1964 Electron Devices Meeting, Washington, D. C., October 1964.

[11] P. Penfield, Jr. and D. E. Sawyer, "Photoparametric Amplifier," *Proc. IEEE*, Vol. 53, p. 340, April 1965.

[12] J. R. Collard and F. Sterzer, "Photoparametric Detectors with Internal Current Multiplication," 24th Conference on Electron Device Research, Pasadena, Calif., June 1966.

the following currents and voltages must be taken into account:

1. The injected photocurrent, which is given by

$$I_{pc} = i_{pc0} + \frac{1}{2}\left[i_{pc1} + i_{pc1}^{*}\right]$$

$$= i_{pc0} + \frac{1}{2}\left[I_{pc1}\exp\{j\omega_1 t\} + I_{pc1}^{*}\exp\{-j\omega_1 t\}\right]. \quad (36)$$

2. The shot-noise current I_n associated with the average current i_{pc0} flowing through the junction, which is given by

$$I_n = \frac{1}{2}\left[i_{n1} + i_{n1}^{*} + i_{n2} + i_{n2}^{*}\right]$$

$$= \frac{1}{2}\left[I_{n1}\exp\{j\omega_1 t\} + I_{n1}^{*}\exp\{-j\omega_1 t\} + \left[I_{n2}\exp\{j\omega_2 t\} + I_{n2}^{*}\exp\{-j\omega_2 t\}\right]\right]. \quad (37)$$

The shot noise at the pump frequency can usually be neglected because the frequency of the pump is so high in most photoparametric amplifiers that this noise is negligible because of transit-time effects, i.e.,

$$\frac{\tanh\sqrt{j2\omega_3\tau}\,\operatorname{sech}\sqrt{j2\omega_3\tau}}{\sqrt{j2\omega_3\tau}} \ll 1.$$

The mean-square value of I_n can be determined from the following relations:

$$\overline{|I_{n1}|^2} = 2qi_{pc0}\,B_1, \quad (38)$$

$$\overline{|I_{n2}|^2} = 2qi_{pc0}\,B_2, \quad (39)$$

where B_1 and B_2 are the bandwidths at the signal and idler frequencies, respectively.

3. The thermal signal noise voltage E_{ns} associated with the series resistance r_d of the junction, which is given by

$$E_{ns} = \frac{1}{2}\left[e_{n1} + e_{n1}^{*}\right]$$

$$= \frac{1}{2}\left[E_{n1}\exp\{j\omega_1 t\} + E_{n1}^{*}\exp\{-j\omega_1 t\}\right]. \quad (40)$$

The mean-squared value of En_1 is given by

$$|\overline{E_{n1}}|^2 = 4kT_d r_d B_1, \tag{41}$$

where T_d is the temperature of the junction and of the idler circuit, and k is Boltzmann's constant.

4. The thermal idler noise voltage E_{ni} associated with the series resistance r_d of the junction and with the loss resistance r_{c2} of the idler circuit, which is given by

$$\begin{aligned} E_{ni} &= \frac{1}{2}\,[e_{n2} + e_{n2}^{*}], \\ &= \frac{1}{2}\,[E_{n2}\exp\{j\omega_2 t\} + E_{n2}^{*}\exp\{-j\omega_2 t\}]. \end{aligned} \tag{42}$$

The mean-squared value of E_{n2} is given by

$$|\overline{E_{n2}}|^2 = 4kT_d(r_d + r_{c2})B_2. \tag{43}$$

Equivalent circuits incorporating these currents and voltages are shown in Figure 3 for a simple photodetector ($V_3 = 0$), for a photoparametric amplifier with negligible transit time of the injected minority carriers ($W_0 = 0$), and for a photoparametric amplifier with finite transit time ($W_0 > 0$). In all three equivalent circuits, it is assumed that the photodetector or photoparametric amplifier is followed by an amplifier that has an input admittance $Y_A = G_A + jB_A$ and an equivalent noise temperature T_A, and that $(\omega_1 C')^{-1} \gg r_d$, where $C' = C(V_B) + E_0(I_{in})_0$, and $|Y_{d1}^{-1}| \gg r_d$. The thermal noise current at the signal frequency associated with the amplifier is given by

$$\begin{aligned} I_A &= \frac{1}{2}\,[i_{A1} + i_{A1}^{*}] \\ &= \frac{1}{2}\,[I_{A1}\exp\{j\omega_1 t\} + I_{A1}^{*}\exp\{-j\omega_1 t\}], \end{aligned} \tag{44}$$

where

$$|\overline{I_{A1}}|^2 = 4kT_A B\, G_A. \tag{45}$$

The ratio of the power output of a photoparametric amplifier to that of a simple photodetector, as obtained from Figure 3 and Equations (21)-(23), and Equation (36), is given by

$$G = \frac{|\alpha\{Y_a + j\omega_1[C(V_B) + E_0 i_0]\}|^2}{|\operatorname{sech} a_1 (Y_A + Y_{d1})|^2}. \tag{46}$$

G, which is the power gain of the photoparametric amplifier, is much larger than unity if $-Y_{d1}$ approaches Y_A, or if the current multiplication factor α is much larger than unity. Gain resulting from $-Y_{d1}$ approaching Y_A is conventional negative-resistance gain common to all difference-frequency ($\omega_1 = \omega_3 - \omega_2$) parametric devices. This type of gain is sensitive to variations in output load and pump amplitude, and is potentially unstable. On the other hand, gain resulting from $\alpha > 1$ is inherently stable because α is not a function of the load impedance (see Equation (23)). As discussed previously, gain due to $\alpha > 1$ occurs because of the modulation of the transit time of the injected carriers by the pump voltage, and is therefore unique to parametric devices that carry injected minority carriers.

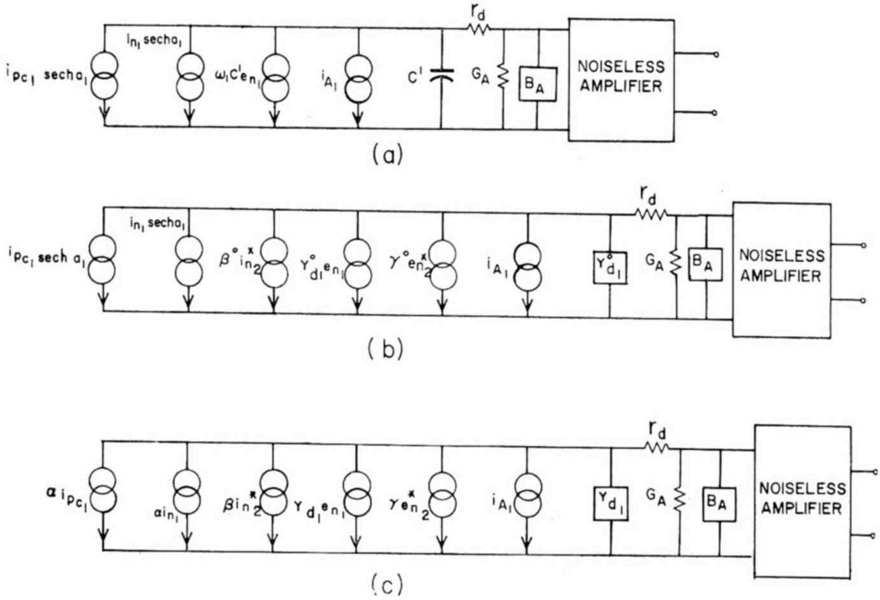

Fig. 3—Equivalent circuits at the signal frequency based on Equations (21) through (25), and (36) through (45), for (a) a p-n junction photodetector, (b) a p-n junction photoparametric amplifier with negligible transit time of the injected minority carriers, and (c) a p-n junction photoparametric amplifier with finite transit time. $C' = C(V_B) + E_0(i_{in})_0$. The superscript 0 in (b) indicates $W_0 = 0$.

Both negative-resistance gain and gain caused by transit-time modulation have been observed experimentally. Achievement of negative-resistance gain in photoparametric amplifiers was reported by Saito and his coworkers,[7] and gain caused by transit-time modulation by Collard and Sterzer.[10] In recent work, Collard reports power gains of 16 db resulting from α in a UHF photoparametric amplifier having negligible negative-resistance gain.[12] His measured values of α are in good agreement with Equation (23).

The signal-to-noise ratio at the output of a photodetector-amplifier or a photoparametric amplifier/amplifier combination, as determined from Figure 3 and Equations (36) through (45), is given by

$$\left(\frac{S}{N}\right)_{\text{detector}} = \frac{1}{2}\,|I_{pc1}\,\text{sech}\,a_1|^2 \Big[2qi_{pc0}B_1\,|\text{sech}\,a_1|^2 + 4kT_d r_d B_1 \omega_1^2 C'^2 + 4kT_A B_1 G_A \Big]^{-1} \tag{47}$$

$$\left(\frac{S}{N}\right)_{\substack{\text{photoparamp}\\ W_0=0}} = \frac{1}{2}\,|I_{pc1}\,\text{sech}\,a_1|^2 \Big[2qi_{pc0}B_1\,|\text{sech}\,a_1|^2 + 2qi_{pc0}B_2|\beta^0|^2 + 4kT_d r_d B_1 |Y_{d1}{}^0|^2 + 4kT_d(r_d + r_{c2})B_2|\gamma^0|^2 + 4kT_A B_1 G_A \Big]^{-1} \tag{48}$$

$$\left(\frac{S}{N}\right)_{\substack{\text{photoparamp}\\ W_0>0}} = \frac{1}{2}\,|I_{pc1}\alpha|^2 \Big[2qi_{pc0}B_1|\alpha|^2 + 2qi_{pc0}B_2|\beta|^2 + 4kT_d r_d B_1|Y_{d1}|^2 + 4kT_d(r_d + r_{c2})B_2|\gamma|^2 + 4kT_A B_1 G_A \Big]^{-1} \tag{49}$$

In Equation (48), the superscript zero indicates $W_0 = 0$.

In many practical situations, the noise contribution from the following amplifier is much larger than the contribution of all the noise sources within the detector or photoparametric amplifier. In such cases, Equations (47) through (49) show that the signal-to-noise ratio of the photoparametric amplifier that has finite transit time is greater by a factor of α^2 than the signal-to-noise ratio of either the detector or the photoparametric amplifier that has negligible transit time. This prediction has been verified experimentally by Collard,[12] who measured an improvement in signal-to-noise ratio by a factor of 40 in a 100-MHz photoparametric amplifier having an α of about 6.3.

Photoparametric Frequency Converter

In a photoparametric frequency converter, the light incident on the junction is modulated at frequency ω_2, and the output from the converter is taken at frequency ω_1. The injected photocurrent can be written as follows:

$$\begin{aligned} I_{pc} &= i_{pc0} + \frac{1}{2} [i_{pc2} + i_{pc2}{}^*] \\ &= i_{pc0} + \frac{1}{2} [I_{pc2} \exp\{j\omega_2 t\} + I_{pc2}{}^* \exp\{-j\omega_2 t\}]. \end{aligned} \tag{50}$$

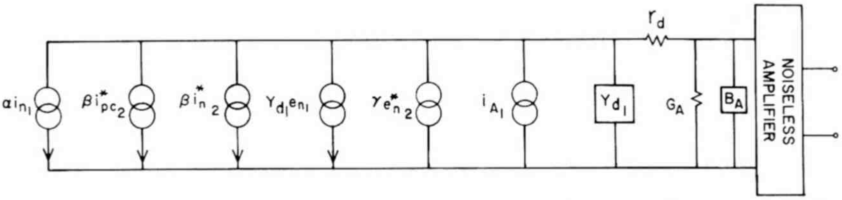

Fig. 4—Equivalent circuit at the output frequency based on Equations (21) and (50) of a p-n junction photoparametric frequency converter.

The equivalent circuit of the converter can be constructed in a straightforward manner from Equations (21) and (50), as shown in Figure 4. This circuit shows that the output signal current is β times the input photocurrent. β is the sum of two parts, as shown by Equation (24) (it is assumed that the term containing $(I_{in})_3$ is negligible); one part is caused by modulation of the transit time of the minority carriers by the pump, and the other by mixing, in the nonlinear junction capacitance, of the pump voltage and of the idler voltage created by the photocurrent flowing through the idler load. Because either or both of these parts can be larger than unity, current gain can also be achieved in photoparametric frequency converters.

The signal-to-noise ratio at the output of an amplifier following a photoparametric frequency converter, as determined from Figure 4 and Equations (37) through (45) and Equation (50), is given by

$$\left(\frac{S}{N}\right)_{\substack{\text{photoparametric}\\ \text{converter}\\ W_0>0}} = \frac{1}{2} |I_{pc2}\beta|^2 \Big[2qi_{pc0}B_1|\alpha|^2 + 2qi_{pc0}B_2|\beta|^2 + 4kT_d r_d B_1 |Y_{d1}|^2 + 4kT_d(r_d + r_{c2})B_2|\gamma|^2 + 4kT_A B_1 G_A \Big]^{-1} \tag{51}$$

Equation (51) shows that the signal-to-noise ratio of the frequency-converter amplifier combination is proportional to $|\beta|^2$, provided (as is often the case) that the noise contribution from the thermal-noise sources is much larger than the contribution from the shot-noise sources.

Parametrically Pumped Transistor Amplifier

The upper frequency limit of a transistor amplifier can be significantly increased by parametrically pumping the amplifier. The circuit for such a parametrically pumped amplifier is similar to the circuit of Figure 2. The pump voltage is applied across the base–collector junction of the transistor, and the minority carriers are injected from a forward-biased emitter into the base–collector junction. Note that a transistor parametric amplifier is a three-terminal device; the input is across the emitter and the base, and the output is across the base and the collector.

If the base width of a conventional junction transistor is much smaller than a diffusion length, then the short-circuit current gain α_0 from elementary transistor theory, or from Equation (23) for $V_3 = 0$, is given by

$$\alpha_0 = \operatorname{sech} a_1 = \operatorname{sech} \sqrt{j2\omega_1\tau}, \tag{52}$$

where ω_1 is the frequency of the injected current and τ is the average transit time of the injected minority carriers across the base. If the current injected into the base is kept constant, then parametric pumping at a frequency ω_3 increases the short-circuit gain by an amount α_p given by

$$\alpha_p = \frac{\pi}{4} f_c \left(\frac{\omega_1\omega_3}{\omega_2{}^2} \right) \frac{|V_3|^2}{V_B} \frac{W_0}{D_p} \left[\frac{\epsilon}{2N_q V_B} \right]^{1/2} \frac{\tanh a_1 \operatorname{sech} a_1}{a_1} \tag{53}$$

where it is assumed that the assumptions given in Equations (26) through (30) are valid so that Equation (32) for α is applicable. The value of α_p depends on frequency through the term $(\tanh a_1 \operatorname{sech} a_1)/a_1$. The absolute value of this term as a function of $\sqrt{\omega_1\tau}$ is given in Figure 5. This curve shows, for example, that α_p is reduced to about one-third of its low-frequency value when $\omega_1\tau = 2$. Thus if the low-frequency value of α_p is three or more, its value is in excess of unity even at frequencies where $\omega_1\tau = 2$.*

---

* If all parameters on the right-hand side of Equation (53) except W_0 are fixed, then α_p is a maximum if W_0 is chosen so that $\omega_1\tau \sim 0.81$.

Frequency Doubling

In frequency doublers, the input to the junction of Figure 1 is primarily at frequency ω, and the output of interest is at frequency 2ω. The most important practical examples of frequency doubling in back-biased p-n junctions that carry injected current are in transistor amplifier–doublers and transistor oscillator–doublers. This mode of operation of transistors is of particular importance in microwave applications because it makes it possible, for example, to generate microwave power with UHF transistors.[13-15]

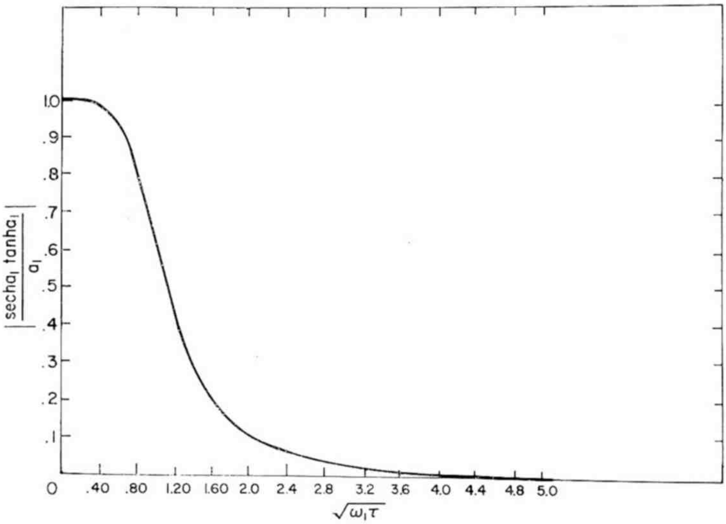

Fig. 5—Curve of $|\operatorname{sech} a_1 \tanh a_1|/|a_1|$ as a function of $\sqrt{\omega_1 \tau}$.

In the present analysis, it is assumed that only fundamental and second-harmonic voltages and currents are allowed to exist (higher harmonics being suppressed by suitable filters). The value of V is then given by

$$V = V_B + \frac{1}{2} [V_1 \exp\{j\omega t\} + V_1^* \exp\{-j\omega t\} + V_2 \exp\{j2\omega t\} + V_2^* \exp\{-j2\omega t\}]. \qquad (54)$$

---

[13] E. Guthrie, et al, "C-Band Solid-State Klystron," NAECON Proc. 340, 1964.

[14] D. E. Nelson, et al, "Transistor Oscillator-Multiplier," 1964 Electron Devices Meeting, Washington, D. C., Oct. 1964.

[15] M. Caulton, H. Sobol, and R. L. Ernst, "Generation of Microwave Power by Parametric Frequency Multiplication in a Single Transistor," *RCA Review*, Vol. 26, p. 286, June 1965.

Substitution of Equation (54) into Equations (6) and (9), and using Equations (4), (5), and (11), yields the following equations for the currents at the fundamental and second-harmonic frequencies.

$$\Bigl[I_1 = j\omega \Bigl\{ [C(V_B) + E_0(I_{in})_0]\, V_1 + \Bigl[\; E_1^*(I_{in})_1^* - \frac{C(V_B)}{4V_B} V_1^*\; V_2 - \frac{E_2(I_{in})_2 V_1^*}{2} \Bigr\} + (I_{in})_1 \operatorname{sech} a_1, \tag{55}$$

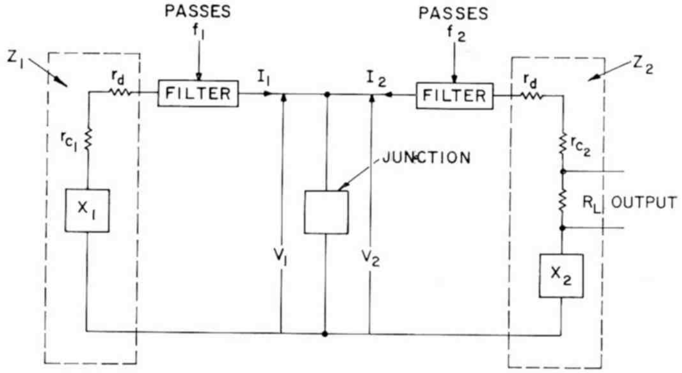

Fig. 6—Circuit arrangement for a frequency doubler (r_d = series resistance of diode).

$$I_2 = j\omega \Bigl\{ \Bigl[\frac{E_1(I_{in})_1}{2} - \frac{1}{4}\,\frac{C(V_B)}{V_B}\, V_1 \Bigr] V_1 + 2\,[C(V_B) + E_0(I_{in})_0]\; V_2 \Bigr\} + (I_{in})_2 \operatorname{sech} a_2, \tag{56}$$

where it was assumed that $V_B \gg V_1 + V_2$, so that higher-order terms could be neglected.

The assumed positive directions of the currents and voltages of Equations (55) and (56) are shown in the equivalent circuit of Figure 6. This circuit shows that the harmonic voltage V_2 can be written

$$V_2 = Z_2 I_2, \tag{57}$$

where Z_2 is the impedance across the junction at frequency 2ω. The power output P_{out} is given by

$$P_{out} = \frac{|I_2|^2}{2} R_L, \tag{58}$$

where R_L is the load resistance.

Elimination of V_2 from Equations (55) and (56) by use of Equation (57) yields the following equations for the currents I_1 and I_2:

$$I_1 = Y_{d1} V_1 + \delta (I_{in})_2 + (I_{in})_1 \operatorname{sech} a_1, \tag{59}$$

$$I_2 = \frac{j\omega \left[\dfrac{E_1 (I_{in})_1}{2} - \dfrac{1}{4} \dfrac{C(V_B)}{V_B} V_1 \right] + (I_{in})_2 \operatorname{sech} a_2}{1 + j2\omega \left[C(V_B) + E_0 (I_{in})_0 \right] Z_2}, \tag{60}$$

where

$$Y_{d1} = j\omega \left[C(V_B) + E_0 (I_{in})_0 \right] + \frac{\omega^2 \left[E_1^* (I_{in})^* - \dfrac{1}{4} \dfrac{C(V_B)}{V_B} V_1^* \right] \left[\dfrac{E_1 (I_{in})_1}{2} - \dfrac{1}{4} \dfrac{C(V_B)}{V_B} V_1 \right] Z_2}{1 + j2\omega \left[C(V_B) + E_0 (I_{in})_0 \right] Z_2}, \tag{61}$$

$$\delta = -j\omega \left[\frac{E_2 V_1^*}{2} + \frac{\left[E_1^* (I_{in})^* - \dfrac{1}{4} \dfrac{C(V_B)}{V_B} V_1^* \right] \operatorname{sech} a_2 Z_2}{1 + j2\omega \left[C(V_B) + E_0 (I_{in})_0 \right] Z_2} \right]. \tag{62}$$

The expressions for Y_{d1} and I_2 can be simplified significantly if the following assumptions are made:

1. The reactance of the junction at frequency ω is tuned out by the reactance of the input circuit, i.e.,

$$I_m (Y_1) = -I_m (Y_{d1}). \tag{63}$$

2. The reactance of the junction at frequency 2ω is tuned out by the reactance of the output circuit, i.e.,

$$I_m (Z_2) = \frac{1}{2\omega \left[C(V_B) + E_0 (I_{in})_0 \right]}. \tag{64}$$

3. There is no injected current at frequency 2ω, i.e.,

$$(I_{in})_2 \sim 0. \tag{65}$$

When these assumptions are used, the expressions for the conductance of the junction and for the output current become

$$\operatorname{Re}(Y_{d1}) = \frac{\left[E_1^*(I_{in})_1 + \frac{1}{4}\frac{C(V_B)}{V_B}|V_1|\right]\left[\frac{E_1}{2}(I_{in})_1 + \frac{1}{4}\frac{C(V_B)}{V_B}|V_1|\right]}{4[C(V_B) + E_0(I_{in})_0]^2 R_2} \tag{66}$$

$$I_2 = \frac{\left[E_1(I_{in})_1 + \frac{1}{2}\frac{C(V_B)}{V_B}|V_1|\right]V_1}{4[C(V_B) + E_0(I_{in})_0]R_2}, \tag{67}$$

where R_2 is the real part of Z_2 and the phase of $(I_{in})_1$ is chosen as the reference phase and set equal to zero.

Equations (66) and (67) show that the transit-time modulation of the injected carriers has a significant effect on the performance of a frequency doubler if either $E_0(I_{in})_0$ or $E_1(I_{in})_1$ is of the same order of magnitude as or larger than $C(V_B)$ or $C(V_B)V_1/(4V_B)$, respectively. The current density J_0 for which $E_0(I_{in})_0 = C(V_B)$ is given by Equation (15); the current density J_I for which $E_1(I_{in})_1 = C(V_B)V_1/(4V_B)$ (assuming $\omega\tau \ll 1$) is given by

$$J_I = \frac{qNV_1}{4V_B}\left(\frac{D_p}{2\tau}\right)^{1/2}. \tag{68}$$

Such current densities are often approached or even exceeded in transistors used in amplifier–multipliers or oscillator–amplifiers.

The modulation of the carrier transit time generally helps to improve the efficiency of a doubler. The power lost in the input circuit is proportional to V_1^2. For a given V_1, however, I_2 increases as E_1 is increased provided the depth of modulation of the injected current is high and $\omega\tau$ is small enough so that E_1 is approximately equal to E_0 in Equation (67); therefore, the power output, which is proportional to I_2^2 as shown in Equation (58), also increases.

CONCLUSION

A small-signal theory has been developed that takes into account the effect of injected minority-carrier current on parametric action in back-biased p-n junctions. This theory differs in important respects from previous parametric theories, which were developed primarily to describe parametric action in varactor diodes and, therefore, did not consider the parametric effects of the diffusion capacitance associated with the injected currents. The new theory has been experimentally verified for d-c injected currents in transistors[2] and for a-c injected currents in photoparametric amplifiers.[12]

ACKNOWLEDGMENT

The author thanks J. R. Collard for many helpful discussions and for permission to quote some of his experimental results.

THRESHOLD PERFORMANCE OF ANALOG FM DEMODULATORS

By

J. Frankle

RCA Communications Systems Division
New York, N. Y.

Summary—*This paper examines the threshold mechanism in three well-known FM detection techniques—limiter–discriminator, phase-locked demodulator (PLD), and the frequency-modulation-feedback demodulator (FMFB). Techniques to suppress these threshold mechanisms are discussed. Threshold performance capabilities of these techniques, as well as models of more advanced demodulators, are analyzed and their performance is compared with that of more conventional demodulators.* It is shown that threshold values 13 db lower than the conventional discriminator and 6 db lower than the PLD or FMFB, at modulation indices around 7 for a typical case, are theoretically achievable.*

INTRODUCTION

THE FM demodulators analyzed here exhibit a characteristic common to all demodulators constructed to compress the transmission bandwidth of signals in the presence of noise. This is the threshold phenomenon, wherein some specified value of carrier to noise power ratio is required to ensure "linear" demodulation. Information theory indicates that, even under theoretically ideal conditions, a boundary exists at which the linear compression (or demodulation) breaks down and begins to lose information in the demodulation process.[1] Practical demodulators exhibit this breakdown because they attempt to measure (or estimate) a signal parameter (amplitude or phase) by performing the measurement on the resultant of signal and noise. This measurement is not linearly related to the signal under all input signal-to-noise ratios and may contain ambiguities that lead to demodulation breakdown. For the type of noise considered here, the probability of breakdown is never zero; however, under high input

---

* The theoretical predictions for several advanced demodulators treated in this article were corroborated experimentally. See contract DA 28-043 AMC-00167(E), U. S. Army Electronics Command, Fort Monmouth, N. J.

[1] D. Slepian, "Bounds on Communication," *Bell System Tech. Jour.*, Vol. 42, p. 681, May 1963.

signal-to-noise ratios, it may be sufficiently small for the effect to be negligible at the demodulator output.

Since the nonlinearity (or threshold) introduced into the demodulated signal is partially determined by the demodulator, it may be reduced by appropriate demodulator design. The characteristics of the signal and the noise, however, will establish the ultimate threshold sensitivity for the demodulation process.

In FM detection the threshold effect appears as sharp impulsive transients at the demodulator output.[2] To evaluate the threshold performance of various demodulators, a quantitative measure of the threshold phenomenon is required; this is based on the common factor (the threshold impulse) and on a characteristic threshold impulse rate. The threshold of an FM demodulator is usually determined by the input–output signal-to-noise ratio curve (see, e.g., Figure 3), where the threshold effect is evidenced by the knee in the curve, above which the demodulator output SNR (signal-to-noise ratio) varies linearly with the input CNR* (carrier-to-noise ratio) and below which the SNR varies as a higher-order power of the input CNR. Although the SNR–CNR plot is a graphic demonstration of the threshold phenomenon, it does not reveal subjective factors that are sometimes more critical than actual SNR at threshold. The demodulator threshold can be viewed as a boundary, the seriousness of which depends upon the system application of the demodulator. It is a region that is characterized by a change in the statistics of the output noise with a rapid deterioration of the output SNR.

The reduction of threshold CNR and the system tradeoffs (e.g., transmitter power, antenna size, equipment complexity, and cost) available from such threshold reduction are vital factors in present-day communication systems. The results of this paper are thus summarized in normalized coordinate plots (such as Figure 11) to facilitate system design.

The basic system under discussion takes the form illustrated in Figure 1. An FM signal is added to white gaussian noise, filtered by an input or i-f filter of noise bandwidth B_{if}, applied to an FM demodulator, and finally filtered by a post-detection filter of noise bandwidth f_b. So that it will be representative of analog signals, the modulation $\dot{\phi}(t)$ is analytically represented as "noise" with a suitable spectral distribution. This approach is particularly appropriate for multi-

---

[2] M. G. Crosby, "Frequency Modulation Noise Characteristics," *Proc. IRE*, Vol. 25, p. 472, April, Pt. 2, 1937.

* CNR is defined as the unmodulated carrier-power-to-noise-power measured at the output of the predetection or i-f filter.

channel FDM signals, where many independent signal sources are multiplexed to produce a "noise-like" result. The noise representation here, however, is used to formulate a model for speech. The speech model is gaussian noise with the spectral distribution shown in Figure 1. The speech spectrum is assumed to start at 1 kHz, roll off at 12 db per octave, and terminate at 4 kHz, to agree closely with measured characteristics of speech[3] over the 1 to 4 kHz region. The exclusion, in the analysis, of speech components below 1 kHz has negligible effect on the analytical results. The choice of gaussian statistics as opposed to exponential statistics, which are more representative of speech waveforms, is made as a matter of convenience and, again, represents a negligible compromise in the analysis. Finally, a speech model waveform peak factor (ratio of peak to rms) of 10 db is assumed.

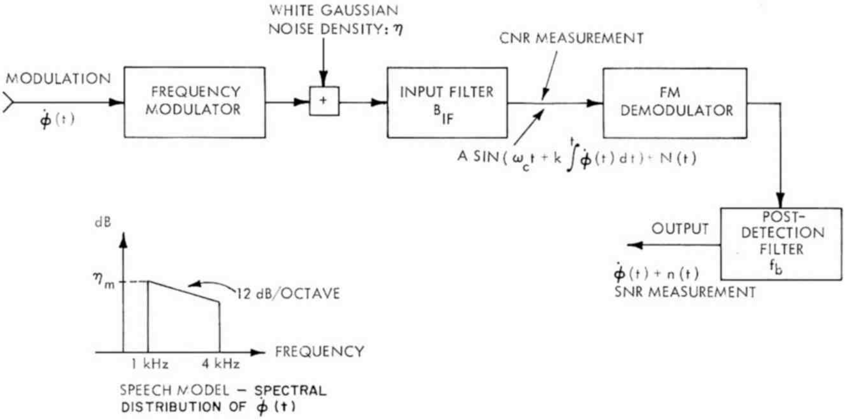

Fig. 1—FM system.

We begin by briefly reviewing some recent work on the limiter–discriminator and applying the results to calculate the threshold characteristics of the limiter–discriminator for a variety of modulation conditions. The results set a foundation for the demodulation techniques subsequently discussed and analyzed.

THRESHOLD IN CONVENTIONAL LIMITER–DISCRIMINATORS

The performance, in the presence of noise, of the conventional FM demodulator (limiter–discriminator) has been treated extensively in

---

[3] H. Fletcher, *Speech and Hearing in Communication*, D. Van Nostrand Co., New York, p. 78, 1953.

the literature.[4–8] Until recently, however, demodulator performance in and below the threshold region has been evaluated in terms of the spectrum and probability density of the instantaneous frequency of an FM signal plus noise. By modeling the limiter–discriminator as an "instantaneous frequency" detector, these analyses provide calculations that describe demodulator performance in the threshold region. Because of analytical complexities, however, only restricted modulation conditions could be handled, these being constant-frequency offset and single sine wave.[8a]

In the laboratory it was recognized that, as the demodulator approached the threshold region, the output noise changes character rapidly from noise that appears gaussian to that resembling a superposition of gaussian noise with impulses. Relying on these observations, S. O. Rice[9,*] postulated a model of the demodulator where the threshold condition is due to impulsive noise components added to the "linearly" demodulated noise component predicted by the above threshold theory. The theoretical results from this model compare well with experimental performance in the threshold region. More importantly, the model allows, without the complexities of the previous analysis, the calculation of limiter–discriminator noise performance in the presence of signals containing random modulations. The model also yields insight into the limiter–discriminator threshold mechanism that aids in formulating threshold-reduction techniques and evaluation of their performance.

Abstracting from Rice's paper, the following points are made.

---

[4] S. O. Rice, "Statistical Properties of a Sine Wave Plus Random Noise," *Bell System Tech. Jour.*, Vol. 27, p. 109, Jan. 1948.

[5] F. L. H. M. Stumpers, "Theory of Frequency Modulation Noise," *Proc. IRE*, Vol. 36, p. 1081, Sept. 1948.

[6] D. Middleton, *The Spectrum of Frequency-Modulated Waves after Reception in Random Noise*, Cruft Lab., Harvard Univ., Pt. I, Tech. Rep. #33, March 1948, Pt. II, Tech. Rep. #62, Nov. 1948.

[7] J. L. Lawson and G. E. Uhlenbeck, *Threshold Signals*, McGraw-Hill Book Co., New York, 1950.

[8] F. W. Fuller and D. Middleton, *Signals and Noise in an FM Receiver*, Cruft Lab., Harvard Univ., Pt. I, Tech. Rep. #242, Feb. 1957, Pt. II, Tech. Rep. #243, Feb. 1957.

[8a] A tutorial discussion of this approach is contained in a paper by M. Schwartz. "Signal-to-Noise Effects and Threshold Effects in FM," *Proc. Natl. Elec. Conf.*, Vol. 18, Sept. 1962.

[9] S. O. Rice, "Noise in FM Receivers," *Time Series Analysis*, Chap. 25, John Wiley, 1963.

[*] It has come to the author's attention that an earlier paper by J. Cohn, "A New Approach to the Analysis of FM Threshold Reception," *Proc. Natl. Elect. Conf.*, Vol. 12, p. 221, 1956, described a similar model of the demodulator.

The limiter–discriminator detects the instantaneous frequency of the resultant formed by adding noise to the carrier signal. The threshold pulses are created by the occasional cancellation of the carrier signal by the input noise accompanied by a 2π radian net change in the resultant phase. These pulses have essentially constant area and an average rate of occurrence, N, in the absence of modulation

$$N = r\,[1 - \operatorname{erf}\sqrt{p}]\ \text{pulses/second,} \tag{1}$$

where r is the radius of gyration of the input filter (having arithmetic symmetry) and p is the input carrier-to-noise-power ratio in the input filter. The effect of modulation is to increase the average pulse rate with the pulses predominantly opposed to the sense of the modulation. This rate is calculated in Appendix A (an extension of Rice's results) and the results are plotted in Figure 2. For the case of rectangular i-f, depicted in Figure 2, the following conclusions can be reached:

(1) The carrier-to-noise separation, for constant pulse rate, in the 10-db region varies by 1 db over the range from no modulation to constant carrier offset.

(2) The majority of the impulses occur at the peaks of the modulation cycle. Note that a sinusoid (which is in the vicinity of its peak a major portion of the time) yields a pulse rate comparable to the equivalent constant carrier-frequency offset.

Rice's analysis concludes by modeling the pulses as impulses of 2π area. This results in a flat spectral-energy distribution, with magnitude $8\pi^2 N$, of pulse noise across the low-frequency region of the demodulator output. Assuming a flat transmission characteristic and a sharp cutoff at f_b, the pulse noise power is equal to $8\pi^2 N f_b$ (rads/s)^2. Thus the demodulator output SNR is*

$$\text{SNR} = \frac{(\Delta\omega)^2/2}{(4\pi^2/3)\ [f_b^2/(2p_n)] + 8\pi^2 f_b N} \tag{2}$$

where $\Delta\omega$ = peak deviation (rads/s) of a sinusoidal modulating tone,

f_b = demodulator post-detection-filter cutoff frequency, and

p_n = normalized input carrier-to-noise power ratio referred to bandwidth $2f_b$.

---

[*] This is a simplification of Rice's results with two second-order effects neglected. Firstly, the signal suppression effect that becomes significant at $p = 0$ db (well below the threshold region), and secondly the nonstationary nature of the output noise in the presence of modulation that results in a lower output noise in comparison to the unmodulated-signal case.

Note that this equation reduces to the well-known FM equation

$$\mathrm{SNR} = 3m^2\,(\mathrm{CNR})_{AM} \tag{3}$$

where $(\mathrm{CNR})_{AM} = p_n$ and $m = \Delta\omega/(2\pi f_b)$ when $N = 0$.

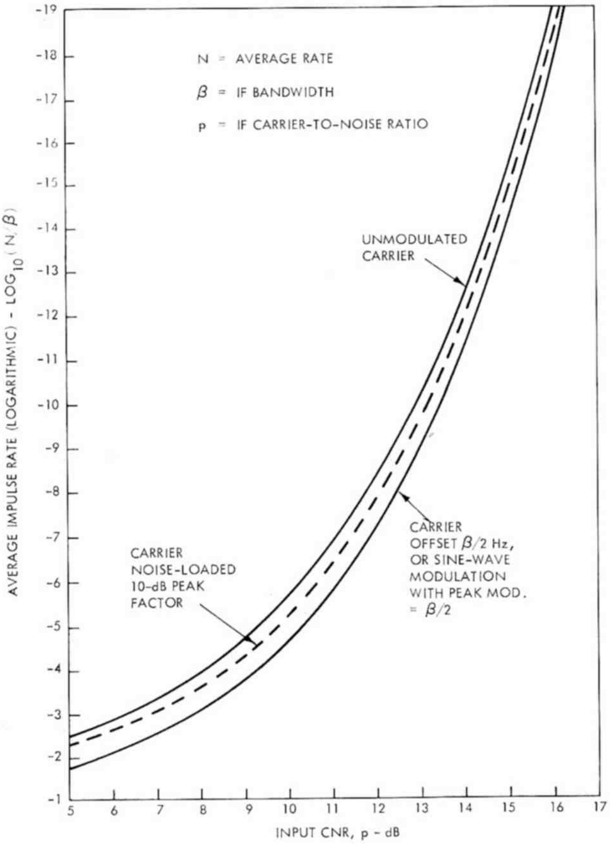

Fig. 2—Average impulse rate at output of discriminator (rectangular i-f).

To evaluate Equation (2), the relationship between the i-f bandwidth and $\Delta\omega, f_b$ must be established (note that N depends upon the i-f bandwidth). This raises the question of modulation distortion, its contribution (both qualitatively and quantitatively) to the output "noise", i-f filter design, and compensation techniques for analog FM signals.

Obviously, an optimum i-f bandwidth and filter shape exists for the signal, depending on the characteristics of the modulation. The problem of signal distortion is complex and intimately related to the signal (such as FDM, single voice channel, or television picture), and further discussion of it is beyond the scope of this paper. The remainder of the discussion is limited to threshold performance based on Carson's Bandwidth Rule, which is widely used and accepted in practice:

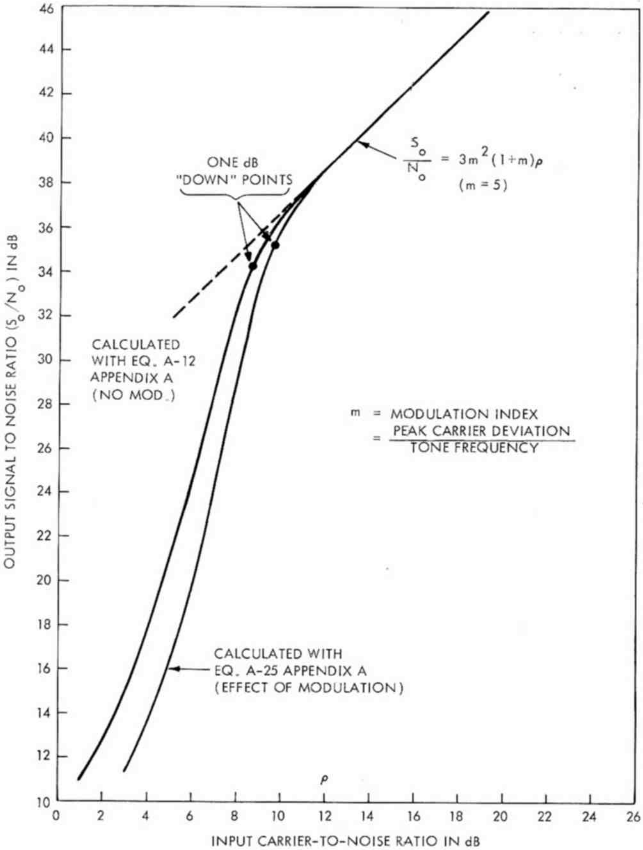

Fig. 3—Output signal-to-noise ratio as a function of input carrier-to-noise ratio (rectangular i-f).

$$B_{if} = 2(f_b + \Delta F_p) \qquad \text{Hz}, \tag{4}$$

where f_b is the top baseband frequency and ΔF_p is the peak deviation of the FM carrier, both in Hz. Although this equation does not satisfy exacting systems requirements, it usually provides a useful and adequate solution. When this bandwidth relationship is incorporated with the parameters of Equation (2), the plot in Figure 3 is obtained for the case of rectangular i-f.

An indication of threshold knee is the departure of the output SNR by roughly 1 to 2 db from the linear relationship between input CNR and output SNR found above threshold. Specifying threshold as the point where the output SNR degrades by 1 db is a reliable definition of threshold that has been applied to the evaluation of other demodulation techniques[10] and that is now used to conclude our evaluation of the conventional FM demodulator.

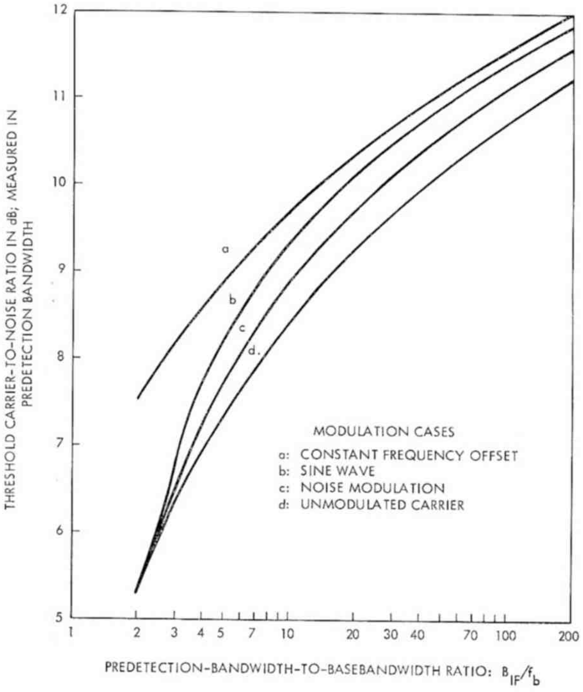

Fig. 4—Threshold CNR as related to pre-detection bandwidth (B_{if}), baseband (f_b) and modulation (conventional limiter–discriminator, rectangular i-f).

Applying to Equation (2) the 1-db degradation factor as the definition of threshold, the following relationship is found to exist between the i-f CNR at threshold and the signal parameters:

$$\left(\frac{B_{if}}{f_b}\right)^2 = \frac{1}{24}\left(\frac{B_{if}}{N}\right)(p)^{-1}.$$

Solution of this equation for the four modulation cases given in Figure 2 results in the threshold CNR curves shown in Figure 4.

---

[10] L. H. Enloe, "Decreasing the Threshold in FM by Frequency Feedback," *Proc. IRE*, Vol. 50, p. 18, Jan. 1962.

When the i-f bandwidth design rule (Equation (4)) for the noise modulation case is applied to the results in Figure 4, the threshold boundary curve for the noise-modulation case in Figure 11 results.

Note that the results of this section are based on an ideal rectangular i-f filter and should be considered optimistic. Other filter shapes, such as single-pole, gaussian, Bessel, and Butterworth, will lead to higher threshold CNR's, as they all tend to attenuate the instantaneous carrier at the peaks of the modulation. This threshold degradation is considered a second-order effect compared to the main threshold determining factor—the noise bandwidth of the predetection filter.

THRESHOLD REDUCTION

The efficiency of threshold reduction techniques can be obtained from Equation (1). It is desired to reduce the number of threshold impulses without excessively distorting the signal or increasing the noise power contributed by each impulse. The obvious technique is to reduce the noise bandwidth of the i-f filter while retaining the signal transmission bandwidth, thus simultaneously reducing r and increasing p (CNR). It is the increase in p that is significant in the reduction of N, as evidenced by the rapid change in the $(1 - \text{erf}\sqrt{p})$ function in the vicinity of $p = 10$ db (see Figure 2). B_{if} can only be reduced by reducing the signal bandwidth, which is synonymous with reducing the signal deviation. The technique of reducing the signal deviation is one of the design objectives in the frequency modulation feedback (FMFB) demodulator, and is discussed at length in the next section.

As the impulse noise that produces the threshold phenomenon has a distinct characteristic with respect to the signal modulation and the linearly demodulated noise, it is theoretically possible to apply impulse noise reduction techniques at the demodulator output. To be effective, these techniques must be applied ahead of the post-detection filter and would consist of circuitry that recognizes the occurrence of a noise pulse and either cancels or blanks the noise pulse prior to the post-detection filter. Several practical problems present themselves; for instance, to recognize the impulse, the high-frequency content of the pulse must be emphasized (either by a high-pass filter or differentiator), and an amplitude detector with a threshold must be employed to sense the occurrence of the impulse. The linearly demodulated noise has a parabolic spectral characteristic essentially extending to $B_{if}/2$, and hence it tends to mask the high-frequency components of the impulse. In addition, the cancellation or blanking of the impulse tends to distort the signal component. The effectiveness of this technique can be estimated by noting, from Figure 2, that 99% of the noise pulses must be identified and precisely cancelled to yield a 3-db improvement in threshold carrier-to-noise ratio.

THE FREQUENCY MODULATION FEEDBACK DEMODULATOR (FMFB)

One method of reducing detector threshold is to track the modulated signal with a replica or estimate of the actual modulation. If the tracking is reasonably precise, the result is an FM signal with reduced deviation. This signal can now be processed by an FM demodulator preceded by a relatively narrow-band predetection filter. The output from the demodulator is a replica of the desired modulation and can be used as the tracking component. The negative feedback system, shown in Figure 5, suggests itself and is called the frequency modulation feedback (FMFB) demodulator.[10–15] This demodulator, investigated by Chaffee[12] and further analyzed and designed for threshold reduction by Enloe,[10,11] exhibits threshold reduction in proportion to the reduction in noise bandwidths between the input i-f filter and the FMFB internal i-f filter.

A limiting factor in this technique of achieving threshold reduction, recognized by Enloe, is that in the presence of input noise, the tracking signal contains a noise component that leads to a second threshold mechanism (as distinct from the threshold mechanism of the limiter–discriminator used as the detector). The onset of this second threshold leads to a lower output SNR than predicted by the above threshold (or small-noise) theory for the demodulation system. From experimental results, Enloe determines that this second, or feedback, threshold is independent of the loop internal detector threshold, and in certain circumstances, may predominate and produce an excessively high demodulation threshold. The onset of the feedback threshold is characterized by the amount of feedback noise, or more specifically, the mean-square-noise phase modulation on the voltage controlled oscillator

---

[11] L. H. Enloe, "The Synthesis of Frequency Feedback Demodulators," *Proc. Nat. Electronics Conf.*, Vol. 18, p. 477, 1962.

[12] J. G. Chaffee, "The Application of Negative Feedback to Frequency-Modulation Systems," *Proc. IRE*, Vol. 27, p. 317, May 1939.

[13] J. R. Carson, "Frequency-Modulation: Theory of the Feedback Receiving Circuit," *Bell System Tech. Jour.*, Vol. 18, p. 395, July 1939.

[14] C. L. Ruthroff and W. F. Bodtman, "Design and Performance of a Broadband FM Demodulator with Frequency Compression," *Proc. IRE*, Vol. 50, p. 2436, Dec. 1962.

[15] J. A. Develet, Jr., "Statistical Design and Performance of High-Sensitivity Frequency-Feedback Receivers," *IEEE Trans. on Milit. Electronics*, Vol. Mil-7, p. 281, Oct. 1963.

(VCO). In a white-noise-input environment (input filter removed) the amount of feedback noise is controlled by the closed-loop response of the demodulator. Hence, it can be minimized by restricting this closed-loop response.

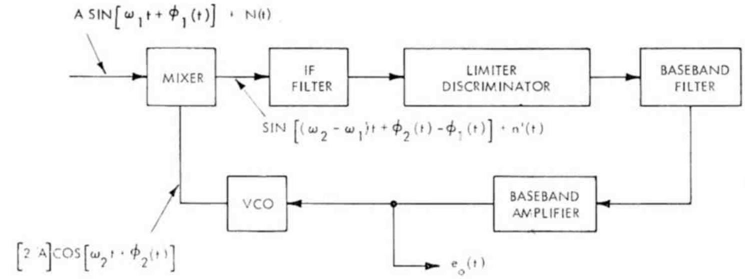

FMFB DEMODULATOR

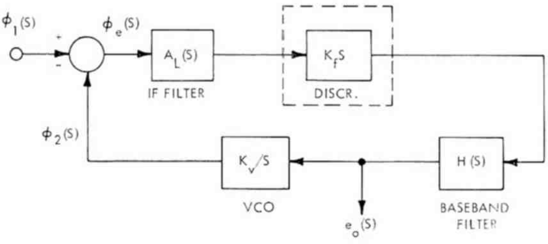

BASIC FMFB DEMODULATOR, LOW-PASS MODEL

Fig. 5—FMFB demodulator.

The Enloe design procedure is as follows. In a white-noise environment, the loop parameters are chosen so that both threshold mechanisms come into play at the same input-carrier level. The feedback threshold mechanism is characterized by the performance curve (shown in Figure 14) obtained when the feedback-threshold carrier-to-noise ratio (referred to twice the baseband) is plotted against a loop-feedback factor (1 + loop gain). If it is assumed that the signal deviation is uniformly compressed by the loop-feedback factor, threshold curves for the internal detector can be plotted against the loop-feedback factor for various input-signal deviations (or input-modulation indices). Because of the diametrically opposite characteristics of the two threshold mechanisms, an intersection of the performance curves exists and specifies the design loop-feedback factor and CNR threshold for the demodulator.

Although an optimization, partially based on empirical measurements, for a white-noise input to the FMFB yields thresholds considerably improved over the conventional limiter–discriminator (preceded by the appropriate input filter), the omission of the input filter in the FMFB analysis results in a less than optimum demodulator performance. A theoretical treatment of the influence of the input filter is not available, but the following qualitative discussion is applicable. After optimization for white-noise input, a comparison is made between the closed-loop noise bandwidth (double-sided) of the demodulator and that of the cascade of the demodulator and the input filter. If the cascade bandwidth is the same as the closed-loop noise bandwidth (double-sided), then the white-noise assumption is justified; however, if the reverse is true, the white-noise optimization is no longer optimum for the entire demodulator (including the input filter), and performance will be better than that shown in Figure 6.

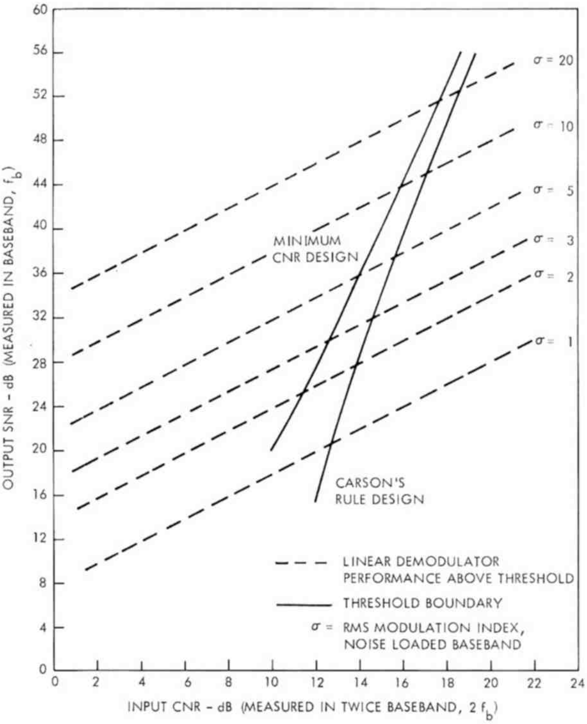

Fig. 6—Threshold performance of various FMFB demodulators.

The full effects of modulation on the FMFB noise performance have yet to be fully analyzed. In the absence of a complete theory, the design is predicated on loop-noise performance with an unmodulated carrier and is carried out by choosing one of two internal i-f bandwidth design rules proposed by Enloe, both of which are modifications of Equation (4):

$$B = 2\left(\frac{\Delta F_p}{1+K}\right),$$

which is referred to here as the Minimum CNR Design, and

$$B = 2\left(\frac{\Delta F_p}{1+K} + f_b\right)\text{ Hz},$$

which is referred to here as the Carson's Rule Design.

$B =$ internal i-f 3-db bandwidth,

$f_b =$ highest baseband frequency transmitted,

$\Delta F_p =$ peak frequency deviation of the signal,

$K =$ design loop gain.

Accordingly, two threshold boundaries are given by Enloe. They are reproduced in modified form in Figure 6.

THE PHASE-LOCKED DEMODULATOR (PLD)

If the voltage-controlled oscillator (VCO) in the FMFB is tuned to the input center frequency, conversion directly to baseband occurs, and the internal i-f filter and limiter–discriminator are removed. The resulting feedback system (Figure 7) is the phase-locked demodulator, and in this sense can be considered a special case of the FMFB circuit. This circuit has been studied by several authors and analyses of its signal and noise characteristics are available in the literature.[16-20]

---

[16] D. Richman, "Color-Carrier Reference Phase Synchronization Accuracy in NTSC Color Television," *Proc. IRE*, Vol. 42, p. 106, Jan. 1954.

[17] R. Jaffee and E. Rechtin, "Design and Performance of Phase-Lock Circuits Capable of Near-Optimum Performance Over a Wide Range of Input Signal and Noise Levels," *Trans. IRE, on Inf. Theory*, Vol. IT-1, p. 66, March 1955.

[18] J. Frankle, F. Lefrak, S. Mehlman, and A. Newton, *Phase-Locked FM Demodulator for 600-Channel FDM*, presented at MIL-E-Con 8, Washington, D. C., 1964.

[19] H. Heinemann, *Threshold Extension Applied to Single-Channel FM Receivers*, presented at MIL-E-CON 8, Washington, D. C., Sept. 1964.

[20] D. L. Schilling and J. Billig, *A Comparison of the Threshold Performance of the Frequency Demodulator Using Feedback and the Phase Locked Loop*, Research Rep. PIBMRI-1207-64, Polytechnic Inst. of Brooklyn, Feb. 28, 1964; also, expanded paper presented at 1965 Int. Space Electronics Symposium, Fontainebleau Hotel, Miami Beach, Fla.

These analyses cover PLD performance for a variety of signal types, but do not cover the area of primary concern—the FM voice-signal model. Appendix B gives a summary of PLD theory and derivations of key equations. The loop operation is summarized as follows:

The PLD detects the incoming FM signal by forming the phase error between the locally generated FM signal (VCO) and the incoming signal. This error signal is fed back to the VCO to reduce the phase error. In the basic PLD, the phase detector is implemented as a doubly balanced mixer exhibiting a sinusoidal output voltage as a function of phase error, thus yielding a multi-valued characteristic. When noise is added to the input signal, it appears in the signal fed back to the VCO, changing the phase error between the VCO and the input signal. When the instantaneous phase error exceeds $\pi/2$ radians, an unstable condition exists in the loop (i.e., positive feedback with respect to the signal). A regenerative action will occur within the loop either progressing the phase of the VCO signal an additional π radians or returning to the original stable region of operation.

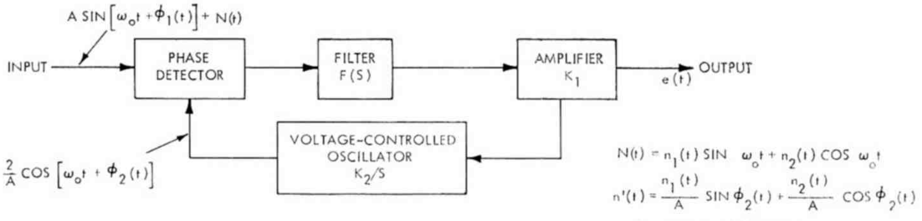

PHASE LOCK DEMODULATOR

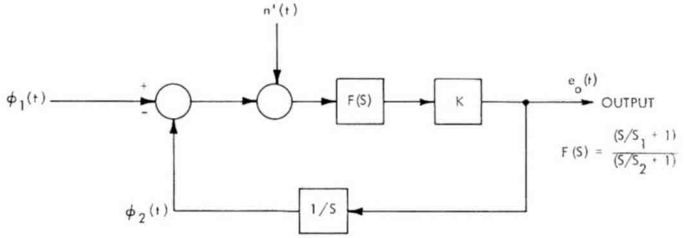

PHASE LOCK DEMODULATOR LINEAR MODEL

Fig. 7—Phase-lock demodulator.

The progression of the VCO phase appears as a rapid phase step of 2π (the center of one stable region to the next) in the VCO output, or as a sharp pulse at the VCO input (the nominal output point of the demodulator). The pulse type noise, when occurring at a sufficiently rapid rate, creates the threshold condition within the loop. Although we say that the VCO phase progresses, it may equally well regress due to both the input noise and modulation; hence VCO phase jumps of plus as well as minus 2π can occur.* In addition, there may be phase jumps of magnitude $2n\pi$ with $n = 2,3,4,5 \cdots$, although they are progressively less probable. The phase jumps are called loss-of-lock transients, and their reduction or elimination is fundamental to reducing the threshold CNR of the PLD. Figure 11 gives the threshold boundary curve for the PLD based on the results obtained in Appendix B. Again, the analysis and optimization is predicated on a white-noise input, and the influence of a predetection filter can only improve performance over that shown in Figure 11.

TECHNIQUES TO REDUCE PLD AND FMFB THRESHOLD

The analysis of the PLD and FMFB demonstrates the optimizations that are possible in a white-noise-input environment. The important factor in the analysis is that the threshold is governed by the noise that is fed around the loop, its variance being controlled by the input CNR referred to the noise bandwidth of the loop. Hence, reduction of the loop noise bandwidth will allow threshold operation with lower input carrier power. Further reduction is possible by incorporating higher-order loop filters, the investigation of which has been partially carried out by others.[21,22] The extent of threshold reduction by this technique is not known explicitly; however, an indication is provided by Develet's comparison of an optimized second-order loop and the optimum loop,[15,23] which shows a 2.25-db difference in performance. It should be noted, however, that the threshold criterion employed by Develet is different from that used here and by Enloe.

Post-detection processing, such as impulse-noise blanking or cancellation, may be applied, but, as discussed previously, a very high

---

* In the presence of modulation the VCO phase jumps (and subsequent threshold impulses) tend to be in opposite sense to the modulation.

[21] E. J. Baghdady—1st Quart. Rept., *Advanced Threshold Reduction Techniques Study*, prepared for NASA Goddard Space Flight Center—N65-30842, Sept. 30, 1964.

[22] S. C. Gupta and R. J. Solem, "Optimum Filters for Second- and Third-Order Phase-Locked Loops by an Error-Function Criterion," *IEEE Trans. on Space Electronics & Telemetry*, Vol. SET-11, p. 54, June 1965.

[23] J. A. Develet, Jr., "A Threshold Criterion for Phase-Lock Demodulation," *Proc. IEEE*, Vol. 51, p. 349, Feb. 1963; also "Correction," *Proc. IEEE*, Vol, 51, p. 580, April 1963.

percentage of the threshold impulses must be eliminated to achieve even a modest threshold reduction.

Techniques to improve threshold performance of the PLD must necessarily reduce the loss-of-lock rate. As the phase error exceeds $\pi/2$ radians due to input noise, the loop becomes regenerative because of the multivalued nature of the sine wave phase-detector characteristic. Thus, for phase errors greater than $\pm\pi/2$ radians, there is a high probability of loss-of-lock. In principle, it is possible to determine phase unambiguously over a 2π range, and thus it is possible to increase the monotonic range of the phase detector. With an increased monotonic range, the noise must exceed a phase error greater than $\pm\pi/2$ radians to produce the regenerative condition. This is equivalent to requiring more input noise to achieve the same loss-of-lock rate (or threshold condition). In essence, the increase in the phase detector monotonic range (with the loop-noise bandwidth fixed) results in a threshold reduction in the PLD. One method for implementing this technique is Tanlock;[24] approximately 4-db threshold reduction is achieved (over the conventional PLD) with the Tanlock parameters adjusted to realize a phase-detector characteristic that is monotonic over ±145°. In another technique[*] phase feedback is incorporated into the PLD to achieve an increased phase detector monotonic range and threshold reduction through a similar range extension.

In Appendix C the threshold for a PLD with idealized phase-detector characteristics is calculated. Two cases are considered—the saw-tooth characteristic and the truncated-sine characteristic (Figure 8). The threshold boundaries for these extended-range PLD's are plotted in Figure 9.

Although both phase-detector characteristics considered have 2π monotonic range, the truncated-sine characteristic results in lower threshold performance than the saw-tooth characteristic when incorporated in the PLD. This may be due to the fact that the truncated-sine characteristic adapts the PLD response to the noise, i.e., as the phase error due to noise increases towards $\pm\pi$ radians (the unlock point), the incremental gain in the loop goes down, thus reducing the loop-noise bandwidth and the fed-back noise, forestalling the unlock condition and threshold impulse.

---

[24] L. M. Robinson, "Tanlock: A Phase Lock Loop of Extended Tracking Capability," *Conf. Proc., 1962 Nat. Winter Convention on Milit. Electronics*, p. 396, 1962.

[*] A. Acampora and A. Newton, "Use of Phase Subtraction to Extend the Range of a Phase-Locked Demodulator," *RCA Review*, Vol. XXVII, No. 3, Dec. 1966 (this issue).

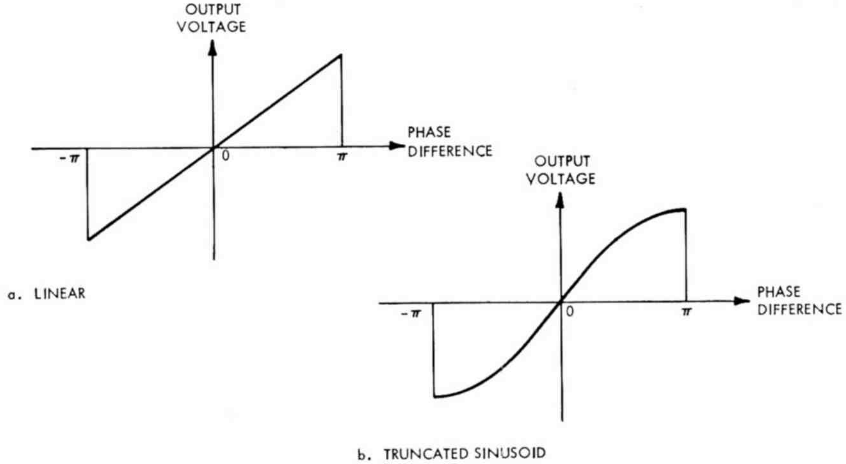

a. LINEAR

b. TRUNCATED SINUSOID

Fig. 8—Idealized phase-detector characteristics.

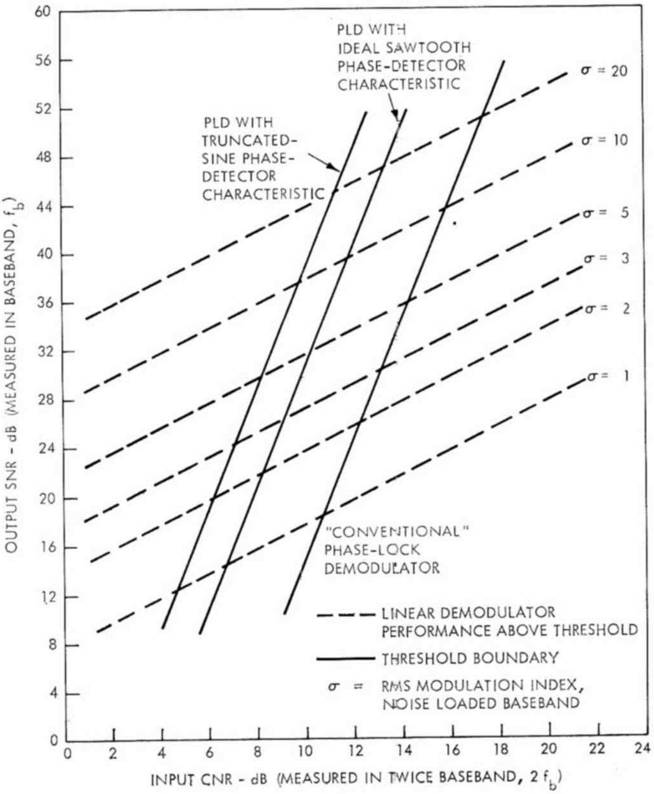

Fig. 9—Threshold performance of various FM phase-lock demodulators.

As described previously, the FMFB demodulator threshold is determined by both the feedback threshold and the open-loop detector threshold. The improvement of either threshold mechanism without deterioration of the other will result in an improved demodulation system. Since the Enloe loop design is predicated on the simultaneous onset of both threshold mechanisms, improvement of one will allow a new choice of loop design parameters (through the Enloe design procedure) that will result in a lower demodulation threshold. The PLD, FMFB, or the extended range PLD can be incorporated[25–27] as the internal detector circuit as a means of improving the open loop threshold. We shall refer to such a system as the compound loop demodulator (Figure 10) and designate it as FMFB-PLD, FMFB-FMFB, or FMFB-ERPLD, where the second term refers to the internal demodulator. A paper describing the design of the FMFB-PLD and FMFB-FMFB compound loops in detail is in preparation. The threshold performance of the compound loops are analyzed in Appendix D, and the threshold boundaries are given in Figure 1.

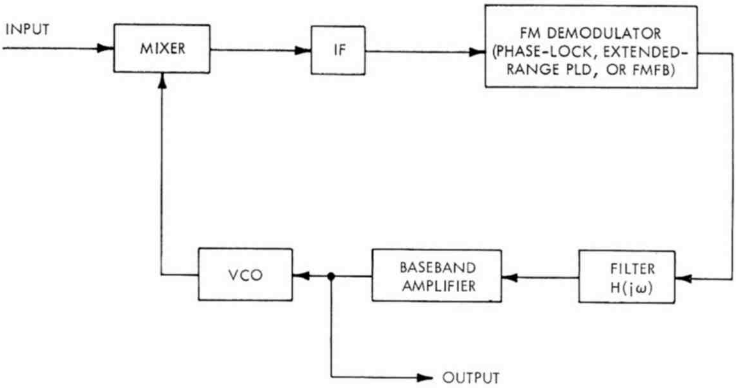

Fig. 10—Compound loop demodulator (functional block diagram).

The analysis is based on the Enloe FMFB analysis and synthesis

---

[25] M. Morita and S. Ito, "High Sensitivity Receiving System for Frequency Modulated Wave," external publication of the Nippon Electric Co. Ltd., Tokyo, Japan; also *IRE Int. Conv. Record*, Vol. 8, Pt. 5, p. 228, 1960.

[26] R. F. Stone, "A Transportable Tracking and Communication Terminal for Passive Satellites," *Proc. 7th MIL-E-CON*, Sept. 9-11, 1963.

[27] R. M. Gagliardi, "Transmitter Power Reduction with Frequency Tracking FM Receivers," *IEEE Trans. on Space Electronics & Telemetry*, Vol. SET-9, p. 18, March 1963.

procedure, with system performance depending on the attainment of all design objectives. In particular the advanced demodulators have a characteristic low-pass base-band frequency response that must be compensated to achieve the desired open-loop gain characteristic stipulated by Enloe. A base-band filter that is the complement of the internal demodulator is required, resulting in a more complex base-band filter than that used in the conventional FMFB.

THE IDEAL DEMODULATOR

To measure the efficiency of the various demodulation techniques discussed, an ideal demodulator is formulated to serve as a reference. This demodulator is one that can compress (or decode) transmitted signals to the base bandwidth with minimum loss of information. The performance boundary for such an ideal demodulator is identified with the lower bound of input signal-to-noise ratio for which information theory predicts errorless transmission. Since the processor can only destroy information, the information capacity at demodulator input and output are, respectively,

$$C_i = B_{if} \ln \left[1 + \frac{S}{\eta_i B_{if}} \right],$$

$$C_0 = f_b \ln \left[1 + \frac{S}{\eta_0 f_b} \right],$$

with the transmission boundary[23] defined by

$$C_0 \leqq C_i ; \ln \left[1 + \frac{S}{\eta_i B_{if}} \right] \geqq \frac{f_b}{B_{if}} \ln \left[1 + \frac{S}{\eta_0 f_b} \right],$$

or, equivalently,

$$\left[1 + \frac{S}{\eta_0 f_b} \right] \leqq \left[1 + \frac{S}{\eta_i B_{if}} \right]^{B_{if}/f_b},$$

where $S =$ signal power in watts,

$\eta =$ noise density in watts per Hz,

$B_{if} =$ transmission bandwidth in Hz,

$f_b =$ base bandwidth in Hz,

$C =$ channel capacity in nats.

The subscripts "o" and "i" denote output and input quantities.

The "errorless" transmission boundary is plotted in Figure 12. Relating the modulation parameter σ to the bandwidth B_{if} by

$$B_{if} = 2f_b\,(1 + \sqrt{10}\sigma)$$

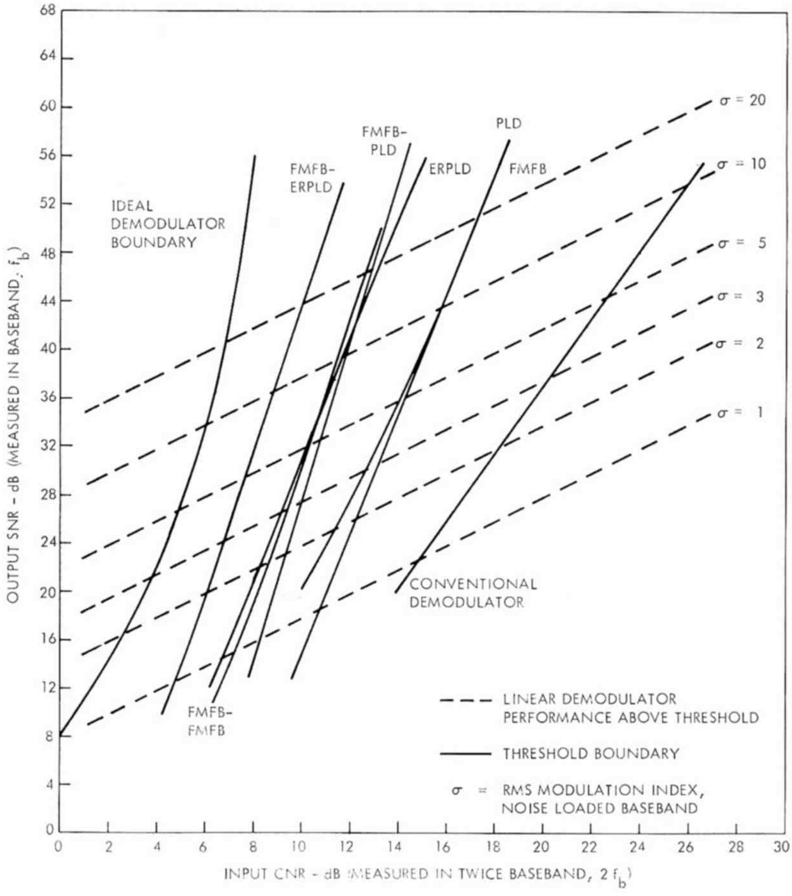

Fig. 11—Threshold performance of various FM demodulators (voice-channel base-band).

results in the ideal performance curve plotted in Figure 11. Figure 11 also summarizes the threshold boundaries of the various demodulation techniques discussed herein.

The transmission mode in the ideal demodulator analysis is quite general; there is no implication that FM could satisfy the "coding and decoding" requirements to achieve the ideal performance boundary. The results indicate, however, that FM coupled to the more esoteric demodulators discussed in this paper proves to be a relatively efficient transmission system in the presence of gaussian noise.

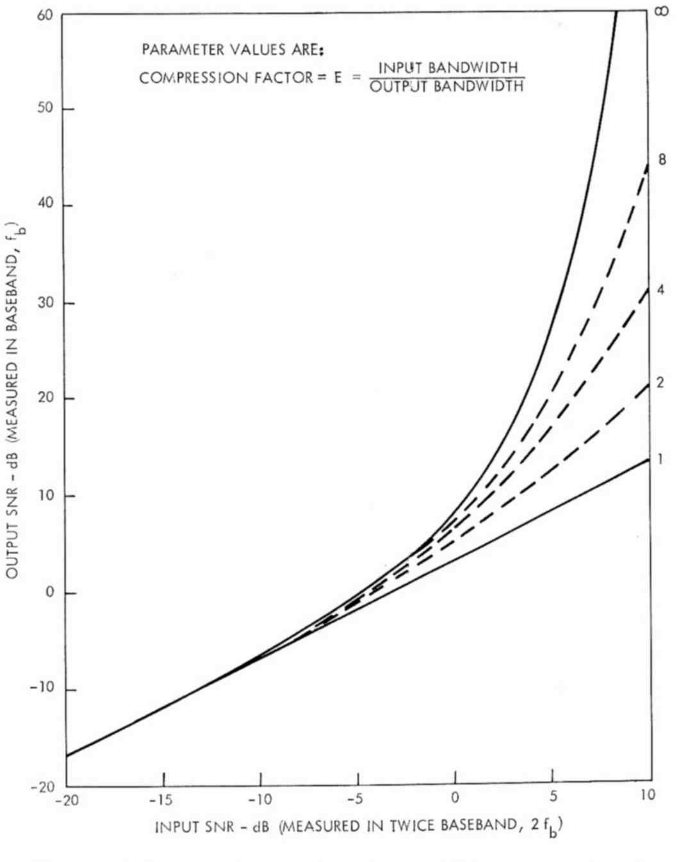

Fig. 12—Threshold bounds for various bandwidth-compression factors for the ideal demodulator.

ACKNOWLEDGMENTS

The author wishes to acknowledge the helpful suggestions of A. Acampora in the derivation of Appendix C, the assistance of F. Lefrak for developing the design curves of Appendix D, and the comments and suggestions of Dr. J. Klapper in the final preparation of this paper.

APPENDIX A—CONVENTIONAL FM DISCRIMINATOR THRESHOLD

This appendix presents the significant parameters that determine the threshold of conventional FM detectors. We apply Rice's results[3] to calculate the FM threshold for several modulation conditions. The average threshold impulse rate (used to determine discriminator threshold) is calculated.

Rice shows that the average threshold impulse rate (in the absence of modulation) is

$$N = r\,(1 - \mathrm{erf}\,\sqrt{p}), \tag{5}$$

where p is the input CNR (measured in B_{if} Hz) and r is the radius of gyration of input-filter characteristic.

Equation (5) is plotted in the text for the case of a rectangular i-f characteristic. In general, the following parameters must be evaluated and applied to Equation (5):

$$r = \frac{1}{2\pi}\,(b_2/b_0)^{1/2}, \tag{6}$$

where

$$b_0 = \int_0^\infty \omega(f)\,df, \tag{7}$$

$$b_2 = (2\pi)^2 \int_0^\infty (f - f_c)^2 \omega(f)\,df, \tag{8}$$

and $\omega(f)$ is the i-f filter power response and f_c is the i-f filter center frequency.

The effect of modulation is to increase the average impulse rate. The following cases are analyzed for comparison to the unmodulated carrier case.

Noise Modulation

Rice derives the average impulse rate, N, for this case as

$$N = 2r\,[e^{-p}] \left[\frac{1 + 2ap}{4\pi p}\right]^{1/2}, \tag{9}$$

where

$$a = \overline{(\dot{\phi})^2}/(2\pi r)^2, \tag{10}$$

and $\overline{(\dot{\phi})^2}$ is the mean square frequency modulation in (rads/sec)^2.

We calculate N by the following. Assuming a rectangular i-f response, with bandwidth B_{if} in Hz:

$$r = B_{if}/\sqrt{12} \tag{11}$$

and

$$a = \frac{(\bar{\dot{\phi}})^2/(2\pi)^2}{B_{if}/12}. \tag{12}$$

The transmitter is assumed to adjust its rms frequency deviation to satisfy the following equation:

$$\frac{\overline{(\dot{\phi})^2}}{4\pi^2} = \frac{1}{10}\left(\frac{B_{if}}{2} - f_b\right)^2 \qquad \text{(Modified Carson's Rule)} \tag{13}$$

where f_b is the top base-band frequency. Therefore,

$$a = 0.3\left[1 - 4\frac{f_b}{B_{if}} + 4\left(\frac{f_b}{B_{if}}\right)^2\right], \tag{14}$$

and Equation (9) reduces to

$$\left(\frac{N}{B_{if}}\right)_m = \frac{e^{-p}}{\sqrt{12\pi p}}\left\{1 + 0.6p\left[1 - 4\frac{f_b}{B_{if}} + 4\left(\frac{f_b}{B_{if}}\right)^2\right]\right\}^{1/2}. \tag{15}$$

In the unmodulated case Equation (5) can be reduced by using the asymptotic expansion for $(1 - \text{erf}\sqrt{p})$:

$$(1 - \text{erf}\sqrt{p}) \approx \frac{e^{-p}}{\sqrt{\pi}\sqrt{p}}, \qquad p \gg 1 \tag{16}$$

$$\left(\frac{N}{B_{if}}\right)_u \approx \frac{e^{-p}}{\sqrt{12}\,\pi\sqrt{p}}, \tag{17}$$

and finally

$$\frac{(N/B_{if})_m}{(N/B_{if})_u} = \left\{1 + 0.6p\left[1 - 4\frac{f_b}{B_{if}} + 4\left(\frac{f_b}{B_{if}}\right)^2\right]\right\}^{1/2}. \tag{18}$$

The impulse rate curve for noise loading can be derived by modifying the curve for the unmodulated case with Equation (18).

Constant Carrier Frequency Offset

In this case the average pulse rate, as derived by Rice, is

$$N = (r^2 + f_0{}^2)^{1/2} \left[1 - \text{erf} \left\{ \left(1 + \frac{f_0{}^2}{r^2} \right)^{1/2} \sqrt{p} \right\} \right] + f_0 e^{-p} \Big\} \text{erf} \left\{ \left(\frac{f_0}{r} \right) \sqrt{p} \right\} \quad (19$$

where f_0 is the frequency offset in Hz.

We calculate N as follows. Assume rectangular i-f, and that the carrier is offset to the edge of the i-f characteristic (i.e., $f_0 = B_{if}/2$). Equation (19) reduces to

$$N = \frac{B_{if}}{\sqrt{3}} [1 - \text{erf} \sqrt{4p}] + \frac{B_{if}}{2} e^{-p} \, \text{erf} \sqrt{3p}. \qquad (20)$$

Over the region of interest ($p = 5$ to 16 db), the first term in Equation (20) is negligible with respect to the second term and the $\text{erf} \sqrt{3p} \sim 1$. Thus,

$$\left(\frac{N}{B_{if}} \right)_m = \frac{1}{2} e^{-p}. \qquad (21)$$

Incorporating Equation (17),

$$\frac{\left(\dfrac{N}{B_{if}} \right)_m}{\left(\dfrac{N}{B_{if}} \right)_u} = \frac{\dfrac{1}{2} e^{-p}}{\dfrac{e^{-p}}{\sqrt{12\pi} \sqrt{p}}} = \sqrt{3\pi} \sqrt{p}. \qquad (22)$$

The impulse rate curve for constant frequency offset is derived by modifying the unmodulated case with Equation (22).

Sine-Wave Modulation

In this case the average pulse rate, as derived by Rice, is

$$N = \frac{\Delta\omega e^{-p}}{\pi^2} + \frac{2re^{-p}}{(4\pi p)^{1/2}} e^{-ap} I_0(ap), \qquad (23)$$

where
$$a=\frac{\left(\dfrac{\Delta\omega}{2\pi}\right)^2}{2r^2}$$

$\Delta\omega =$ peak frequency deviation.

We calculate N for this case as follows. Assume a rectangular i-f and peak frequency deviation $(\Delta\omega/(2\pi))$ Hz related to the i-f half-bandwidth by

$$\frac{B_{if}}{2}=f_b+\frac{\Delta\omega}{2\pi}$$

where f_b is the sine-wave frequency and the post-detection filter bandwidth in Hz. If we make the following substitutions in Equation (23),

$$a=\frac{[(B_{if}/2)-f_b]^2}{\dfrac{2}{3}(B_{if})^2}=1.5\left[1-\frac{2}{1+m}+\frac{1}{(1+m)^2}\right],$$

where m is the system peak modulation index $(m=\Delta\omega/(2\pi f_b))$, it reduces to

$$N=\frac{B_{if}m}{\pi(1+m)}e^{-p}+\frac{2B_{if}e^{-p}e^{-(1.5kp)}}{\sqrt{48\pi}\sqrt{p}}I_0(1.5kp) \tag{24}$$

where

$$k=\left[1-\frac{2}{1+m}+\frac{1}{(1+m)^2}\right].$$

Using the first term of the asymptotic expansion of the modified Bessel function,

$$I_0(1.5kp)=\frac{e^{1.5kp}}{\sqrt{3k\pi p}},\qquad p\gg 1, \tag{25}$$

$$N\sim\frac{B_{if}m}{\pi(1+m)}e^{-p}+\frac{B_{if}e^{-p}}{6\pi p\sqrt{k}}, \tag{26}$$

$$\left(\frac{N}{B_{if}}\right)_s\doteq\frac{e^{-p}}{\pi}\left[1-\frac{1}{1+m}+\frac{1}{6\pi p\sqrt{k}}\right]. \tag{27}$$

Note that if $m \gg 1$, then $k \approx 1$; and if the term $1/(6\pi p)$ is neglected (which, at worst, is a 2% error at $p = 5$ db), Equation (27) can be reduced to

$$\left(\frac{N}{B_{if}}\right)_s \approx \frac{e^{-p}}{\pi} \text{ (large } m \text{ and } p). \tag{28}$$

Equation (28) is similar to Equation (21) and serves to illustrate that the constant carrier offset case is representative of the sine-wave modulation when the peak modulation is equal to the carrier offset (this occurs for $m \gg 1$).

APPENDIX B—PERFORMANCE ANALYSIS OF THE PHASE-LOCKED DEMODULATOR

The phase-locked demodulator (PLD) illustrated in Figure 7 is governed by the following differential equation in operational form[28] (S denoting the differential operator):

$$S\phi_2(t) = KF(S)\ [\sin\{\phi_1(t) - \phi_2(t)\} + n'(t)]. \tag{29}$$

In the absence of noise, and with large loop gain across the modulation components, the phase error $[\phi_1(t) - \phi_2(t)]$ can be made sufficiently small so that the approximation for the sine term is valid, reducing the differential equation to

$$S\phi_2(t) = KF(S)\ [\phi_1(t) - \phi_2(t)]. \tag{30}$$

The loop performance can then be calculated on the basis of the linear model illustrated in Figure 7. If the input noise is gaussian, with flat spectral density of sufficient bandwidth so that it is white with respect to the loop response, it is possible to insert an equivalent noise input to the linear model. This equivalent input is gaussian and white, with a spectral density of $2\eta/A^2$ watts/Hz (where η = input spectral density in region of ω_0 and A is the signal amplitude). With the inclusion of the noise, the linearization remains valid if the phase error, $\phi_e(t) = \phi_1(t) - \phi_2(t)$, remains sufficiently small. Note that $\phi_2(t)$ now contains a noise term determined by the loop response.

The following analysis deals exclusively with the second-order loop

---

[28] A. J. Viterbi, "Phase-Locked Loop Dynamics in the Presence of Noise by Fokker-Planck Techniques," *Proc. IEEE*, Vol. 51, p. 1737, Dec. 1963.

response. Higher-order loop responses are possible,[21,22] but will not be treated at this time.

The second-order loop response can be realized by use of the lag filter for $F(S)$:

$$F(S)=\frac{\left(\frac{S}{S_1}+1\right)}{\left(\frac{S}{S_2}+1\right)}, \tag{31}$$

and the following loop transfer functions are derived on the basis of the linear model:

$$\frac{\Phi_2}{\Phi_1}(S)=\frac{\omega_n{}^2\left(\frac{S}{S_1}+1\right)}{S^2+2\xi\omega_nS+\omega_n{}^2} \tag{32}$$

$$\frac{\Phi_e}{\Phi_1}(S)=\frac{S(S_2)\left(\frac{S}{S_2}+1\right)}{S^2+2\xi\omega_nS+\omega_n{}^2} \tag{33}$$

where $\omega_n{}^2=KS_2$

$$2\xi=\sqrt{S_2/K}+\frac{\sqrt{KS_2}}{S_1}$$

$\Phi(S) =$ the transform of $\phi(t)$.

The phase error is composed of two components—modulation and noise. They are independent if the input noise is white, as previously assumed. Thus, the instantaneous component values as well as their mean square values add linearly;

$$\overline{\phi_e{}^2(t)}=\overline{\phi_n{}^2(t)}+\overline{\phi_s{}^2(t)} \tag{34}$$

$$\overline{\phi_n{}^2(t)}=\frac{2\eta}{A^2}\int_0^\infty\left|\frac{\omega_n{}^2\left(\frac{S}{S_1}+1\right)}{S^2+2\xi\omega_nS+\omega_n{}^2}\right|^2_{S=j\omega}df \tag{35}$$

$$\overline{\phi_s{}^2(t)} = \int_0^\infty \left| \frac{[\Phi_1(S)]\,(S)\,(S_2)\left(\dfrac{S}{S_2}+1\right)}{S^2+2\xi\omega_n S+\omega_n{}^2} \right|^2_{S=j\omega} df \tag{36}$$

where $\overline{\phi_n{}^2(t)}$ = mean square phase error due to noise

$\overline{\phi_s{}^2(t)}$ = mean square phase error due to signal.

In order to realize the lowest threshold value, both components of the phase error (Equation (34)) must be minimized by the loop design. This requires maximizing the loop gain across the modulation frequency range and simultaneously minimizing the closed-loop noise bandwidth. The optimization is formulated by selecting the loop gain K and filter frequency S_2 to establish the loop gain across the base-band frequency range, and then minimizing the closed-loop noise bandwidth by adjusting filter frequency S_1. Equation (35) is evaluated by Gruen[29] and shown to have a minimum for $\xi = 1/2$ under large K and $S_2 \ll S_1$ conditions. Defining B_n as

$$B_n = \int_0^\infty \left| \frac{\omega_n{}^2\left(\dfrac{S}{S_1}+1\right)}{S^2+2\xi\omega_n S+\omega_n{}^2} \right|^2_{S=j\omega} df, \tag{37}$$

we have, from Gruen,

$$B_n = \frac{\omega_n}{2}\ \text{Hz}, \quad \text{and} \quad S_1 = \omega_n, \quad \text{for } \xi = \frac{1}{2}.$$

The effect of modulation on threshold is considered next. If the modulation is gaussian noise, it will merely add a term to the mean square phase error predicted by the linear transfer function Equation (36). The modulation term increases the probability of loss of lock and raises the threshold above the unmodulated case.

Assume a random phase modulation $\phi_1(t)$ that has a spectral distribution $|\Phi_1(j\omega)|^2$ between 0 and ω_b rads/sec in the base-band range. The total mean-square phase error, Equations (34) and (36), yields

---

[29] W. J. Gruen, "Theory of AFC Synchronization," *Proc. IRE*, Vol. 41, p. 1043, Aug. 1953.

$$\overline{\phi_e{}^2(t)} = \frac{2\eta}{A^2}\,\frac{\omega_n}{2} + \int_0^{f_b} |\Phi_1(j\omega)|^2 \left|\frac{\Phi_e}{\Phi_1}(j\omega)\right|^2 df. \tag{38}$$

Note that with $\xi = 1/2$ and $B_n = \omega_n/2$ Hz, the transfer function for $\omega_n > \omega_b$ in the integral above is essentially

$$\left|\frac{\Phi_e}{\Phi_1}(j\omega)\right| \doteq \left|\frac{S^2}{\omega_n{}^2}\right|_{S=j\omega} = \frac{\omega^2}{\omega_n{}^2} \tag{39}$$

over the base-band frequency range. Equation (38) reduces to

$$\overline{\phi_e{}^2(t)} = \frac{\eta\omega_n}{A^2} + \frac{1}{\omega_n{}^4}\int_0^{f_b} \omega^4 |\Phi_1(j\omega)|^2 df. \tag{40}$$

Setting

$$Y = \int_0^{f_b} \omega^4 |\Phi_1(j\omega)|^2 df, \tag{41}$$

the total mean square error $\overline{\phi^2(t)}$ is minimized by setting the derivative

$$\frac{d\overline{\phi_e{}^2(t)}}{d\omega_n} = \frac{\eta}{A^2} - \frac{4Y}{\omega_n{}^5} = 0. \tag{42}$$

This leads to the conclusion that the optimum apportionment of the mean-square phase error is distributed one-fifth of the total to the modulation-induced components and four-fifths to the noise-induced components. From Viterbi's[28] analysis of the first-order loop it is possible to determine the mean-square phase error in the linear model that is indicative of the point where the actual mean-square phase error has increased by 1 db over that predicted by the linear model. From Figure 13 (from Viterbi) it is seen that this occurs when $\overline{\phi_e{}^2(t)} = 1/4$ (rad/sec)^2. Although this is a result obtained for the first-order loop, and is the point where the total noise from the loop (rather than the portion found in f_b Hz) has increased by 1 db, we take it as the threshold condition for the second-order loop (this criterion is also found in

Heitzman[30]). The result is that the threshold occurs when

$$\frac{2\eta}{A^2}B_n = \left(\frac{4}{5}\right)\left(\frac{1}{4}\right) = \frac{1}{5}, \tag{43}$$

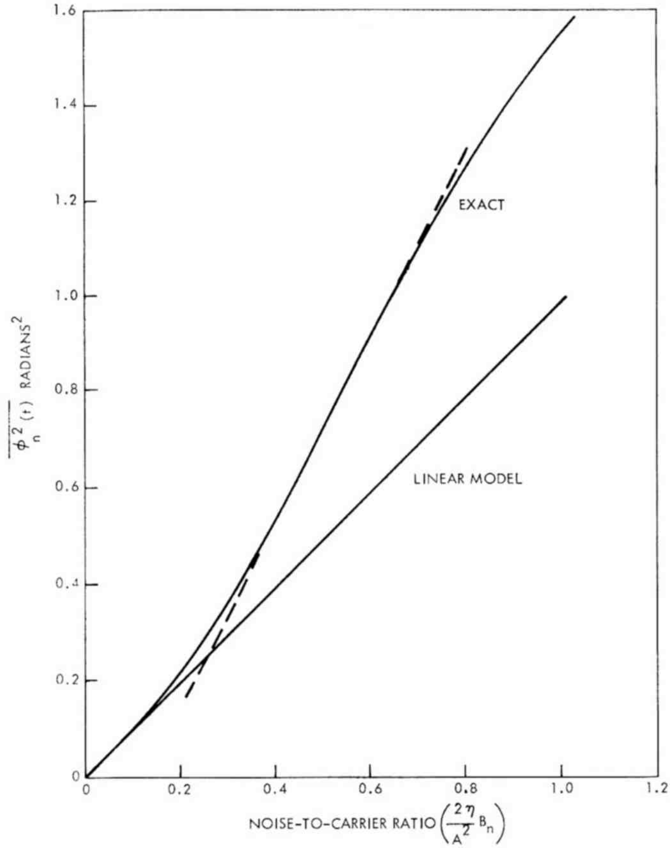

Fig. 13—Mean-square phase perturbation due to input noise-to-carrier ratio (from Viterbi).

or

$$\frac{A^2/2}{\eta B_n} = 5 = 7 \text{ db.} \tag{44}$$

The required noise bandwidth is determined from the modulation

---

[30] R. E. Heitzman, "A Study of the Threshold Power Requirements of FMFB Receivers," *IRE Trans. on Space Electronics & Telemetry*, Vol. SET-8, p. 249, Dec. 1962.

characteristics. From Equations (40) through (43):

$$\frac{Y}{\omega_n{}^4} = \frac{1}{20} \tag{45}$$

or

$$\omega_n = 2B_n = \left[20 \int_0^{f_b} \omega^4 |\Phi_1(j\omega)|^2 df \right]^{1/4}. \tag{46}$$

Y is evaluated for a speech-modulation case. The speech is characterized analytically as noise with a spectral distribution starting at 1 kHz falling off at 12 db/octave and terminating at 4 kHz. A peak factor of 10 db is assumed for the speech waveform (i.e., the transmitter limits its peak deviation to 10 db above the rms value).

The FM speech spectrum expression is

$$|\Phi_1(j\omega)| = \frac{\eta_m}{\omega^4} \; (\text{rad/s}^2)^2; \quad f_1 \leqq f \leqq f_b. \tag{47}$$

Thus

$$Y = \eta_m \, [f_b - f_1]. \tag{48}$$

The mean-square frequency modulation of the carrier $(\bar{\dot{\phi}})^2$ is

$$(\bar{\dot{\phi}})^2 = \int_0^{f_b} \omega^2 |\Phi_1(j\omega)|^2 \, df \tag{49}$$

$$= \frac{\eta_m}{(2\pi)^2} \left[\frac{1}{f_1} - \frac{1}{f_b} \right] (\text{rad/s})^2. \tag{50}$$

Combining Equations (48) and (50) yields

$$Y = \omega_1 \omega_b (\bar{\dot{\phi}})^2. \tag{51}$$

Substituting Equation (51) into (46) yields, with $\Delta\omega_{rms} = \sqrt{(\bar{\dot{\phi}})^2}$,

$$\omega_n = \sqrt[4]{20} \sqrt{\omega_r \Delta\omega_{rms}} \tag{52}$$

where $\omega_r = \sqrt{\omega_1 \omega_b}$ = geometric-mean base-band frequency for voice modulation. Substituting Equation (52) into the threshold Equation (44),

$$\frac{A^2/2}{2\eta f_r} = \frac{5\pi \sqrt[4]{20}}{2} \sqrt[4]{\frac{\Delta\omega_{rms}}{\omega_r}}. \tag{53}$$

or

$$p_n = \frac{A^2/2}{2\eta f_b} = \frac{5\pi \sqrt[4]{20}}{2} \sqrt[4]{\frac{f_1}{f_b}} \sqrt{\sigma} \tag{54}$$

The phase-lock demodulator is followed by a low-pass filter having a sharp cutoff at f_b. The transmitted noise power above threshold is

$$\begin{aligned} N_0 &= \frac{2\eta}{A^2} 4\pi^2 \int_0^{f_b} f^2\, df \\ &= \frac{2\eta}{A^2} 4\pi^2 \frac{f_b^3}{3} \text{ (rad/s)}^2. \end{aligned} \tag{55}$$

The output signal power is

$$S_0 = (\Delta\omega_{rms})^2 = 4\pi^2 \sigma^2 f_b^2, \tag{56}$$

where $\sigma = \Delta\omega_{rms}/\omega_b$ = rms modulation index. The output signal-to-noise ratio above threshold is

$$\text{SNR} = \frac{S_0}{N_0} = \frac{3\sigma^2 f_b A^2}{f_b^3 (2\eta)} = \frac{6\sigma^2 \frac{A^2}{2}}{2\eta f_b}, \tag{57}$$

$$\frac{S_0}{N_0} = 6\sigma^2 p_n, \tag{58}$$

$$p_n = \frac{A^2/2}{2\eta f_b}. \tag{59}$$

The threshold boundary is obtained by simultaneous application of Equations (54), (58), and (59):

$$(\mathrm{SNR})_{TH}|_{db} = 5\,[p_n|_{db}] - 41.04\ \mathrm{db} + 10\log\left(\frac{f_b}{f_1}\right). \qquad (60)$$

Substituting $f_b = 4$ kHz and $f_1 = 1$ kHz yields the performance curves of Figures 5 and 11 for the PLD.

APPENDIX C—CALCULATION OF THRESHOLD OF AN EXTENDED-RANGE PLD USING A MODIFIED PHASE-DETECTOR CHARACTERISTIC

The fundamental source of threshold in the PLD is the loss-of-lock phenomenon. As indicated in Appendix B the threshold of the conventional PLD is related to a specific input carrier-to-noise ratio (referred to the closed-loop noise bandwidth) and, referring to Viterbi,[28] indicates a specific loss-of-lock rate. The threshold extension capabilities of the extended-range PLD are determined by the allowable reduction of input carrier-to-noise ratio to sustain the loss-of-lock rate. The following calculation determines the loss-of-lock rate for an extended-range PLD that utilizes either the ideal saw-tooth or truncated-sine phase-detector characteristic. The loss-of-lock rate is equal to the reciprocal of the mean time to loss of lock. Viterbi calculates the mean time to loss of lock for the generalized (arbitrary phase-detector characteristic) first-order loop $[F(S) = 1]$. Here we apply the first-order loop calculations to obtain the performance gains in our extended-range second-order loops. Justification for this approximation lies in the fact that recent experimental results[31] show that the conventional (sinusoidal phase-detector characteristic) first-order PLD calculations (Viterbi) agree to within one db of those obtained in a conventional second-order PLD; exact analysis does not exist for the generalized second-order loop.

The mean time to loss of lock is equal to the mean time to reach 2π radians phase error if we assume the loop input is an unmodulated carrier and wideband gaussian noise.

Viterbi shows that the mean time to reach ϕ_e degrees of phase error (assuming $\phi = 0°$ initial phase error) is

$$T(\phi_e) = \frac{1}{\gamma}\int_0^{\phi_e}\int_{\phi}^{\phi_e} \exp\{-\alpha[g(\phi) - g(x)]\}\,dx\,d\phi \qquad (61)$$

---

[31] R. W. Sanneman and J. R. Rowbotham, "Unlock Characteristics of the Optimum Type II Phase-Locked Loop," *IEEE Trans. on Aerospace & Navigational Electronics*, Vol. ANE-11, p. 15, March 1964.

$$\text{where} \qquad \gamma = \frac{4B_n}{\alpha}; \quad g(\phi) = \int^{\phi} h(x)\,dx,$$

$B_n =$ noise bandwidth of the demodulator (one-sided),

$\gamma =$ input carrier-to-noise ratio referred to B_n,

$h(x) =$ phase-detector characteristic.

We continue by evaluating Equation (61) for the ideal saw-tooth and for the truncated-sine phase detector characteristics. For the case of the ideal saw-tooth, $T(2\pi) = 2T(\pi)$, and the calculation proceeds as follows:

$$g(\phi) = \frac{\phi^2 - \pi^2}{2}. \tag{62}$$

Then,

$$\begin{aligned} T(\pi) &= \frac{1}{\gamma} \int_0^{\pi}\int_{\phi}^{\pi} \exp\left\{-\frac{\alpha}{2}[\phi^2 - x^2]\right\} dx d\phi, \\ &= \frac{1}{\gamma}\int_0^{\pi}\left\{\int_{\phi}^{\pi} \exp\left(\frac{\alpha x^2}{2}\right) dx\right\} \exp\left(-\frac{a\phi^2}{2}\right) d\phi. \end{aligned} \tag{63}$$

By changing the order of integration and substituting $u = \sqrt{\alpha/2}\,x$, the integral reduces to

$$T(\pi) = \frac{\sqrt{\pi}}{\gamma\alpha}\int_0^{\pi\sqrt{\alpha/2}} \operatorname{erf} u \exp u^2\,du.$$

Solution of this integral can be found by expanding erf u into its series representation and integrating the resultant serial integrand, term by term. For large values of the limit of integration, the integrated series converges slowly and hence an asymptotic solution is desirable to evaluate $\mathrm{T}(\pi)$ at high input carrier-to-noise ratios. Assuming $\pi\sqrt{\alpha/2} \gg 1$, it is observed that the erf $u \rightarrow 1$ as $u \rightarrow \infty$ (and $\alpha \rightarrow \infty$), and as the major portion of the integral is contributed in the region of u approaching the limit $\pi\sqrt{\alpha/2}$, the following approximation is formed:

$$\underset{\alpha\to\infty}{T(\pi)} \doteq \frac{\sqrt{\pi}}{\gamma\alpha} \int_0^{\pi\sqrt{\alpha/2}} \exp u^2 \, du. \tag{64}$$

The asymptotic value of this integral is found by observing:

$$\underset{x\to\infty}{\text{limit}} \int_0^{\infty} e^{u^2} du = \frac{e^{x^2}}{2x}. \tag{65}$$

Substituting Equation (65) into Equation (64) yields the approximation

$$\underset{\alpha\to\infty}{T(\pi)} \doteq \frac{\exp\{\pi^2\alpha/2\}}{4B_n\sqrt{2\pi}\sqrt{\alpha}}$$

$$R_E = \text{Rate of losing lock} = \frac{1}{2T(\pi)}$$

$$\doteq B_n 2\sqrt{2\pi}\sqrt{\alpha}\exp\{-\pi^2\alpha/2\} \quad \text{as } \alpha\to\infty. \tag{66}$$

Viterbi shows the asymptotic normalized loss-of-lock rate (R_N) for the conventional PLD is

$$R_N \doteq \frac{4}{\pi} B_{nN} \exp\{-2\alpha_N\}. \tag{67}$$

where

B_{ne} = closed-loop noise bandwidth of the extended-range PLD,

α_N = input unmodulated CNR (referred to B_{nN}) of the conventional PLD,

B_{nN} = closed-loop noise bandwidth of the conventional PLD.

It is assumed that the loss-of-lock transient will have the same disruptive effect in the extended-range PLD as the conventional PLD, hence it is anticipated that the extended-range PLD will experience threshold at the same loss-of-lock rate as the conventional PLD.

The loss-of-lock rates for the two demodulators are equated and the threshold condition for the conventional PLD ($\alpha_N = 4$) (Appendix B) inserted into the above equation, yielding

$$\sqrt{\alpha_E}\exp\left\{-\frac{\pi^2}{2}\alpha_E\right\}=\frac{B_{nN}}{B_{nE}}\,\frac{\sqrt{2}\exp-8}{\pi\sqrt{\pi}}, \tag{68}$$

where α_E is the input unmodulated CNR (referred to B_{nE}) of the extended-range PLD.

From Appendix B, the optimized noise bandwidth, B_n, is related to the VCO phase jitter (or $1/\alpha$), at threshold, by

$$B_n=\frac{1}{2}\left[5\alpha\omega_1\omega_b\Delta\omega_{rms}\right]^{1/4}. \tag{69}$$

Hence, the ratio of optimized noise bandwidth for two second-order PLD's having different threshold sensitivities (assuming constant modulation parameters) is

$$\frac{B_{nE}}{B_{nN}}=\left[\frac{\alpha_E}{\alpha_N}\right]^{1/4}. \tag{70}$$

Thus, Equation (68) reduces to:

$$[\alpha_E]^{3/4}\exp\left\{-\frac{\pi^2}{2}\alpha_E\right\}=\frac{2\exp-8}{\pi\sqrt{\pi}}. \tag{71}$$

The solution of Equation (71) is facilitated by taking logarithms of both sides;

$$\alpha_E \doteq 1.9. \tag{72}$$

The threshold carrier-to-noise ratio for the optimized second-order loop (refer to Appendix B), as a function of α at the threshold is

$$p_n=\frac{A^2/2}{2\eta f_b}=\frac{5\pi\alpha[5\alpha]^{1/4}}{8}\sqrt{\frac{f_1}{f_b}}\sqrt{\sigma}. \tag{73}$$

The threshold equation for the extended-range PLD is, therefore ($\alpha_E = 1.9$),

$$p_n=6.5\left[\frac{f_1}{f_b}\right]^{1/4}\sqrt{\sigma}. \tag{74}$$

Referring to the voice model discussed in the text,

$$f_1 = 1\ \text{kHz},$$

$$f_b = 4\ \text{kHz}.$$

Therefore, the extended-range PLD threshold equation reduces to:

$$p_n = 4.6\sqrt{\sigma}. \tag{75}$$

Referring this carrier-to-noise ratio to the transmission bandwidth yields

$$p = 4.6 \frac{\sqrt{\sigma}}{[1 + \sqrt{10}\,\sigma]}. \tag{76}$$

Referring to Appendix B, the threshold improvement of the extended-range PLD utilizing the ideal saw-tooth phase detector characteristic with respect to the conventional PLD is 4.0 db.

We continue the calculations by analyzing the mean time to loss-of-lock for the PLD utilizing the truncated-sine phase-detector characteristic. From Equation (61) the mean time to reach 2π radians phase error (loss-of-lock condition) is

$$T(2\pi) = \frac{1}{\gamma} \int_0^{2\pi} \int_\phi^{2\pi} \exp\{-\alpha[g(\phi) - g(x)]\} dx d\phi. \tag{77}$$

Evaluation of $g(\phi)$ for the truncated-sine characteristic

$$\left.\begin{aligned} g_1(\phi) &= \int_{-\pi}^{\phi} 2 \sin \frac{x}{2}\, dx, \quad -\pi \leqq \phi \leqq \pi \\ g_2(\phi) &= \int_{\pi}^{\phi} 2 \sin \frac{x}{2}\, dx, \quad \pi \leqq \phi \leqq 3\pi \end{aligned}\right\} . \tag{78}$$

$$\left.\begin{aligned} g_1(\phi) &= -4 \cos \frac{\phi}{2}, \quad -\pi \leqq \phi \leqq \pi \\ g_2(\phi) &= +4 \cos \frac{\phi}{2}, \quad \pi \leqq \phi \leqq 3\pi \end{aligned}\right\} . \tag{79}$$

The integration is reduced, by virtue of the periodic nature of $g(\phi)$, and change of variables, $\mu = \phi/2$ and $\omega = x/2$, to:

$$T(2\pi) = \frac{4}{\gamma} \int_{-\pi/2}^{\pi/2} \int_{\mu}^{\pi/2} \exp\{4\alpha(\cos\mu - \cos\omega)\} d\omega d\mu. \tag{80}$$

This integral can be solved by the Fourier series representation;

$$\exp(4\alpha \cos \phi) = I_0(4\alpha) + 2 \sum_{m=1}^{\infty} I_m(4\alpha) \cos m\phi$$

$$\exp(-4\alpha \cos x) = I_0(4\alpha) + 2 \sum_{n=1}^{\infty} (-1)^n I_n(4\alpha) \cos nx, \tag{81}$$

which results in

$$T(2\pi) = \frac{4}{\gamma} \left[\frac{\pi^2 I_0{}^2(4\alpha)}{2} + 8 \sum_{m=1}^{\infty} \sum_{n=1}^{\infty} I_m(4\alpha) I_n(4\alpha) \frac{\left(\sin \frac{n\pi}{2}\right)\left(\sin \frac{m\pi}{2}\right)}{nm} \right]. \tag{82}$$

This rather complex expression can be evaluated in closed form for large input carrier-to-noise ratios (α very high). In this case, the modified Bessel functions asymptotically approach $I_0(4\alpha)$. Using this, and the fact that

$$\sum_{m=1}^{\infty}\sum_{n=1}^{\infty} \left(\frac{\sin \frac{m\pi}{2}}{m} \right) \left(\frac{\sin \frac{n\pi}{2}}{n} \right) = \frac{\pi^2}{16},$$

gives

$$T(2\pi) = \frac{4}{\gamma} \left[\frac{\pi^2 I_0{}^2(4\alpha)}{2} + \frac{8\pi^2 I_0{}^2(4\alpha)}{16} \right]$$

$$= \frac{4}{\gamma} \left[\pi^2 I_0{}^2(4\alpha) \right] = \frac{1}{\gamma} \left[4\pi^2 I_0{}^2(4\alpha) \right]. \tag{83}$$

Recall that $\gamma = 4B_n/\alpha$. Also, for large α, $I_0(4\alpha) \approx e^{4\alpha}/[2\pi\sqrt{4\alpha}]$. Therefore

$$T(2\pi) = \frac{\alpha}{4B_n} \frac{4\pi^2 e^{8\alpha}}{2\pi(4\alpha)} = \frac{\pi e^{8\alpha}}{8B_n}. \tag{84}$$

The normalized loss-of-lock rate (R_E) for the extended-range PLD is then

$$\frac{1}{T(2\pi)} = R_E = \frac{8B_n}{\pi} \exp - 8\alpha_E. \tag{85}$$

Setting this equal to the conventional PLD loss-of-lock rate (Equation (67)) at $\alpha_n = 4$ and utilizing Equation (69) results in

$$\alpha_E \doteq 1.06. \tag{86}$$

Since the conventional PLD loses lock at $\alpha' = 4$, this extended range PLD (that utilizes the truncated-sine phase-detector characteristic) is seen to be nearly 7 db better in threshold performance than the conventional PLD.

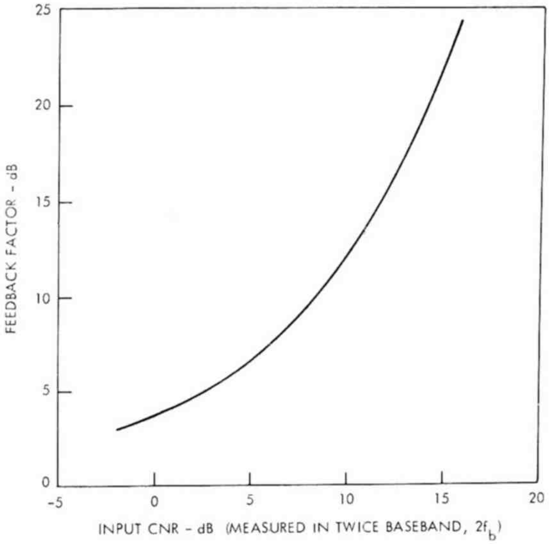

Fig. 14—Feedback threshold characteristic for the FMFB demodulator.

APPENDIX D—CALCULATION OF THRESHOLD SENSITIVITY FOR THE HYBRID FMFB DEMODULATOR

The Enloe design is based upon equating the two threshold mechanisms that are characteristic of the FMFB demodulator. This is accomplished graphically by simultaneous plotting of the feedback threshold p_{nF} as a function of the feedback factor F, and the threshold of the internal demodulator as a function of the input modulation index. The intersection of the characteristic curves yields the minimum threshold design. The feedback threshold characteristic is taken from Enloe and plotted in Figure 14.

The threshold characteristic equation, as derived in Appendix B for the PLD, is

$$p_n = \frac{5\pi[20]^{1/4}}{2} \left[\frac{f_1}{f_b} \right]^{1/4} \sqrt{\sigma}, \tag{87}$$

where $\sigma =$ input rms modulation index and $f_1 = 1$ kHz; $f_b = 4$ kHz from the noise model postulated to represent speech. Equation (87) reduces to:

$$p_n = \frac{5\pi}{2} [5]^{1/4} \sqrt{\sigma}. \tag{88}$$

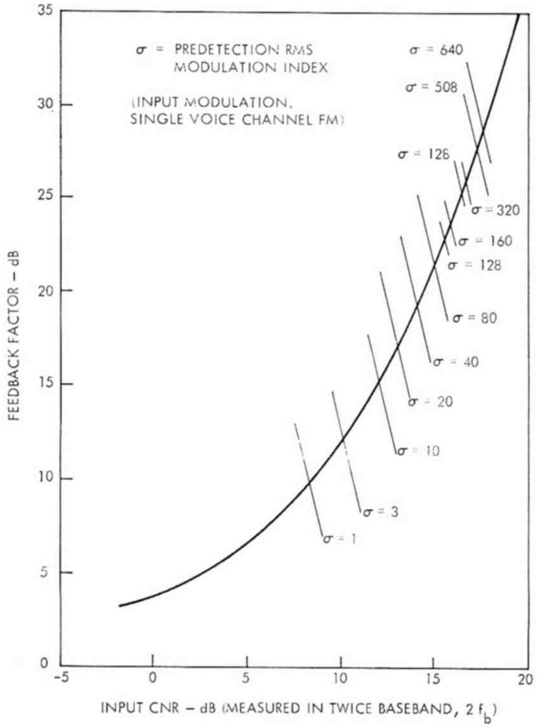

Fig. 15—Determination of threshold compound FMFB-PLD demodulator.

As the PLD is demodulating the compressed input deviation, the PLD threshold characteristic, as related to the uncompressed input modulation index, is

$$p_n = \frac{5\pi}{2} [5]^{1/4} \sqrt{\frac{\sigma}{F}}, \tag{89}$$

where F is the feedback factor incorporated in the FMFB design. Figure 15 determines the intersection of the feedback threshold characteristic and the PLD threshold characteristic. The threshold boundary represented in Figure 11 is determined from Equation (58), relating input modulation index to output signal-to-noise ratio, and Figure 15.

FMFB—Extended Range PLD Hybrid Demodulator

The threshold characteristic equation of the extended-range PLD, as derived in Appendix C, is

$$p_n = 4.6\sqrt{\sigma}. \tag{90}$$

As the PLD is demodulating the compressed input deviation, the extended-range PLD threshold characteristic, as related to the uncompressed input modulation index, is

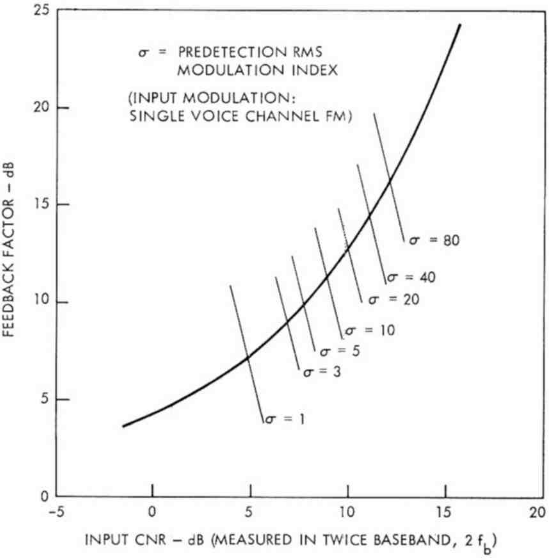

Fig. 16—Determination of threshold compound FMFB-ERPLD demodulator.

$$p_n = 4.6\sqrt{\sigma/F}, \tag{91}$$

where F is the feedback factor incorporated in the FMFB design. The intersection of the feedback threshold characteristic and the extended-range PLD threshold characteristic is determined from Figure 16. The output signal-to-noise ratio at threshold is determined from Equation (58) (Appendix B). The results of Figure 16, and the output signal-to-noise ratio calculation yield the threshold boundary in Figure 11.

FMFB-PLD Hybrid Demodulator

From Figure 11 it is possible to determine the threshold characteristic equation for the FMFB demodulator. The threshold characteristic equation is

$$p_n = 9.52[\sigma]^{0.6}. \tag{92}$$

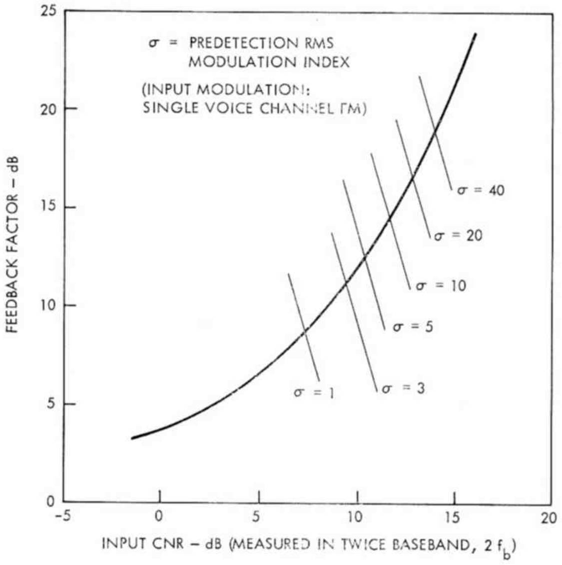

Fig. 17—Determination of threshold compound FMFB-FMFB demodulator.

Since the internal FMFB demodulates the compressed input deviation, the internal FMFB demodulator threshold characteristic, as related to the uncompressed input modulation index, is

$$p_n = 9.52[\sigma/F]^{0.6}, \tag{93}$$

where F is the feedback factor incorporated in the outer FMFB design. As in the previous two calculations, the internal demodulator characteristic equation is equated graphically to the outer loop threshold characteristic, as shown in Figure 17. The result of the graphical analysis, in conjunction with Equation (58) of the Appendix, yields the threshold boundary in Figure 11 of the text.

It is emphasized that the validity of this graphical analysis depends upon meeting the requirement in $H(j\omega)$ (the loop filter for the outer loop) that the closed-loop response of the inner loop is compensated to yield the overall maximally flat Butterworth response in the outer loop. Since the inner loop is designed as a second-order demodulator, this requirement is not difficult to realize if the base-band filtering is distributed between base-band isolation stages.

THE FREQUENCY-MODULATION FEEDBACK SYSTEM FOR THE LUNAR-ORBITER DEMODULATOR*

BY

F. LEFRAK, H. MOORE, A. NEWTON, AND L. OZOLINS

RCA Communications Systems Division
New York, N. Y.

Summary—*The frequency-modulation feedback (FMFB) system described is designed to demodulate the Lunar Orbiter signal with low threshold and distortion. A distinct feature of the FMFB system is optimization for the Lunar Orbiter signal characteristics. The baseband signal consists of a video channel impressed on a 310-kHz subcarrier transmitted through a vestigial-sideband filter, and telemetry and pilot-tone information in the 30- to 40-kHz range. The composite signal phase modulates the r-f carrier with an index of 4.0 radians, of which the subcarrier takes 3.6 radians. This mode of transmission results in large deviation energy associated with high modulation frequencies (near 310 kHz). The effect of modulation on threshold is significant, and a departure from conventional design was required.*

Performance results show 7 db carrier-to-noise ratio at threshold, measured in 3.3 MHz bandwidth. Total harmonic and intermodulation distortion is down more than 46 db. The functional design and outstanding circuit features are described, and the FMFB frequency response is analyzed.

INTRODUCTION

THE UNMANNED Lunar Orbiter satellite transmits high-resolution pictures of likely landing targets on the moon, as well as telemetry data. It employs phase modulation to impress intelligence on an r-f carrier.

A frequency-modulation feedback (FMFB) demodulator, whose design and performance characteristics are described in this paper, was developed for the Lunar-Orbiter ground-station equipment to recover the transmitted intelligence. The advantage of a feedback demodulator over a conventional discriminator in a receiver for angle-modulated signals is a reduction in input carrier-to-noise ratio (CNR) at which threshold (significant reduction of the noise improvement factor) occurs. This permits a reduction in transmitter power and thus a reduction in spacecraft weight.

A comparative analysis of available FM demodulators, based on theoretical estimates and available experimental evidence, revealed

---

* This work was performed on NASA Contract NAS-1-3800.

FMFB to be superior for the Lunar Orbiter. The available literature on FMFB theory, however, is incomplete in that it does not treat the effect of modulation on threshold. To date, this problem has not been amenable to analysis. Furthermore, the effect of modulation is not so significant under usual conditions in which modulation peaks are not statistically related to high baseband frequencies. In the case of the Lunar-Orbiter signal, however, the presence of the subcarrier results in the system being subject to large sine-wave deviation at 310 kHz, which is high in the baseband.

LUNAR-ORBITER BASEBAND SIGNAL

The information bandwidth of the Lunar-Orbiter video signal covers the range from 0 to 230 kHz. Prior to modulating the carrier transmitted by the spacecraft transponder, this signal amplitude-modulates a subcarrier at 310 kHz to facilitate accurate transmission of a video d-c component. This is necessary because phase modulation is employed in the spacecraft, the carrier being derived from the ground. Balanced subcarrier modulation is utilized, but the presence of a d-c video component can result in a 310-kHz tone with full subcarrier amplitude appearing in the baseband output signal. To minimize signal bandwidth, the subcarrier signal is passed through a vestigial-sideband filter that restricts significant upper-sideband energy to 390 kHz. The choice of subcarrier frequency provides a region from 0 to 80 kHz for insertion of pilot tone and telemetry information. It also allows maximum utilization of the 4-radian peak-deviation capability of the modulator, while restricting the r-f signal to the assigned 3.3-MHz system bandwidth.

Peak phase deviation for the video information is 3.6 radians, equivalent to 1.12 MHz frequency deviation at 310 kHz. The pilot tone is at 38.75 kHz, which is one-eighth the subcarrier frequency; this tone is required for synchronous demodulation of the video signal. The telemetry channel, at 30 kHz, carries non-return-to-zero (NRZ) data. The deviations due to the pilot tone and telemetry are each limited to 0.2 radian. Hence, the video channel parameters are the most significant in relation to system performance capabilities. Specifically, the FMFB demodulator must be designed to accept an input signal modulated by a 310-kHz tone at 3.6 radians peak deviation. It is the presence of this 310-kHz tone that stresses the loop most severely.

The composite baseband spectrum is illustrated in Figure 1. The three components are separated by filtering, and the video portion is integrated to give constant amplitude response for constant input phase modulation of the video subcarrier signal. These processes occur after the signal leaves the FMFM demodulator and are not considered in the present discussion.

Experiment has verified that the classical FMFB design procedures lead to a system that is significantly degraded in the presence of the Lunar-Orbiter modulation. An experimental program was undertaken to establish the optimum FMFB loop parameters for the specified signal. This paper describes experimental findings of that program.

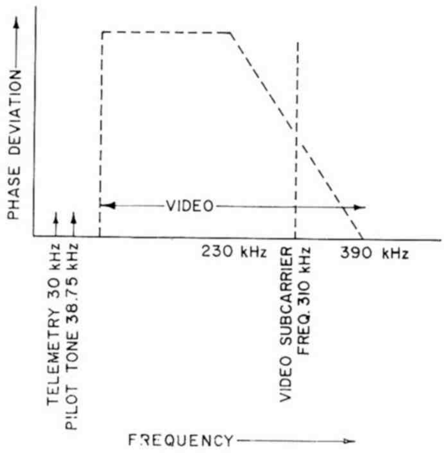

Fig. 1—Composite baseband spectrum.

SYSTEM DESCRIPTION

The FMFB demodulator is designed to accept a 10-MHz i-f input signal and to deliver a 2-volt rms baseband output signal under reference conditions of a 230-kHz modulating tone and a 3.6-radian peak phase deviation. The block diagram in Figure 2 shows the loop preceded by a predetection filter and an a-g-c amplifier, and followed by an output amplifier capable of driving a 75-ohm load.

The predetection filter is an integral part of the demodulator. Because it band-limits noise components falling within the closed-loop response of the FMFB, it is a factor in threshold performance. Specifically, for the 5-MHz noise bandwidth utilized in the predetection filter, the threshold is improved by 0.5 db relative to a wide-band input. Group-delay distortion sets a limit to predetection band limiting. A three-pole Butterworth filter was used without equalization.

For optimum threshold performance over a range of system input levels, the level at the input to the loop must be accurately regulated so as to prevent clipping on noise peaks in the mixer. At the same time there must be adequate signal clipping in the limiter. The a-g-c amplifier acts to reduce input variation to ±0.5 db.

The balanced mixer is effective in suppressing the 55-MHz voltage-controlled-oscillator (VCO) drive, which is close in frequency to the loop i-f. The input signal and VCO power applied to the mixer, —20 and +2 dbm, respectively, are chosen to minimize generation of spurious components. Of particular significance are the fourth and fifth harmonics of the input, which fall close to the 45-MHz i-f. Excessive spurious amplitude would degrade the noise-improvement factor (the ratio of output SNR to input CNR above threshold) as well as threshold and distortion performance.

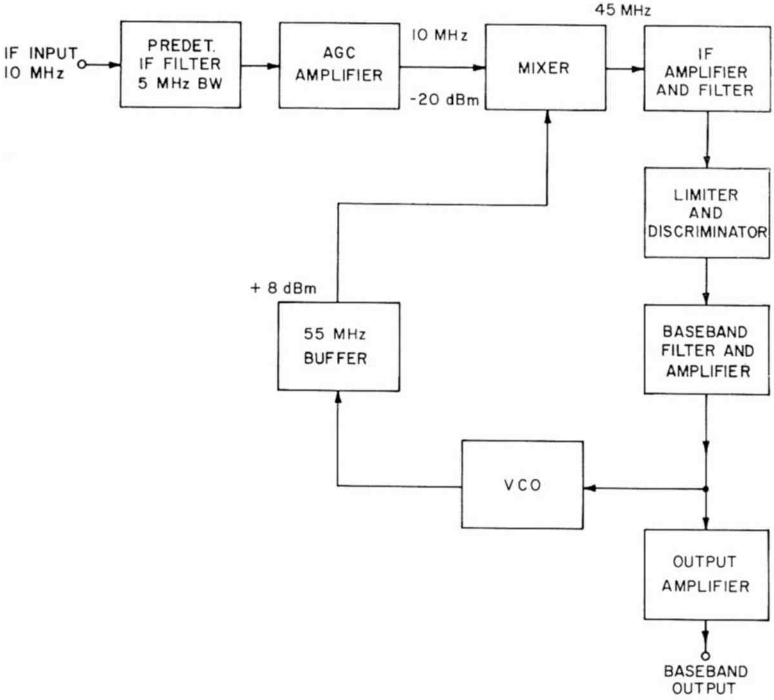

Fig. 2—Block diagram of the Lunar Orbiter FMFB demodulator system.

The single-pole band-pass filter is incorporated into the i-f amplifier. Except for this filter, the entire system must exhibit wide bandwidth and low delay. The limiter output amplitude varies 0.2 db for a 6-db input variation. The system gain is proportional to the level at which the limiter drives the discriminator; therefore a limiter output adjustment is used to control the feedback factor. The sensitivity of the discriminator is nominally 50 millivolts per MHz. Peak-to-peak separation of the discriminator is 20 MHz.

The baseband filter is a passive network feeding the baseband amplifier, which drives both the VCO and the output amplifier. The baseband gain of 1.8 and VCO sensitivity of 30 MHz per volt yield a feedback factor of 3.9. The range of gain (indicated in Table I) is obtained by adjusting limiter output.

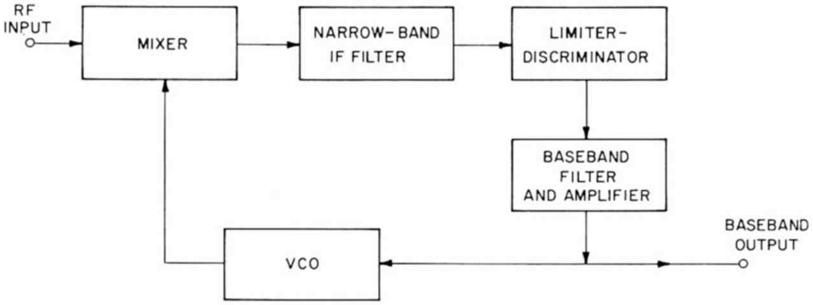

Fig. 3—Block diagram of an FMFB demodulator.

The VCO is transistorized and employs varactor control of two UHF oscillators modulated in push-pull. This arrangement has the advantages of cancelling even-order distortion and doubling the VCO sensitivity. The VCO output is generated in a mixer (part of the VCO block in Figure 2), and is amplified 24 db in the 55-MHz buffer. The buffer has a bandwidth of 70 MHz and exhibits low delay.

The output amplifier, employing feedback, accepts a 16-millivolt signal from the baseband amplifier and boosts it to 2 volts rms with sufficient power to feed a 75-ohm load. The total harmonic distortion in the output amplifier is 60 db down. The output amplifier incorporates a simple amplitude and delay equalizer to maintain the amplitude within 0.5 db and the phase-delay variation within 200 nanoseconds.

FMFB DESIGN

Threshold reduction is achieved in the FMFB demodulator in Figure 3 by virtue of reduced deviation, which permits transmission of the compressed signal through a narrow-band-pass filter prior to detection. The threshold of the limiter–discriminator combination, for which theory is well established, is lower than in a demodulator not utilizing negative feedback.

Deviation in the FMFB demodulator is compressed in proportion to the feedback factor F, defined as the open-loop gain plus one. The bandwidth of the band-pass filter in the loop is important, since it determines the noise power presented to the limiter. It is related to the base bandwidth, f_b, and to the compressed modulation index, M/F (M is the input-signal index). The exact relationship depends, to some extent, on performance criteria. A conservative approach is to utilize Carson's Rule for the 3-db bandwidth, B_s;

$$B_s = 2f_b \left(1 + \frac{M}{F} \right). \tag{1}$$

An alternative criterion recognizes the effect of feedback in reducing distortion caused by attenuation or phase shift of sideband components in a filter. This yields smaller bandwidth, hence lower threshold;

$$B_s = 2f_b \left(\frac{M}{F} \right). \tag{2}$$

These two bandwidth criteria are advanced by Enloe.[1] An intermediate bandwidth is found useful in a tradeoff between threshold and distortion performance;

$$B_s = 2f_b \left(\frac{1}{2} + \frac{M}{F} \right). \tag{3}$$

The designs utilizing the i-f bandwidth criteria of Equations (1)-(3) are designated Carson's Rule, Minimum CNR, and Transitional, respectively.

It is convenient and meaningful to express threshold in terms of CNR, normalized to $2f_b$, as a function of F with M as a parameter. Curves for this "open-loop threshold" are shown in Figure 4 for $M = 3.6$.

Another threshold mechanism present in the FMFB demodulator is due to the application of feedback. No analysis has appeared in the literature to account completely for this mechanism, known as feedback threshold, in a quantitative way. Additive input noise is transferred to baseband by the loop discriminator and modulates the VCO. The resulting VCO phase jitter mixes with the input carrier and noise to produce noise modulation in the loop i-f. There is an uncorrelated

---

[1] L. H. Enloe, "The Synthesis of Frequency Feedback Demodulators," *Proc. Nat. Electronics Conference*, Vol. 18, Chicago, Ill., 1962.

component of VCO jitter that is not suppressed by feedback action. As the input CNR is lowered, a point is reached at which the loop fails to track the input signal, and impulses appear in the baseband signifying approach of the feedback threshold.

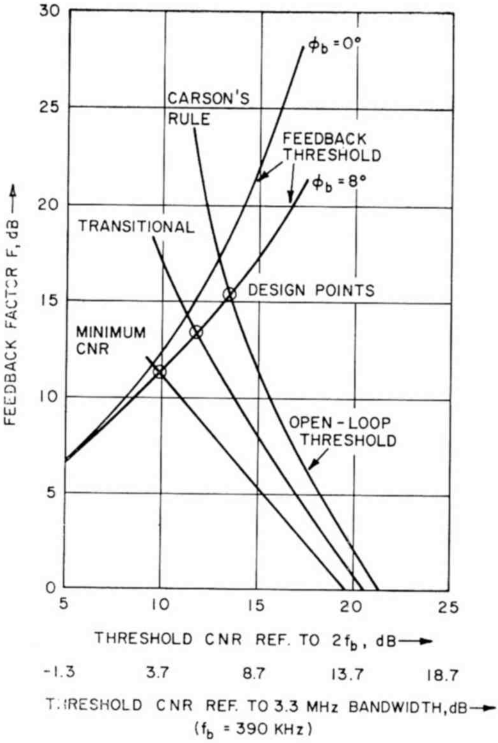

Fig. 4—FMFB design curves, $M = 3.6$.

Enloe found[2] that, for frequency-feedback receivers having a broad range of design characteristics, the mean-squared noise-induced phase jitter at the VCO output is close to 0.1 $(\text{radian})^2$ at threshold. He shows[1] that the CNR referred to the closed-loop noise bandwidth depends only upon F, so that once this bandwidth is known for a particular loop design, the feedback threshold may be plotted versus F. Enloe's feedback threshold curves are plotted on the same set of axes as the open-loop threshold curves in Figure 4. The two thresholds are nearly independent and an optimum is realized when the two thresholds occur at the same value of CNR, i.e., where the feedback-threshold

---

[2] L. H. Enloe, "Decreasing the Threshold in FM by Frequency Feedback," *Proc. IRE*, Vol. 50, p. 18, Jan. 1962.

curve intersects the curve of open-loop threshold corresponding to the desired design. Note that the feedback threshold does not depend upon i-f bandwidth; the i-f filter response is canceled by the baseband filter in the Enloe design. Different curves are required, however, for different values of loop delay or excess phase shift, ϕ_b, at top baseband frequency, since the closed-loop bandwidth depends upon this quantity.

Table I—Loop Parameter for Various Designs

	Carson's Rule	Transitional	Min. CNR	Final
Feedback Factor, F (decibels)	15.7	13.3	10.9	11.8
Feedback Factor, F (ratio)	6.1	4.6	3.5	3.9
Open-Loop Gain (ratio)	5.1	3.6	2.5	2.9
Threshold CNR, db (referred to 3.3 MHz i-f noise bandwidth)	7.2	5.2	3.7	7.0 (meas. value)
		Enloe Predictions		
Loop i-f 3 db Bandwidth, B_s (MHz)	1.24	1.0	0.80	1.2
Closed-Loop Noise Bandwidth (MHz)	3.12	2.34	1.72	2.15

Completing the description of the Enloe design procedure, a constant feedback factor over the baseband f_b is desired for uniform compression of the i-f signal. This condition is reasonably well satisfied with sufficient stability margin by choosing a second-degree maximally flat (Butterworth) characteristic for the open-loop transfer function. This is incorporated into the baseband filter. Included also is a zero to cancel the single-pole i-f filter response, as represented by its low-pass analog. Above threshold, validity of a low-pass analog for the loop depends upon compression of the i-f signal to an AM bandwidth, i.e., only first-order sidebands have significant amplitude. Finally, a zero is included to minimize the closed-loop noise bandwidth. The frequency of this zero depends upon the value of ϕ_b. Enloe used a computer routine to establish the zero that yields minimum noise bandwidth, and has published tabulated results.[1]

The initial Lunar-Orbiter FMFB design was conducted according to the Enloe synthesis described above, with loop parameters approximately determined by the Transitional design criterion. These parameters are listed in Table I, together with those for the Carson's Rule and Minimum CNR designs. Also shown in Table I are the loop parameters for the final design, the development of which will be described.

THRESHOLD PERFORMANCE IN THE PRESENCE OF MODULATION

Threshold performance was determined experimentally by applying to the input of the FMFB demodulator a carrier modulated by a 310 kHz tone at 3.6 radians peak deviation, together with additive noise that is bandlimited to 5 MHz. Signal and noise were measured at the output of a sharp-cutoff filter with bandwidth extending from 80 to 390 kHz. For the output noise measurement, a narrow band-stop filter rejects the modulating tone. From a plot of output SNR versus input CNR, threshold is found as the value at which SNR drops 1 db from the unity-slope asymptote (db versus db) to the curve above the threshold.

This measurement technique yields threshold data in the presence of modulation. With the initial Transitional design described above, the measured threshold CNR was as much as 4 db greater than predicted. In absence of modulation (no modulating signal at the transmitter during the FMFB output noise measurement), threshold was within about 1 db of the predicted value. Threshold extension, relative to a conventional discriminator, was thus substantially reduced under realistic operating conditions. Thus, for optimal threshold design under representative conditions, the effect of modulation on loop dynamics must be considered.

In accounting for the presence of modulation, Enloe's two optimized designs do include full compression across the baseband frequency range. However, if compression becomes deficient in a region of the baseband spectrum that contains considerable energy, which is the case for the Lunar-Orbiter signal, deterioration of threshold becomes more pronounced. Full compression is not realized in the higher baseband region because of phase shift and amplitude rolloff in the open-loop response. The formal Enloe design ignores the effect of modulation. In particular, the feedback threshold is strongly influenced by modulation. A critical quantity appears to be the loop frequency error due to the combined effects of noise and modulation. With greater contribution from the modulating signal, less noise is tolerated before the loop fails to track the input frequency, and the feedback threshold occurs at a larger CNR.

An analysis by Davis[3] shows that the loop has a limited dynamic

---

[3] B. R. Davis, "Factors Affecting the Threshold of Feedback FM Detectors," *IEEE Trans. on Space Electronics and Telemetry,* Vol. SET-10, No. 3, p. 90, Sept. 1964.

range over which negative (stable) feedback is obtained. Outside this range, determined by CNR in addition to the i-f filter bandwidth, feedback becomes positive. Instantaneous modulation-plus-noise excursions beyond the stable range cause a re-locking transient to be generated. This restriction on dynamic range is over and above the static response limitations of the conventional discriminator.

Loop performance would be improved by decreasing modulation error and increasing the loop tracking range. This can be accomplished by increasing the loop gain or the loop i-f filter bandwidth. Increasing the gain increases the closed-loop noise bandwidth more rapidly; hence, it is preferable to increase the filter bandwidth. The open-loop threshold is degraded by this adjustment, but the spread between thresholds in the absence and in the presence of modulation is reduced, resulting in a compromise design.

With respect to the additive effects of signal and noise errors, the situation is analogous to that in the phase-locked loop wherein the phase detector has a limited range of input phase difference over which its transfer characteristic has the correct slope for negative feedback. When this range is exceeded by a combination of baseband signal and noise phase modulation of the VCO, positive feedback causes a re-locking transient to occur in the loop.

An experimental program was undertaken to optimize the design so that the presence of modulation would result in least threshold degradation. Best results were obtained with moderate feedback factor, minimum loop i-f filter bandwidth consistent with low measured distortion, and a slightly peaked open-loop response rather than the flat characteristic of the initial design. The resulting closed-loop noise bandwidth was low. In the final design, 7.0 db CNR at threshold referred to 3.3-MHz bandwidth has been achieved in the presence of a tone representing the full-amplitude video subcarrier.

Comparing the final design with the initial approaches shown in Table I, optimum performance requires a low feedback factor appropriate for Minimum CNR design, but a wider i-f filter bandwidth. Although the bandwidth value approximates that for the Carson's Rule design, the fit is tighter because of the reduced compression.

In the experimental procedure for minimizing threshold CNR the loop gain and the i-f and baseband filter constants were varied, but the number of poles and zeros employed by Enloe was retained. Specifically, we examine the combined response of the i-f filter low-pass analog $A_L(j\omega)$ and the baseband filter $H_0(j\omega)$:

$$A_L(j\omega)H_0(j\omega) = \frac{1}{\dfrac{j\omega}{b\omega_b}+1}\cdot\frac{\left(\dfrac{j\omega}{a\omega_b}+1\right)\left(\dfrac{j\omega}{c\omega_b}+1\right)}{\left(\dfrac{j\omega}{\omega_b}\right)^2+2d\left(\dfrac{j\omega}{\omega_b}\right)+1}. \tag{4}$$

In an Enloe design, $c = b$, i.e., one zero of the baseband filter is made to coincide with the i-f pole. Also, the damping factor $d = \sqrt{2}/2$, yielding a Butterworth response as determined by the complex poles in the baseband filter.

Table II—I-F and Baseband Filter Data

	Carson's Rule	Transitional	Min. CNR	Final
Natural frequency of complex-pole response, f_b	390 kHz	390 kHz	390 kHz	338 kHz
Complex-pole damping factor, d	0.707	0.707	0.707	0.48
I-F filter zero	1.59 f_b	1.28 f_b	1.03 f_b	1.78 f_b
Baseband filter zeros	1.59 f_b 4 f_b	1.28 f_b 4 f_b	1.03 f_b 4 f_b	2.06 f_b 2.71 f_b

The filter response function in the final design, which gives the best threshold performance in the presence of modulation, is expressible in terms of Equation (4), when ω_b coresponds to 338 kHz:

$$A_L(j\omega)H_0(j\omega) = \frac{1}{\dfrac{j\omega}{1.78\omega_b}+1}\,\frac{\left(\dfrac{j\omega}{2.71\omega_b}+1\right)\left(\dfrac{j\omega}{2.06\omega_b}+1\right)}{\left(\dfrac{j\omega}{\omega_b}\right)^2+0.96\left(\dfrac{j\omega}{\omega_b}\right)+1}. \tag{5}$$

Equation (5) shows that the i-f pole is not canceled by a baseband filter zero in the final design, both zeros occurring at higher frequencies. These are at lower frequencies than the compensating zero called for in the Enloe synthesis, however. The damping factor is only 0.48. Filter parameters are summarized in Table II.

Loop delay, which has a bearing on threshold performance, was measured to be 90 nanoseconds. This is equivalent to $\phi_b = 12.7°$ per baseband of 390 kHz.

To summarize, the experimental evidence indicates that in the presence of modulation, the superimposed tracking error due to signal becomes significant. Increasing the i-f bandwidth reduces this error and entails a smaller threshold penalty than increasing loop gain. This process results in an increased open-loop threshold. Reduced gain results in a smaller closed-loop bandwidth and lower closed-loop threshold.

DISTORTION AND OTHER PERFORMANCE CHARACTERISTICS

Distortion in the baseband output of the FMFB demodulator is due to non-ideal transfer functions of various components of the loop. Nonlinearities in these components fall into two categories—static nonlinearity and nonlinear phase response. Static nonlinearities involve departure from constancy of the VCO and discriminator sensitivities and the baseband amplifier gain over the dynamic range of the signal. If these nonlinearities are controlling, they may be reduced to an arbitrary extent by design refinements.

Nonlinear phase response in the loop i-f filter presents a more fundamental limitation. Distortion from this source, associated with the angle modulation on the i-f signal, is not evident from examination of the low-pass model. As the i-f filter is ultimately the only source of baseband distortion, it is useful to estimate the expected contribution from this source.

The i-f filter has a single-pole response, which makes it amenable to distortion analysis. According to the Enloe design procedure described above, the "fit" of the compressed i-f signal to the filter is as follows. For the Carson's rule design the feedback factor F is 15.7 db (for $\phi_b = 8°$), the compressed modulation index M/F is 0.59, and the maximum frequency deviation (at 310 kHz) is 0.183 MHz peak. Correcting for a 1.5-db drop in open-loop gain at 310 kHz, the maximum deviation is 0.210 MHz peak. The 3-db bandwidth B_s of the i-f filter is 1.24 MHz.

Similarly, for the minimum CNR design $F = 10.9$ db, $M/F = 1.03$, and the corrected maximum frequency deviation at 310 kHz is 0.357 MHz peak. B_s is 0.80 MHz. For the final design, $F = 11.8$ db, $M/F = 0.92$, and the maximum deviation at 310 kHz (no correction is needed for drop in gain) is 0.287 MHz peak. B_s is 1.2 MHz.

Distortion values are taken from Figures 3 and 6 of Izatt,[4] utilizing

---

[4] J. B. Izatt, "The Distortion Produced When Frequency-Modulated Signals Pass Through Certain Networks," *Proc. IEE* (British), Vol. 110, p. 149, Jan. 1963.

the above data. An open-loop condition is hypothesized, in which a carrier modulated with a 310-kHz tone at the compressed deviation given above is passed through the pertinent i-f filter, an ideal limiter and discriminator, and the baseband filter. Third, harmonic distortion (the most significant harmonic in the discriminator output) is down 63 db from the 310-kHz fundamental for the Carson's rule design of Enloe, 45 db for the minimum $(\mathrm{CNR})_{\mathrm{T}}$ design, and 54 db for the final design. At the FMFB output, the distortion is reduced by the relative response of the pertinent baseband filter to 310 kHz and 930 kHz, and by the feedback factor. The resultant distortion values for the three designs are 91, 71.5, and 77 db, respectively.

In measuring harmonic distortion in the frequency-feedback discriminator, a 310-kHz tone was used to modulate the input carrier at 3.6 radians peak deviation. This represents the worst case with respect to accommodation by the loop i-f filter response and to closed-loop tracking ability. The ratio of fundamental to second-harmonic output is 52.2 db, and fundamental to third harmonic is 49.1 db. The rms sum of these distortion components is 47.4 db down.

It is emphasized that these calculations relate to a system wherein the only distortive element is the single-pole filter and that otherwise exhibits static and dynamic linearity. They serve to establish a tolerance on the signal fit within the filter. For example, the Minimum CNR design is inadequate since it leads to a product only 37 db down.

In practice, of course, these very low levels of distortion are not realized, as the other loop elements, principally the VCO and discriminator, limit the performance.

The over-all FMFB response, including the post-loop filter, was measured to be flat within ±0.25 db over the baseband to 390 kHz. Phase-delay variation over this range is less than 200 nanoseconds.

The noise improvement factor, i.e., the difference in db between output SNR and input CNR, is within 0.5 db of the 19.6-db theoretical value for $M = 3.6$.

CONCLUSIONS

Present design procedures for FMFB systems do not account adequately for the presence of modulation. Their application compromises the performance of the demodulator presented with the Lunar Orbiter signal and additive noise.

Best results were obtained with the wide single-pole bandwidth approximating the Carson's Rule design, and low feedback factor approximating the Minimum CNR design. This combination yields a reduced closed-loop bandwidth and good tracking capability.

Distortion was substantially lower than would be realizable using the Minimum CNR design.

ACKNOWLEDGMENT

The contributions of S. Friedman in design, development, and optimization of the production prototypes for the ground station receiver are hereby acknowledged. The encouragement and assistance of S. J. Mehlman is also acknowledged.

USE OF PHASE SUBTRACTION TO EXTEND THE RANGE OF A PHASE-LOCKED DEMODULATOR

BY

A. ACAMPORA AND A. NEWTON

RCA Communications Systems Division
New York, N. Y.

Summary—*A theoretical and experimental evaluation of a technique for reducing threshold in a phase-locked loop is presented. Threshold in a phase-locked discriminator (PLD) is related to loss-of-lock, which occurs when the instantaneous phase difference between the input carrier and the return voltage-controlled-oscillator (VCO) signal exceeds the locking range of the loop. For the conventional PLD, this range is ±90°.*

By retarding the phase of the return signal from the VCO to the phase detector, it is possible to extend the range of locking phase error between signal and VCO voltage beyond ±90°, thereby achieving threshold extension. This paper describes an extended-range PLD (ERPLD) using phase subtraction. Theoretical design considerations are discussed, and threshold performance of a voice-channel demodulator designed for a deviation ratio of three is examined. The results are compared with those of the conventional limiter–discriminator and the PLD.

INTRODUCTION

IN THE phase-locked loop, the return signal derived from a voltage-controlled oscillator (VCO) tracks the input signal with a finite phase error. The control voltage at the VCO contains base-band information from the angle-modulated input signal.

If the dynamic tracking range of the linear phase-locked system were not limited, the output noise would be that produced by phase jitter of the input signal, free of any additive component injected by the demodulator. In practice, the dynamic range of tracking phase error is limited, and a loss-of-lock output component is generated whenever the instantaneous phase error between input and return signals exceeds this loop tracking range. For a conventional loop this range is $\pm\pi/2$ radians. The relocking transient causes additive impulsive noise within the loop at the output of the phase detector. The strength of the impulse is 2π if the loop relocks in one cycle of the input wave.

Threshold phenomena can be related to the loss-of-lock effect. As the loss-of-lock rate increases, the impulsive component of noise becomes a significant fraction of the total output noise, and the approach of threshold is manifested by a reduction of the noise-improvement factor (NIF) for angle modulation. The loss-of-lock probability is inversely related to the input carrier-to-noise ratio (CNR) and the range of lock.

The demodulator described in this paper realizes a reduced loss-of-lock probability and lower threshold by extending the dynamic range of lock. The method employed involves controlled phase subtraction in the path of the VCO return signal. The linear model of this extended-range phase-locked discriminator (ERPLD) is presented, the static response of the phase detector as a function of the significant gain parameters is examined, linearity and threshold properties are analyzed, and experimental results for a voice-channel discriminator are presented.

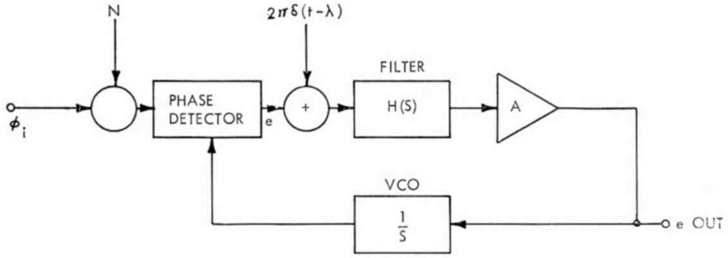

Fig. 1—The linear model for the PLD.

PERFORMANCE OF THE PHASE-LOCKED LOOP AS A DEMODULATOR FOR ANGLE-MODULATED SIGNALS

It will be instructive to review some general properties of the phase-locked demodulator for angle-modulated signals and additive gaussian noise. The model feedback system and its principal elements are represented in Figure 1. The signal is phase inscribed, $e_i = \text{Re}[\exp j(\omega t + \phi_i(t))]$ and is corrupted by additive gaussian noise. The phase of the VCO return signal, ϕ_r, tracks the input phase with a finite phase error $\phi_e = \phi_i - \phi_r$. Over a region, the phase-detector output voltage (e) is proportional to the phase error. The filtered and amplified error voltage is applied to the VCO, which produces a return phase signal, ϕ_r, and the loop is complete.

The VCO has the properties of an integrator with respect to phase, since a step input voltage produces a step frequency change and a phase ramp. The filter is generally a lag network, $H(S) = [(S/S_1) + 1]/[(S/S_2) + 1]$. From the closed-loop response, the output voltage is

$$e_0 = S\phi_r = \frac{AS_2[(S/S_1)+1]S}{S^2+[S_2+(AS_2/S_1)]S+AS_2}\,\phi_i = \frac{AS_2[(S/S_1)+1]S}{S^2+2\beta S_0 S+S_0{}^2}\,\phi_i,$$

where $S_0{}^2 = AS_2$, and $2\beta = \sqrt{S_2/A} + \sqrt{AS_2/S_1}$. This is recognized as the equation for a second-order loop having a damping factor dependent on the gain A, the zero corner S_1, and the pole S_2. Figure 2 shows a log-log plot of the open-loop response.

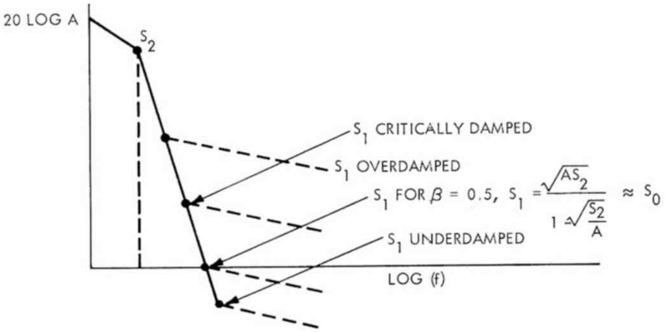

Fig. 2—Open-loop response.

The initial 6 db/octave rolloff is due to the VCO. At the pole the slope changes to 12 db/octave. The lead S_1 restores the slope to 6 db/octave.

A number of criteria can be applied in the choice of the damping factor. A common approach in servo design is to minimize the noise bandwidth for a given natural frequency, which leads to a damping factor of 0.5. For this condition, the zero corner is placed on the frequency axis (0-db gain) and the noise bandwidth is πS_1. A more conservative approach, with respect to stability, is to require critical damping ($\beta = 1$), which places S_1 above 0-db gain.

To account for threshold, the model includes a summing point within the loop where threshold impulses are injected. The impulses are assumed to have a standard strength of 2π and to be Poisson distributed. Thus λ is a random variable characterized by an average rate, and the additive component can be represented as $2\pi\delta(t-\lambda)$, as shown in Figure 1. The threshold properties are determined by this rate as a function of CNR.

The problem is to determine the noise bandwidth and relative allotment of signal and noise phase errors for which the threshold CNR is a minimum. In practice, the threshold is reached when the squared error due to signal and noise reaches a critical value that is proportional to the phase-detector range of lock, i.e., where $\phi_e{}^2 + \phi_n{}^2 = K$. A larger value of K permits a larger signal error ϕ_e and noise error ϕ_n. Hence, the threshold is lowered as K is increased.

The discussion thus far has not been limited to any specific phase-detector or phase-error constraint. The conventional phase detector exhibits a static response that is a sine function of phase error if the input and return waves are sinusoidal. The monotonic range, therefore, is constrained to $\pm\pi/2$. The criteria accepted as nearly optimal for a voice channel are $K = 0.23$ and $\phi_e = 0.3$ radian peak for a sine tone at one-quarter the top base-band frequency. These figures provide sufficient design information for the loop.

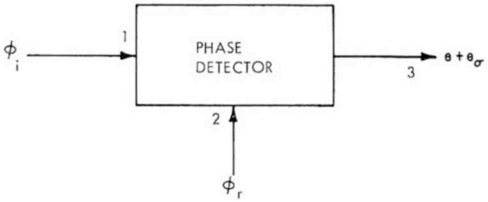

Fig. 3—A representation of the phase detector.

To gain an insight into the threshold-extension potential available through the increase of the range of lock, let it be assumed that the period associated with the phase-detector sine response is doubled and the limits thereby increased to $\pm\pi$. Identical conditions will prevail when both ϕ_e and ϕ_n are doubled; thus, a threshold extension of 6 db would have been realized.

To the extent that a linear model for the phase detector was assumed for the dynamic loop response, the phase-detector range does not influence the closed-loop response. Appendix C develops this idea in greater detail for the ERPLD to be described.

The following discussion is concerned with the static response of a phase detector whose range is extended by phase subtraction, the linearity of the detector, and the threshold characteristics of the loop using this phase detector.

EXTENDED-RANGE PHASE DETECTOR

The phase detector can be represented by a three-port device at which phase and voltage signals appear. As shown in Figure 3, the input and return phase signals are applied to ports 1 and 2, which are

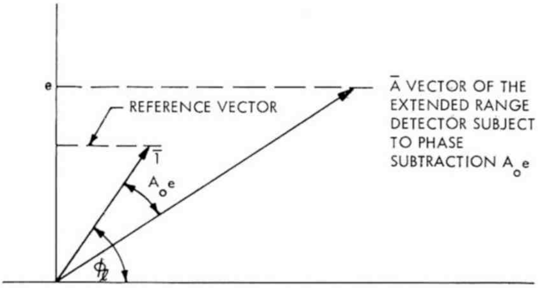

Fig. 4—Vector representation of the phase-detector response.

isolated from each other and from port 3. The output voltage, e, is proportional to $\phi_i - \phi_r = \phi_e$; e_σ represents the impulsive noise due to loss of lock. While e and e_σ may, in general, be interrelated, the probability of loss of lock can be uniquely determined from a static response measurement of e versus $\phi_i - \phi_r$. The onset of the impulse will produce a response that is a function of the phase-detector characteristics. If the system relocks in one cycle, the impulse strength is 2π.

For a conventional phase detector, the static response can be normalized to $e = \sin \phi_e$. The normalized response is shown graphically in Figure 4 as the projection on the vertical axis of a unit vector rotated by ϕ_e.

The application of phase subtraction to extend the range of lock is shown in Figure 5. The VCO return signal is subject to a phase-

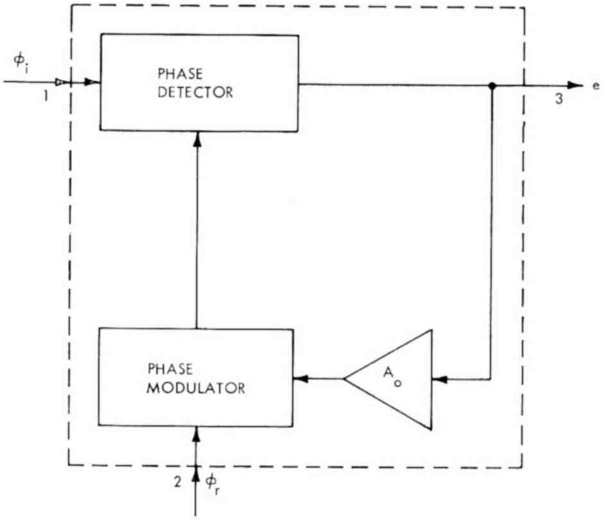

Fig. 5—Block diagram of the extended-range detector by phase subtraction.

retarding action by the phase modulator, so that the phase detector is presented with a phase $\phi_e - A_0 e$. Thus, $e = A \sin(\phi_e - A_0 e)$, where A is the amplitude of the return signal.

Referring to Figure 4, the output voltage is the projection of vector A. The response reaches a maximum when vector A falls on the vertical axis. Since the angle associated with A is retarded from ϕ_e by $A_0 e$, the peak will be reached when ϕ_e exceeds $\pi/2$ by an arbitrary angle, depending on the gain factors A and A_0.

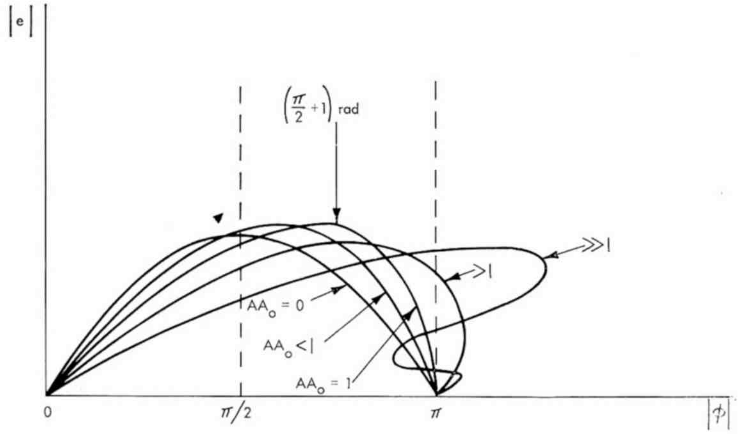

Fig. 6—$|e|$ versus $|\phi|$ characteristics.

STATIC RESPONSE

The solution of the equation $e = A \sin(\phi_e - A_0 e)$ yields the static response and is treated in Appendix A. The following significant facts are established (see Figure 6):

(a) The range extension beyond $\pi/2$ is, strictly speaking, unbounded and given by AA_0 radians.

(b) For $AA_0 \leq 1$, the response is monotonic over the full range, and intersects the ϕ-axis with a slope less than zero.

(c) For $AA_0 = 1$, the response is monotonic and intersects the ϕ-axis at π with infinite slope.

(d) For $AA_0 > 1$, the axis is intersected with positive slope, and an arbitrary range extension is possible. However, a multivalued function results in the path beyond the response peak.

(e) A range of $(\pi/2) + 1$ is realized for the $AA_0 = 1$ case. Figure 6 presents plots of these responses with AA_0 as a parameter. It is noted, of course, that, for $AA_0 = 0$, the system degenerates to the conventional phase detector having a sine response.

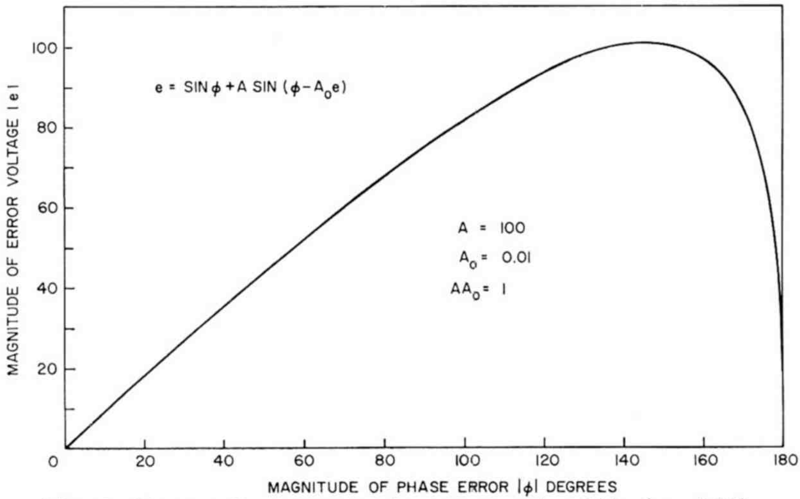

Fig. 7—Error voltage versus phase error ($A = 100$, $A_0 = 0.01$).

To test the sensitivity of the system to variations of gain constants A and A_0 in greater detail, plots were produced of e versus ϕ_e for $A = 100$ and $A_0 = 0.01$ (Figure 7), as well as for $A = 4$ and $A_0 = 0.25$ (Figure 8). The product $AA_0 = 1$ is of interest because it results in a monotonic response beyond the peak. It is noted that the peaks are within about 5 degrees, indicating that neither the gain nor the tolerance requirements are critical.

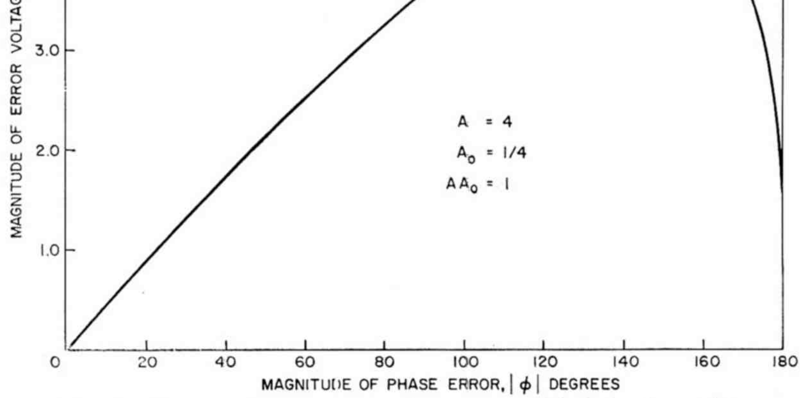

Fig. 8—Error voltage versus phase error ($A = 4$, $A_0 = 1/4$).

PHASE-DETECTOR LINEARITY

It is meaningful to examine linearity in terms of the ratio of the slope m at a given point to the slope of the origin m_0. To obtain a plot of $m/m_0 = \bar{m}$ versus $|\phi|$, it will be convenient to normalize the expression as $e/A = e_n = \sin[\phi_e - (AA_0e)/A]$. In Appendix B the linearity of this equation is considered. Figure 9 shows plots of m versus $|\phi_e|$ for both the conventional and extended-range phase detector. The absolute departure of the response from the straight-line tangent at the origin is obtained by computing the area between the curve and the horizontal at $m = 1$. It is evident that the extended range detector offers appreciably greater linearity over a wide phase angle. Appendix B also derives an rms measure of the linearity of the ERPLD.

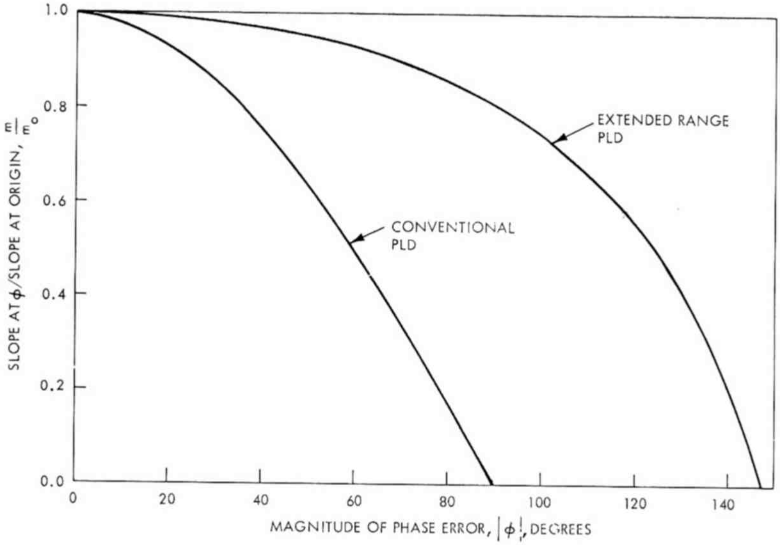

Fig. 9—m/m_0 versus phase error.

ERPLD CLOSED-LOOP RESPONSE

In the following the dynamic response of the ERPLD is treated, taking into account the transfer functions of the individual elements. Figure 10 shows the representation of the linear model of the loop. Linearity implies that the phase comparator and phase modulator can be represented by linear summers, which is valid for small signals. The blocks are identified as follows:

(a) The phase comparator is represented as a summer with a sensitivity of δ volts per radian and output voltage, e.

(b) The base-band filter, whose transfer function is $H(S)$, has a gain constant K at $S = 0$.

(c) The voltage-controlled oscillator (VCO) is represented as an integrator. It has sensitivity of μ[radians/s]/V.

(d) The phase modulator (PM) is represented as a summer.

(e) The amplifier driving the phase modulator is assumed to have a frequency response $F(S)$ with a constant gain, G.

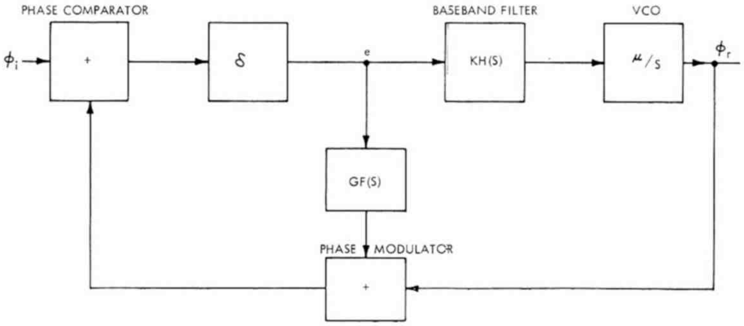

Fig. 10—The linear model of the ERPLD.

As shown in Appendix C, the closed-loop transfer function, $T_1(S)$, for the ERPLD is given by

$$T_1(S) = \frac{\phi_r(S)}{\phi_i(S)} = \frac{\delta K \mu H(S)}{S[1 + \delta G F(S)] + \delta K \mu H(S)}.$$

For $G = 0$, the closed-loop response of the PLD is

$$T_2(S) = \frac{\delta K \mu H(S)}{S + \delta K \mu H(S)}.$$

The practical problem that arises is to choose $H(S)$ such that, given $F(S)$ (whether intentional or incidental), a prescribed closed-loop response is realized. The prescribed closed-loop response typically may be a second-order system with a damping factor of 0.5, as for a PLD.

Whether or not the transfer function $H(S)$ can be realized depends on $F(S)$. It is of interest, therefore, to examine the condition of frequency independence, $F(S) = 1$. As would be expected from the previous discussion, the closed-loop response of the PLD should be unchanged by the phase-detector range extension, except for the change of phase-detector sensitivity. This is evident from the expression

$$T_1(S) = \frac{[(\delta K\mu)/(1+\delta G)]H(S)}{S + [(\delta K\mu)/(1+\delta G)]H(S)}.$$

In the following discussion of experimental results, the close correspondence of the closed-loop response for the PLD and ERPLD for equal loop gain will be evident. Since the closed-loop bandwidth of the ERPLD is unchanged, the threshold extension properties are directly attributed to the larger tolerance of phase error.

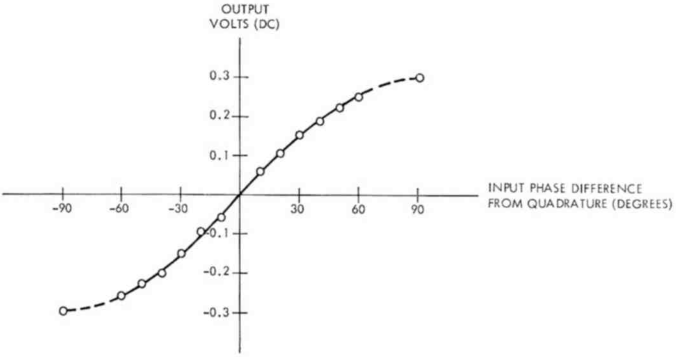

Fig. 11—Static response of phase detector.

EXPERIMENTAL VOICE CHANNEL ERPLD

An ERPLD was implemented for a single-channel FM receiver. The specific parameters chosen were:

Base-band voice channel: 300-3300 Hz
Center frequency: 11.5 MHz
Deviation: ±10 kHz peak
I-F bandwidth: 35 kHz
Base-band bandwidth: 3.5 kHz

These parameters are typical for tactical FM transceivers and, in this regard, the performance of the ERPLD was related to that of the AN/PRC-25 limiter–discriminator.

The phase detector in the ERPLD had a sensitivity of 0.3V/[rad/s]. The response is shown in Figure 11. The VCO was a modification of the VCO used in the AN/PRC-25 set. The oscillator was varactor controlled, but the crystal was removed. The sensitivity was 255 [rad/s]/V. The frequency-versus-voltage plot is shown in Figure 12. The phase modulator employs varactors imbedded in a second-order equalizer network that provides a linear phase-versus-voltage relationship. This quality is important with regard to optimization of circuit performance. The sensitivity of the modulator is $\pi/7$ V/rad, and its response is shown in Figure 13. Operational amplifiers were used for the VCO drive and in the phase modulator section.

The noise bandwidth is related to the modulation parameters by

$$B_n = C\sqrt{f_b \Delta F},$$

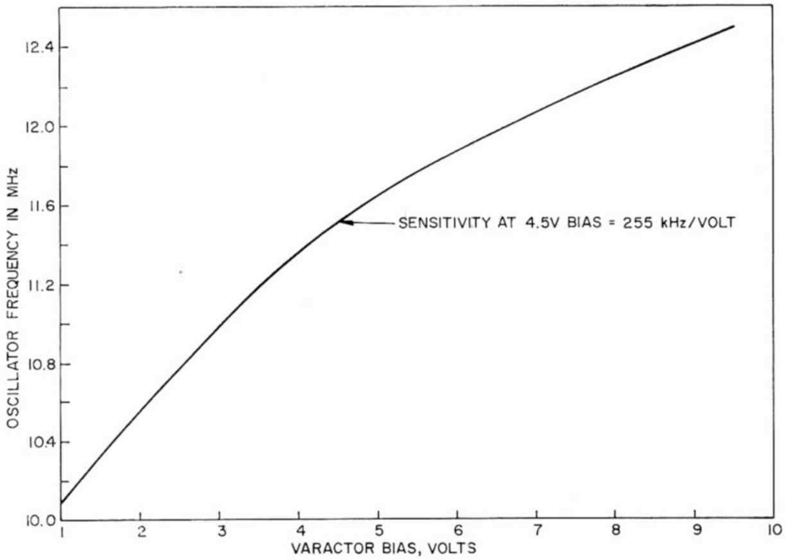

Fig. 12—VCO sensitivity.

where $B_n =$ noise bandwidth in Hz, f_b is the top base-band frequency in Hz, ΔF is the rms frequency deviation in Hz, and C is a constant that depends upon the nature of the base band (i.e., tone, voice, etc.). In particular, $C = 4.46$ for voice. The rms deviation can be determined for a voice signal with a ±10-kHz peak deviation by assuming a peak-to-rms ratio for voice to be 10 db. The rms deviation is then $\pm\sqrt{10}$ kHz.

Since the upper end of the base band is about 3.3 kHz,

$$\begin{aligned} B_n &= 4.46\ [\sqrt{10}\,(3.3)\,]^{1/2} \\ &= 14.4 \text{ kHz.} \end{aligned}$$

Given the noise bandwidth, the maximum gain is developed across the base band in the loop with a damping factor of 0.5. The noise bandwidth is related to the corner frequencies S_1 and S_2 and the loop gain, K, by

$$B_n = \sqrt{KS_2}/2 = S_1/2 \text{ Hz},$$

where S_1 and S_2 are in rad/s.

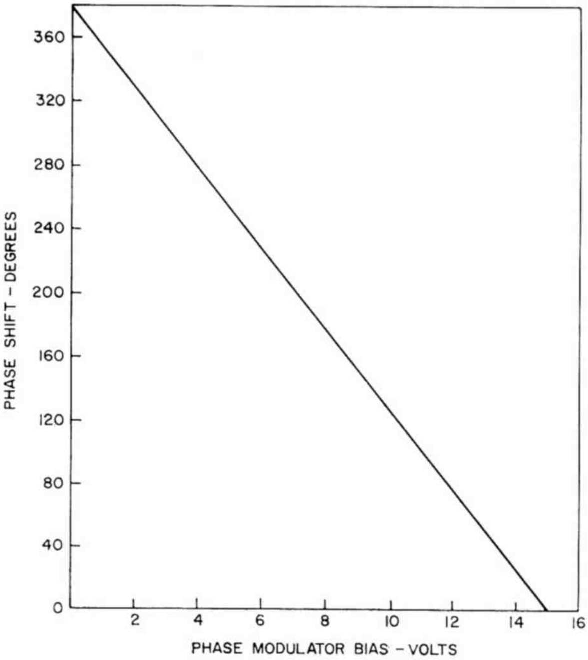

Fig. 13—Phase modulator modulation characteristic.

S_1 is determined as $29.4K$ rad/s. Given the loop gain, S_2 is obtained as the intersection of the 6 db/octave and the 12 db/octave asymptotes pivoted at the 1-rad/s and S_1 points, respectively. For d-c stability and low-frequency gain, it is desirable to realize a high system gain that results in a low S_2 corner frequency. In the experimental system, the sensitivities of the phase detector and VCO were 0.3 V/rad and 255 kHz/V, respectively. The combined loop gain was 4.7×10^5 s^{-1}. S_2 was 1,880 rad/s, which was considered low enough for voice application.

The gain in the phase-modulator control was adjusted for the requirement that the product of phase-detector and phase-modulator sensitivities be unity, as established from the linear-model analysis,

ERPLD FREQUENCY RESPONSE

The frequency response of the ERPLD was measured by frequency modulating a carrier with a variable-frequency tone and observing the demodulated output level as a function of frequency. The modulation index was lowered substantially from the design value for these tests to ensure that the loop would track frequencies much higher than the intended base band. The result of this test is shown in Figure 14.

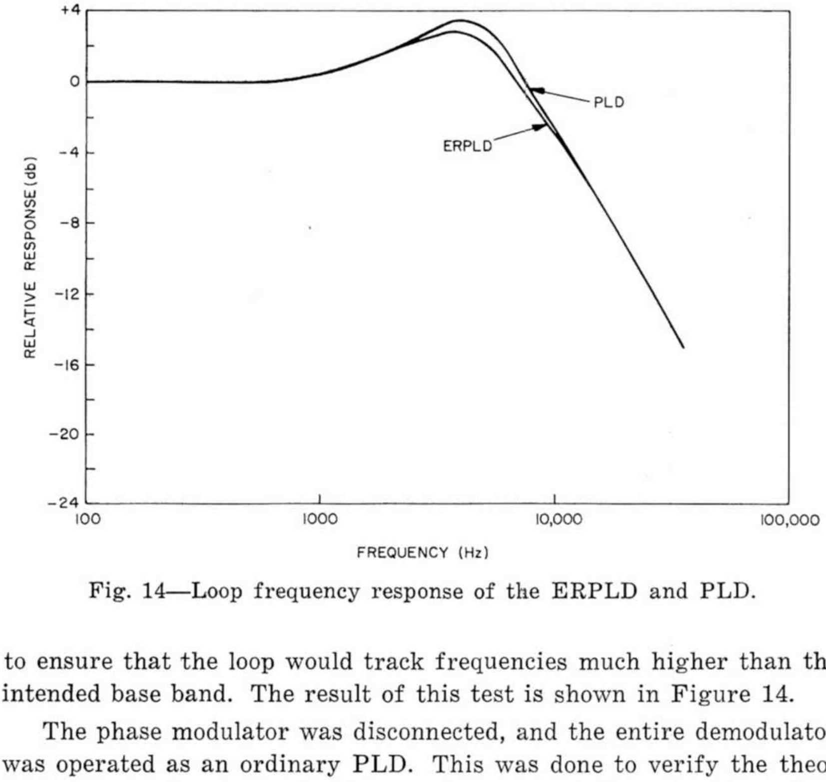

Fig. 14—Loop frequency response of the ERPLD and PLD.

The phase modulator was disconnected, and the entire demodulator was operated as an ordinary PLD. This was done to verify the theoretical prediction that, for linear phase modulation, the closed-loop response for both ERPLD and PLD would be the same. The PLD response is also given in Figure 14.

ERPLD THRESHOLD PERFORMANCE

The ERPLD was tested with additive gaussian noise interference. The test set-up is shown in Figure 15. The carrier was modulated with a 1-kHz tone and ±10 kHz peak deviation. Both carrier and noise were filtered by a 34-kHz crystal filter from an AN/PRC-25 set. The power response for this filter is shown in Figure 16. The demodulated signal level was monitored in a 6-Hz wide filter. The output noise level was

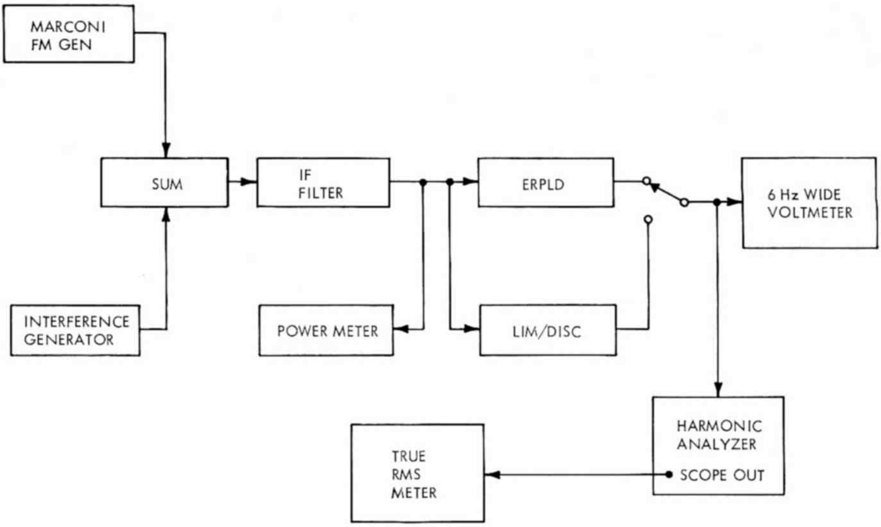

Fig. 15—Test setup for output SNR measurements.

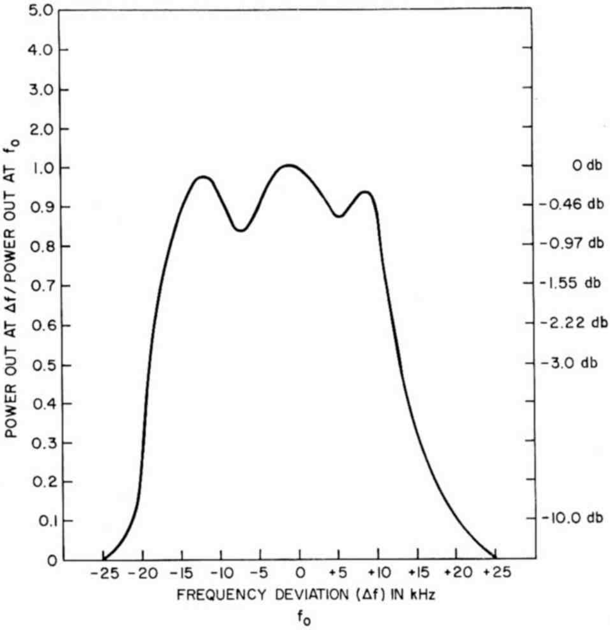

Fig. 16—Power response for the nominal 11.5 MHz predetection filter.

measured in a 3.3-kHz low-pass filter with the signal nulled by a notch filter. The input CNR versus output SNR relationship is shown in Figure 17.

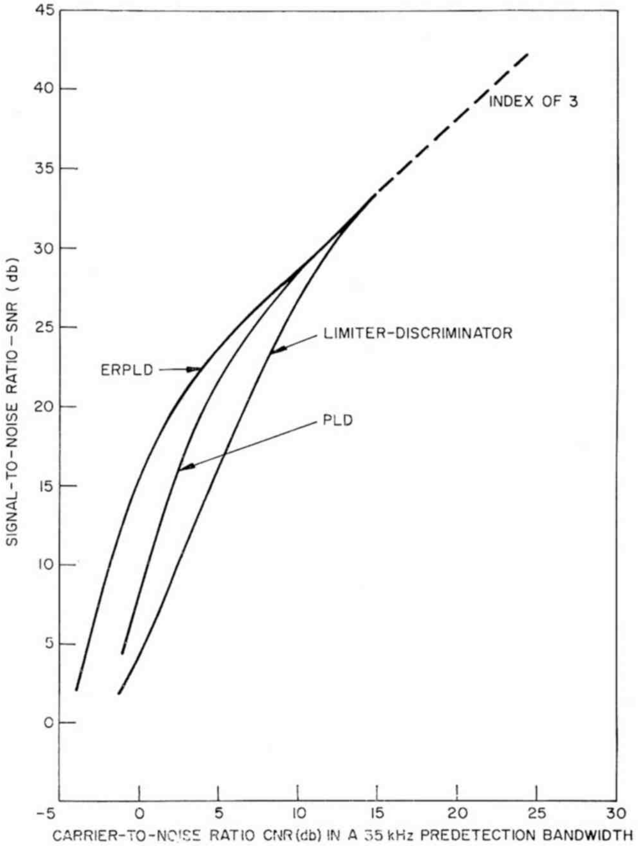

Fig. 17—Measured SNR versus CNR (additive Gaussian noise) for 4-kHz voice channel base-band and an FM carrier, modulated by a 1-kHz tone with a 10-kHz peak deviation.

The AN/PRC-25 limiter–discriminator module and the PLD configuration were also tested. Both are shown in Figure 17.

Defining the threshold point by the CNR value for which the NIF is 1 db down from the high-level value, the threshold CNR for the discriminator is +10 db, while for the ERPLD it is +2 db, an 8-db advantage. It is interesting to note that the ERPLD curve below threshold is relatively well-behaved and affords substantial improvement over the discriminator.

Figure 18 shows photographs of a 1-kHz tone demodulated by the

ERPLD and the conventional limiter–discriminator. Three levels of CNR were chosen. The 12-db level is above threshold for both devices, and the photographs show identical performance. The 6-db level is above threshold of the ERPLD but below threshold of the limiter–discriminator. The 2-db level is the threshold point of the ERPLD.

In addition to the impulsive noise, a certain amount of signal suppression is evident in the limiter–discriminator. This is not present in the ERPLD.

CONCLUSIONS

When the range of lock of the phase detector is extended, a larger margin of phase error due to noise can be allowed for a given loss-of-lock probability. This results in a lower threshold CNR in demodulation of angle-modulated signals.

The application of feedback to retard the phase-return signal transmitted through a phase modulator enables the extension of range of lock by an arbitrary amount. The extension of one radian from $\pm\pi/2$ to $\pm(\pi+2)/2$ is possible with a monotonic static response on both sides of the peak. Such an ERPLD was implemented for a voice channel, and a threshold extension of 8 db relative to the limiter–discriminator was achieved.

ACKNOWLEDGMENTS

The contribution of R. Sommer in a number of analytical and computational tasks is acknowledged. J. T. Frankle provided valuable suggestions in linearizing the phase modulator and assistance in the formal design of the PLD. The support and encouragement of S. Cohen and his staff of USECOM, under whose sponsorship (Contract number DA 28-043-AMC-00167(E)) this work was performed, is gratefully acknowledged.

APPENDIX A—EXTENDED-RANGE PHASE-DETECTOR CHARACTERISTICS

Consider the extended-range phase detector with dynamic characteristic

$$e = A\sin(\phi - A_0 e), \tag{1}$$

as described in the text. Recall that ϕ is the applied phase difference, and e is the output voltage. It is expedient to normalize Equation (1) by allowing $e_n = e/A$, such that

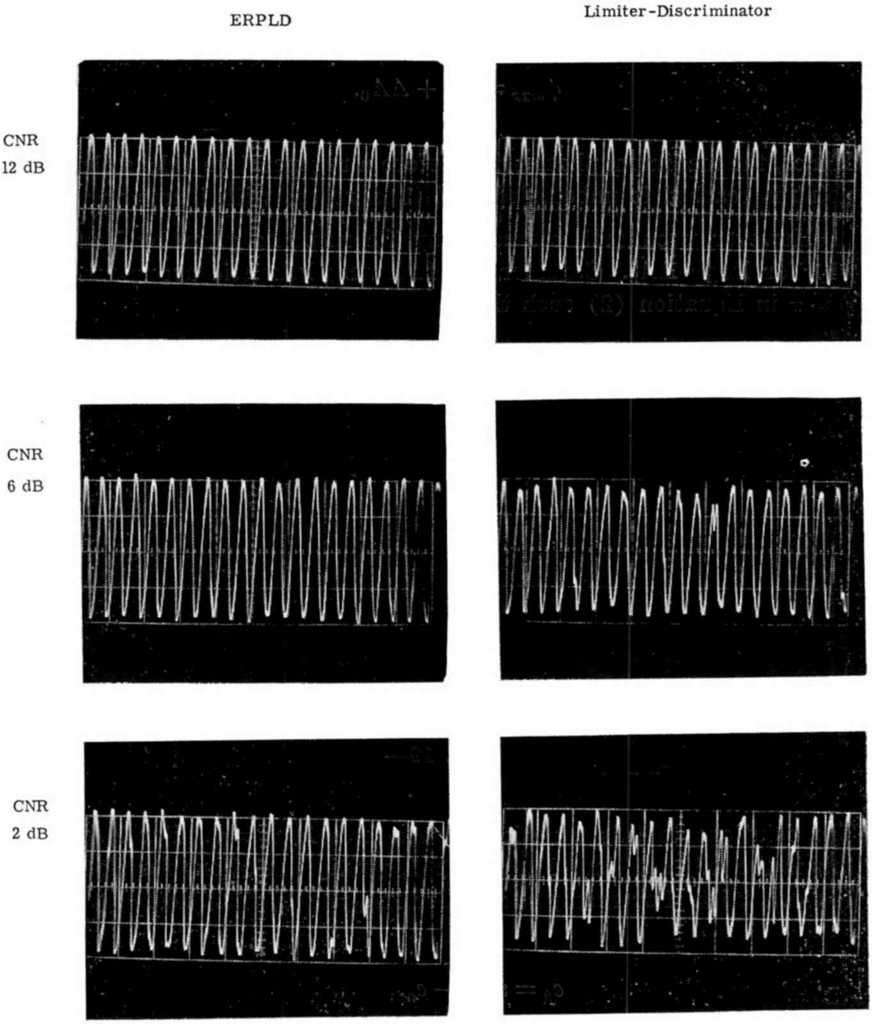

Fig. 18—Photographs of the demodulated 1-kHz tone.

$$e_n = \sin(\phi - AA_0 e_n). \tag{2}$$

Evidently, the normalized output voltage is bounded by ±1, since $|\sin x| \leq 1$.

When the upper bound $e_n = +1$ is reached, the phase error, ϕ_{max}, which causes this condition, is (considering principal values only)

$$\phi_{max} - AA_0 = \frac{\pi}{2} \tag{3}$$

or

$$\phi_{max} = \frac{\pi}{2} + AA_0. \tag{4}$$

Hence, the maximum phase error before a regenerative (slope change) point is reached is unbounded, and it increases with increasing AA_0.

However, peculiarities accompany the response given by Equation (1) for large AA_0. Consider the following heuristic argument. Let $\phi = \pi$ in Equation (2) such that

$$e_n = \sin(\pi - AA_0 e_n) = \sin AA_0 e_n. \tag{5}$$

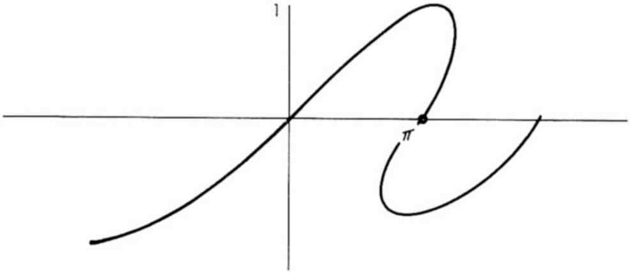

Fig. 19—

The solutions to this equation always include $e_n = 0$. For $AA_0 < 1$, this is the only solution. For $AA_0 > 1$, multiple solutions for Equation (5) can exist. For example, consider $AA_0 = \pi/2$, such that

$$e_n = \sin \frac{\pi}{2} e_n. \tag{6}$$

Obviously, $e_n = 0$ and $e_n = 1$ both satisfy Equation (6), and the plot of Equation (2) for $AA_0 = \pi/2$ is shown in Figure 19. In fact, as AA_0 increases, so do the number of solutions to Equation (5). For arbitrarily large AA_0, the resultant plot from Equation (2) can be shown as in Figure 20. To obtain information regarding the slope of the curve given by Equation (2) at the point $\phi = \pi$, consider the implicit differentiation of Equation (2) and evaluation of this derivative at $e_n = 0$, $\phi = \pi$. From Equation (2),

$$de_n = \cos(\phi - AA_0 e_n)[d\phi - AA_0 de_n]. \tag{7}$$

At $\phi = \pi$, $e_n = 0$,

$$de_n = -1[d\phi - AA_0 de_n], \tag{8}$$

or

$$\frac{de_n}{d\phi} = -\frac{1}{1 - AA_0}. \tag{9}$$

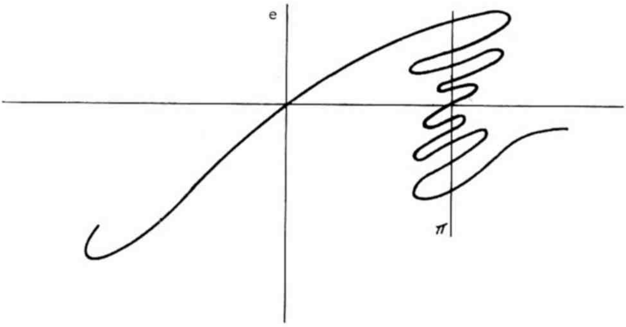

Fig. 20—

Hence, for $AA_0 < 1$, the slope at $\phi = \pi$ is <0; for $AA_0 > 1$, the slope at $\phi = \pi$ is >0; and for $AA_0 = 1$, the slope is infinite.

Clearly then, from Equations (4) and (9), the condition $AA_0 = 1$ provides the largest range extension (one radian), while maintaining the regenerative region free of ambiguous loops and slope changes.

APPENDIX B—LINEARITY OF e VERSUS ϕ CHARACTERISTIC OF ERPLD

Consider the normalized phase-detector characteristic $e_n = \sin(\phi - e_n)$ when $AA_0 = 1$. Since $|e_n| \leq 1$, it follows that

$$\cos(\phi - e_n) = (1 - e_n^2)^{1/2}, \tag{10}$$

and

$$de_n = \cos(\phi - e_n)\, d\phi - \cos(\phi - e_n)\, de_n. \tag{11}$$

Thus,

$$\frac{de_n}{d\phi} = \frac{\cos(\phi - e_n)}{1 + \cos(\phi - e_n)} = \frac{(1 - e_n^2)^{1/2}}{1 + (1 - e_n^2)^{1/2}}. \tag{12}$$

Define M as the slope of e_n versus ϕ at some angle ϕ and M_0 as the slope of e_n versus ϕ at $\phi = 0$. Then a measure of linearity for the e_n versus ϕ characteristic for the ERPLD is

$$\bar{m} = \frac{M}{M_0} = \frac{2(1 - e_n{}^2)^{1/2}}{1 + (1 - e_n{}^2)^{1/2}}, \tag{13}$$

where $e_n = \sin(\phi - e_n)$. For a conventional PLD,

$$\bar{m} = \frac{M}{M_0} = \cos\phi. \tag{14}$$

The results given by Equations (13) and (14) are shown in Figure 9. An rms measure of linearity can be obtained by considering the case where $AA_0 = 1$ and $A \rightarrow \infty$ and confining attention to the range $|\phi| \leq 33$ degrees. Choose a linear function with a slope of m_a and compute the mean square departure from linearity,

$$\frac{1}{\phi_m} \int_0^{\phi_m} (m_a - m)^2 d\phi,$$

where m is the slope of the ERPLD characteristic at a phase error ϕ. The result of such a calculation (by numerical means) for $\phi_m = 33$ degrees is shown in Figure 21. The linear function that exhibits the least-mean-square error in slope is characterized by $m_a \doteq 0.9948$, for which the minimum rms departure from linearity is about 0.6015%.

With a conventional PLD, $m = \cos\phi$, and it can easily be shown that the mean square departure from linearity is

$$\frac{1}{\phi_m}\left[m_a{}^2\phi_m - 2m_a \sin\phi_m + \frac{\phi_m}{2} + \frac{1}{4}\sin 2\phi_m \right],$$

which minimizes when $m_a = (1 + \cos\phi_m)/2$. With $\phi_m = 33$ degrees, $m_a \doteq 0.919$ provides a minimum rms departure from linearity of about 4.31%.

APPENDIX C—THE LINEAR MODEL ANALYSIS OF THE ERPLD

Consideration of the linearized model for the ERPLD, as shown in Figure 10, leads to the closed-loop transfer response for the system.

Moreover, some interesting properties regarding the phase-detector output voltage as a function of phase difference between the input carrier and the tracking VCO can be obtained.

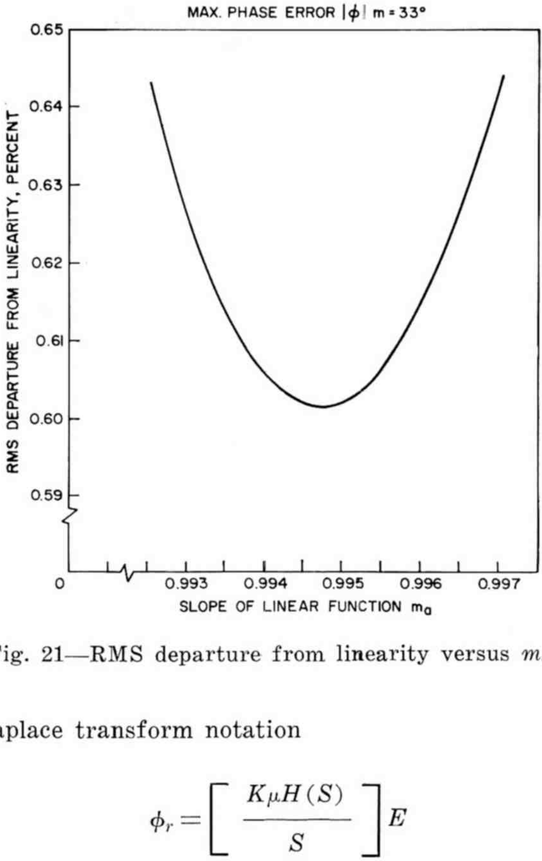

Fig. 21—RMS departure from linearity versus m_a.

Using Laplace transform notation

$$\phi_r = \left[\frac{K\mu H(S)}{S} \right] E \tag{15}$$

$$E = \delta [\phi_i - \phi_r - EGF(S)]. \tag{16}$$

From Equation (15),

$$E = \frac{\phi_r}{K\mu H(S)/S}\,; \tag{17}$$

And from Equation (16),

$$E = \frac{\delta(\phi_i - \phi_r)}{1 + \delta GF(S)}. \tag{18}$$

Dividing Equation (17) by Equation (18) gives

$$1 = \frac{\phi_r/[K\mu H(S)/S]}{[\delta(\phi_i - \phi_r)]/[1 + \delta GF(S)]}, \tag{19}$$

or

$$\frac{\phi_i - \phi_r}{\phi_r} = \frac{1 + \delta GF(S)}{\delta K\mu H(S)/S} = \frac{\phi_i}{\phi_r} - 1. \tag{20}$$

Then

$$\frac{\phi_i}{\phi_r} = \frac{1 + \delta GF(S) + \delta K\mu H(S)/S}{\delta K\mu H(S)/S}. \tag{21}$$

The required phase transfer function ϕ_r/ϕ_i is obtained by inverting Equation (21),

$$\frac{\phi_r}{\phi_i} = \frac{\delta K\mu H(S)/S}{[1 + \delta GF(S)] + (\delta K\mu \mathrm{H}(S)/S)} = T_1(S). \tag{22}$$

Equation (22) can be written more recognizably as

$$T_1(S) = \frac{\delta K\mu H(S)}{[1 + \delta GF(S)]\,S + \delta K\mu H(S)}, \tag{23}$$

which is the closed-loop transfer function of the ERPLD.

The closed-loop response for the PLD without phase modulator is simply obtained by letting $G = 0$ in Equation (23),

$$T_2(S) = \frac{\delta K\mu H(S)}{S + \delta K\mu H(S)}. \tag{24}$$

As explained earlier, from a theoretical point of view and for comparative purposes it is desirable to maintain the same closed-loop response for both the PLD and ERPLD. In Equations (23) and (24), it is tacitly assumed that the loop filter $H(S)$ is the same for both loops. If this is the case, then $T_1(S)$ and $T_2(S)$ can never be equivalent except for $F(S) = \text{constant}$.

For nonconstant $F(S)$, $T_1(S)$ and $T_2(S)$ can sometimes be made equivalent by using a different primary loop filter $H^1(S)$ for the

ERPLD than for the PLD case. The "sometimes" qualification is necessary since, given an arbitrary realizable $F(S)$, the resulting $H^1(S)$ to make equivalent transfer functions is $H^1(S) = H(S)\ [1 + \delta GF(S)]$, which may not be physically realizable.

Furthermore, the development of loop-stabilizing filters in feedback loops is so well-established for PLD that it is convenient to leave the loop filter the same for the ERPLD. Thus, $F(S) = 1$, and Equation (23) becomes

$$T_1(S) = \frac{\dfrac{\delta K\mu}{1+\delta G} H(S)}{S + \dfrac{\delta K\mu}{1+\delta G} H(S)} . \tag{25}$$

The similarity between Equations (24) and (25) (except for a gain constant) is immediately evident.

BIBLIOGRAPHY

1. A. J. Viterbi, "Phase-Locked Loop Dynamics in the Presence of Noise by Fokker–Planck Techniques," *Proc. IEEE,* Vol. 51, No. 12, Dec. 1963.

2. R. M. Jaffee, J. G. Rechtin, "Design and Performance of Phase-Locked Circuits Capable of Near-Optimum Performance Over a Wider Range of Signal and Noise Levels," *IRE Trans. on Information Theory,* Vol. IT-1, No. 1, March 1955.

3. J. Develet, "A Threshold Criterion for Phase-Locked Demodulation," *Proc. IEEE,* Vol. 51, No. 2, Feb. 1963.

THE ACOUSTOELECTRIC EFFECTS AND THE ENERGY LOSSES BY HOT ELECTRONS —PART II

BY

ALBERT ROSE

RCA Laboratories
Princeton, N. J.

Editor's Note: This is the second part of a several part paper. Part I appeared in the March 1966 issue of *RCA Review* (Vol. XXVII, No. 1, p. 98).

Summary—*The rates of energy loss by hot electrons to phonons and to electronic excitations are derived from an elementary model. All of the energy-loss expressions have essentially the same form. The various channels for loss of energy are characterized by a coupling constant which, in the case of phonons, is shown to be the ratio of electrical to total energy for the corresponding macroscopic sound waves. It is the same coupling constant which, in Part I, was shown to characterize the various acoustoelectric effects. Quantum effects are introduced as constraints on the classical model. Finally, the rates of energy loss are related to the acoustoelectric effects by a heuristic argument.*

1. INTRODUCTION

WHEN an electric field is applied to a solid, the free carriers are heated relative to the lattice. The degree to which the carriers are heated depends on the rate at which they can lose energy to the lattice. Since the rate of energy loss is rather insensitive to the lattice temperature, we will assume a zero-temperature lattice.

The gamut of energy-loss mechanisms is shown in Table I. At the low end of the scale, electrons whose energies lie in the approximate range 1 to 25 millivolts lose energy to acoustic phonons. The coupling to the acoustic phonons may be via a deformation potential or a piezoelectric field. At about 25 millivolts the electrons begin to lose energy

Table I

Form of Radiated Energy	Approximate Threshold Excitation Energy Electron Volts	Analyzed By	Year
Acoustic Phonons	10^{-3}		
Deformation-Potential		Seitz[1]	1949
Piezoelectric		Tsu[2]	1964
Intervalley Scattering		Herring[3]	1955
Optical Phonons	10^{-2}		
Polar		Fröhlich[4]	1939
Nonpolar		Conwell[5]	1959
Impact Ionization	E_{gap}	Motizuki and Sparks[6]	1964
Plasmons	10	Bohn and Pines[7]	1953
Excitation of X-Ray Levels	10^2	Bohr[8] Bethe[9]	1913 1929
Cerenkov Radiation	10^4	Frank and Tamm[10]	1937

---

[1] F. Seitz, "On the Theory of Electron Multiplication in Crystals," *Phys. Rev.*, Vol. 76, p. 1376, Nov. 1, 1949.

[2] R. Tsu, "Phonon Radiation by Uniformly Moving Charged Particles in Piezoelectric Solids," *Jour. Appl. Phys.*, Vol. 35, p. 125, Jan. 1964. See also H. J. G. Meijer and D. Polder, "Notes on Polar Scattering of Conduction Electrons in Regular Crystals," *Physica*, Vol. 19, p. 255, 1953.

[3] C. Herring, "Transport Properties of a Many-Valley Semiconductor," *Bell Syst. Tech. Jour.*, Vol. 34, p. 237, March 1955.

[4] H. Fröhlich, "On the Theory of Dielectric Breakdown in Solids," *Proc. Roy. Soc.* (London), Vol. A188, p. 521, 25 Feb. 1947; H. Fröhlich, "Theory of Electrical Breakdown in Ionic Crystals," *Proc. Roy. Soc.*, Vol. A160, p. 230, 18 May 1937.

[5] E. M. Conwell, "Relative Energy Loss to Optical and Acoustic Modes of Electrons in Avalanche Breakdown in Ge," *Phys. Rev.*, Vol. 135, p. A1138, 17 Aug. 1964.

[6] K. Motizuki and M. Sparks, "Range of Excited Electrons and Holes in Metals and Semiconductors," *Jour. Phys. Soc. Japan*, Vol. 19, p. 486, April 1954.

[7] D. Pines and D. Bohm, "A Collective Description of Electron Interactions; II. Collective vs. Individual Particle Aspects of the Interactions," *Phys. Rev.*, Vol. 85, p. 338, 15 Jan. 1952; and "A Collective Description of Electron Interactions: III. Coulomb Interactions in a Degenerate Electron Gas," *Phys. Rev.*, Vol. 92, p. 609, Nov. 1, 1953.

[8] N. Bohr, "Decrease of Speed of Electrified Particles in Passing Through Matter," *Phil. Mag.*, Vol. 25, p. 10, Jan. 1913 and Vol. 30, p. 581, Oct. 1915.

[9] H. Bethe, *Ann. Phys.*, Vol. 16, p. 285, 1933; *Handbuch der Physik* (Geiger and Scheel, Eds.), Vol. 24, Part I, Springer, Berlin, 1933; (see also Reference (11) for critical historical review).

[10] I. Frank and I. Tamm, "Coherent Visible Radiation from Fast Electrons Passing Through Matter," *Comptes Rendus (Doklady) de l'Acad. des Sci.*, USSR, Vol. 14, p. 109, 1937.

[11] J. D. Jackson, *Classical Electrodynamics*, John Wiley and Sons, New York, 1963.

to optical phonons, both polar and nonpolar. For energies of the order of volts, they can lose energy by impact ionization across the forbidden gap. In the range of about ten to twenty volts they begin to excite plasmon oscillations. At the level of hundreds of volts they lose energy to the deeper-lying atomic levels. Finally, at speeds approaching the velocity of light, the electrons emit Cerenkov radiation. All of the above energies represent threshold values. High-velocity electrons lose energy to all of the above mechanisms simultaneously.

The rates of energy loss to each of the channels listed have been computed and have appeared in the literature. Some of the names and dates associated with these publications are listed in Table I. It is interesting to note that the dates are more or less uniformly distributed over the last fifty years. The methods of analysis are almost as varied as the number of contributors. Moreover, most of the analyses, particularly those for energy loss to phonons, are carried out in momentum space. The following discussion is an attempt to re-state the arguments in "real space" and in terms of an elementary model. The results have only an order-of-magnitude validity, consistent with the use of the uncertainty principle.

An outline of the argument is presented in the next four sections. This is followed by a more detailed consideration of each of the modes of energy loss. The central concept is that of an electron polarizing the surrounding medium to form an energy well. The moving electron loses energy in the form of a wake, or trail, of energy wells.

2. DIMENSIONAL ARGUMENT

Figure 1 gives a dimensional argument for the rate of loss of energy by a moving particle to a system with which it interacts. In Figure 1 a particle moves with velocity v past a series of elements of dimension d. The particle repels each element with a force such that, for a stationary particle, an energy E_w is stored in the "compressed spring" of the element. The frequency of vibration of each element is denoted by ω.

By inspection we can write the maximum rate of loss of energy by the particle:

$$\left.\frac{dE}{dt}\right]_{\max} \approx E_w \omega. \tag{1}$$

At the assumed velocity ωd, the particle spends a time ω^{-1} opposite each element and deflects the element almost as far as it would if the particle were stationary. While the element is in the deflected state the particle moves on to the next element leaving behind an energy of almost E_w per element. Since, by assumption, the particle traverses ω elements per second, the rate of energy loss is that given by Equation (1).

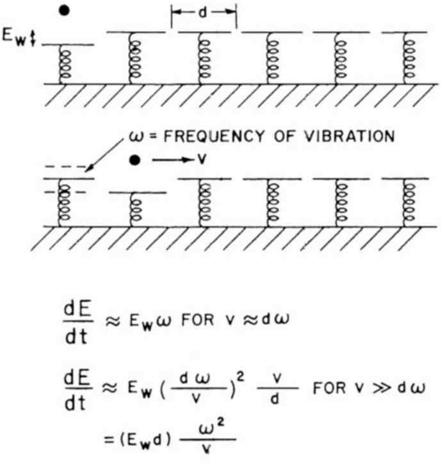

Fig. 1—Model for computing rate of energy loss by a moving particle.

A quick confirmation of Equation (1) is obtained by expressing the maximum rate of loss of energy to polar optical phonons as the product of the polaron energy $\alpha\hbar\omega$ and the optical-phonon frequency ω:

$$\left.\frac{dE}{dt}\right]_{\max} = (\alpha\,\hbar\,\omega)\;\omega$$

$$= \frac{e^2}{\bar{\epsilon}}\left(\frac{m}{\hbar^3\omega}\right)^{1/2}\hbar\omega^2 = \frac{e^2\omega^2}{\bar{\epsilon}v} \qquad \text{for } \tfrac{1}{2}\,mv^2 \approx \hbar\omega, \qquad (2)$$

where $\bar{\epsilon}^{-1} \equiv \epsilon_\infty{}^{-1} - \epsilon_0{}^{-1}$. Equation (2) matches the result obtained by Fröhlich[4] and by Callen[12] using perturbation theory. In this argument we have, of course, borrowed the concept and magnitude of a polaron energy well from the results of perturbation theory. We will show later a semiclassical method of computing E_w.

Meantime, returning to Figure 1, we observe, again almost by

---

[12] H. B. Callen, "Electric Breakdown in Ionic Crystals," *Phys. Rev.*, Vol. 76, p. 1394, Nov. 1, 1949.

inspection, that the rate of energy loss for $v > \omega d$ is

$$\frac{dE}{dt} = E_w \left(\frac{\omega d}{v} \right)^2 \frac{v}{d} = E_w d \frac{\omega^2}{v}. \tag{3}$$

The factor $(\omega d)/v$ is equal to $\omega\tau$, where τ is the transit time of the particle past one of the elements of the array. Equation (3) reduces to Equation (1) for $\omega\tau = 1$. For $v > \omega d$, $\omega\tau < 1$ so that the particle acts on each element with an impulsive force. The momentum imparted is proportional to τ. Hence, the energy imparted is proportional to τ^2. The energy imparted per element is therefore less than E_w by the factor $(\omega\tau)^2$ where $\omega\tau < 1$. The last factor, v/d, is simply the number of elements traversed per second.

Equation (3) is the essence of the "real-space" argument for energy losses by fast electrons. In order to apply Equation (3) to electrons, we need to determine in each case the value of E_w, the energy well that a stationary electron digs in the surrounding medium or, more definitely, in the mode of vibration of the medium through which the energy loss is being computed.

For those cases where the electron couples to and does work on the medium via its coulomb field, we can write

$$E_w = \beta \frac{e^2}{Kd}, \tag{4}$$

where β is, by definition, the fraction of the available coulomb energy that is used to form an energy well and K is the real part of the dielectric constant for frequencies higher than that of the emitted radiation. For example, if the electron is emitting energy to polar optical phonons, K is equal to ϵ_∞, the high-frequency, or electronic, part of the dielectric constant. In brief, the coulomb energy available for doing work on the ionic part of the lattice is reduced from its vacuum value by the electronic polarization factor ϵ_∞.

Combination of Equations (3) and (4) yields

$$\frac{dE}{dt} \approx \beta \frac{e^2\omega^2}{Kv}. \tag{5}$$

This is the form in which the various rates of energy loss, taken from the published literature, have been recast in Table II. In the case of coupling by deformation potential, a coulomb energy of $e^2/(Kd)$, d

Table II—Time Rates of Energy Loss (dE/dt) by Electrons of Velocity v.

Phenomenon	dE/dt	Source
Polar Optical Phonons	$\left[\frac{\epsilon_o - \epsilon_\infty}{\epsilon_o}\right]\frac{e^2\omega^2}{\epsilon_\infty v}\ln\left(\frac{2m\,v^2}{\hbar\omega}\right)$ Note: $\frac{1}{2}mv^2 > \hbar\omega$	Fröhlich[4] Callen[12]
Piezoelectric Phonons	$\frac{\pi}{4}\left[\frac{\epsilon_p{}^2}{KC}\right]\frac{e^2\omega^2}{Kv}$ Note: $2mv = \hbar\omega/v_s$	Tsu[2]
Acoustic Phonons	$\frac{1}{4}\left[\frac{B^2\omega^2K}{4\pi e^2\rho v_s{}^4}\right]\frac{e^2\omega^2}{Kv}$ Note: $2mv = \hbar\omega/v_s$	Seitz[1] Conwell[5]
Nonpolar Optical Phonons	$\frac{1}{2}\left[\frac{\pi KD^2}{\rho e^2\omega^2\lambda^2}\right]\frac{e^2\omega^2}{Kv}$ Note: $\frac{1}{2}mv^2 > \hbar\omega$ and $\frac{\lambda}{2\pi} = \frac{\hbar}{2mv}$	Conwell[5]
X-Ray Levels	$\left[\frac{\omega_p{}^2}{\omega_e{}^2}\right]\frac{e^2\omega_e{}^2}{v}\ln\left(\frac{2mv^2}{\hbar\omega_e}\right)$ Note: $\omega_p{}^2 = \frac{4\pi ne^2}{m} \ll \omega_e{}^2$ $\hbar\omega_e$ = Excitation energy of x-ray levels $\frac{1}{2}mv^2 > \hbar\omega_e$	Bohr[8] Bethe[9]
Plasma	$\left[1\right]\frac{e^2\omega^2}{v}\ln\left(\frac{2mv^2}{\hbar\omega}\right)$ Note: ω = plasma frequency and $\frac{1}{2}mv^2 > \hbar\omega$	Bohm and Pines[7]
Cerenkov	$\left[1 - \frac{1}{\epsilon_\infty}\right]\frac{e^2\omega^2}{v}$ Note: $v = c$ = velocity of light in vacuum	See, e.g., Schiff[13]

---

[13] L. I. Schiff, *Quantum Mechanics*, p. 271, McGraw-Hill Book Co., New York, 1955.

Definitions for Table II

ϵ_0 = low-frequency dielectric constant

ϵ_∞ = high-frequency (optical) dielectric constant

K = dielectric constant

ϵ_p = piezoelectric constant

C = elastic modulus (dynes/cm^2)

ρ = density (grams/cm^3)

v_s = phase velocity of sound

v = velocity of electron

ω = angular frequency of radiation

B = deformation potential (electron volts in ergs/unit strain)

D = optical deformation potential (electron volts in ergs per centimeter relative shift of sublattices)

m = effective mass of electrons

---

being an uncertainty diameter, was assumed. This procedure may or may not have physical significance. It does allow ready comparison with the other rates of energy loss.

3. COUPLING CONSTANT

We need at this point to clarify the meaning of β. We consider first the loss to phonons, and write

$$\frac{1}{2}\left[\ \mathcal{E}_c{}^2-(\mathcal{E}_c-\mathcal{E}_p)^2\ \right]=\mathcal{E}_p{}^2+E_{elastic}, \qquad (6)$$

where $\mathcal{E}_c$ is the coulomb field of the electron, $\mathcal{E}_p$ is the (opposing) polarization field induced in the medium, and $E_{elastic}$ is the elastic energy stored in the medium (since a polarization field is accompanied by a mechanical strain or distortion of the medium). We have omitted factors of 8π and dielectric constants for simplicity and because they cancel out in the ratios obtained below. The left-hand side of Equation (6) is the coulomb energy per unit volume *available* for doing work in the medium. It is the difference between the electrostatic energy in the field of the electron before and after polarizing the medium. The factor 1/2 takes into account that the efficiency at which the stored energy can do useful work is, at most, 50%. The right-hand side of

Equation (6) is the energy imparted to the medium and consists of an electrical part $\mathcal{E}_p^2$ and an elastic or mechanical part $E_{elastic}$. An elementary example is that a strain in a piezoelectric crystal has an elastic energy that is distinct from the electrical energy due to the piezoelectric field.

For $\mathcal{E}_p \ll \mathcal{E}_c$, Equation (6) can be written

$$\mathcal{E}_c\mathcal{E}_p \doteq \mathcal{E}_p^2 + E_{elastic}. \tag{7}$$

Using Equation (7), we write for the fraction of coulomb energy used in forming the energy well,

$$\beta \equiv \underbrace{\frac{\mathcal{E}_c\mathcal{E}_p}{\mathcal{E}_c^2}}_{\substack{\text{Fraction of coulomb energy}\\ \text{used in forming energy well.}}} = \frac{\mathcal{E}_p^2}{\mathcal{E}_c\mathcal{E}_p} = \left(\underbrace{\frac{\mathcal{E}_p^2}{\mathcal{E}_p^2 + E_{elastic}}}_{\left.\frac{\text{electrical energy}}{\text{total energy}}\right]_{\text{phonon}}}. \right) \tag{8}$$

Equation (8) says that our general definition of β is equivalent to taking the ratio of electrical to total energy for the various phonons.

The values of β for the phonons in Table II are shown in square brackets. They were computed in Part I* for macroscopic sound waves and were used (see Table III) to characterize the various acoustoelectric effects. For polar optical waves, we used the Lyddane–Sachs–Teller relation for the ratio of frequencies of transverse and longitudinal modes and combined it with the fact that transverse modes have only elastic energy while the longitudinal modes have the same elastic energy plus an electric field energy due to polarization. For piezoelectric waves, the ratio of electrical to elastic energy is given by the square of the well-known electromechanical coupling constant. Since the electrical energy is small compared with the elastic energy, this ratio is a good approximation to the ratio of electrical to total energy. For the acoustic and nonpolar optical waves coupled by deformation potential, we computed the electrical energy as if the slope of the band edges due to the deformation potential were an actual field.

The values of β for the electronic excitations are close to unity for both plasmons and Cerenkov radiation, since the coulomb field of the electron is substantially canceled by electronic polarization and is therefore substantially completely used in digging an energy well. In the case of the deeper lying atomic levels (this is essentially the

---

* See *RCA Review*, March 1966, pp. 98-139.

problem treated classically by Bohr)[8], the tightly bound electrons can only partially cancel the coulomb field of the impinging electron since their contribution to the dielectric constant is near unity, namely, $1 + (\omega_p{}^2/\omega_c{}^2)$. Here $\hbar\omega_c$ is their binding energy, $\omega_p{}^2 = 4\pi ne^2/m$, and $\omega_p{}^2 \ll \omega_c{}^2$. It is this small value of dielectric constant that leads to the value of $\beta = \omega_p{}^2/\omega_c{}^2$ in Table II.

4. INNER RADIUS OF COULOMB FIELD

We have thus far given the dimensional form (Equations (3) and (5)) for the rates of energy loss and have defined the meaning of β as the fraction of available coulomb energy used in digging an energy well. What remains to be clarified further is the phrase "available coulomb energy." We have pointed out, for example, that in the case of loss to polar optical phonons the available coulomb energy is the vacuum field energy reduced by the high-frequency or electronic part of the dielectric constant. In the case of loss to electronic excitations, it is the vacuum field energy itself. What we have not yet defined is the inner radial limit of this coulomb field.

The inner radius is set by the uncertainty relation. This means, for example, that the radius of the smallest wave packet that can be formed for an electron whose maximum momentum is mv is of the order of $\hbar/mv$. Within this uncertainty radius the electronic charge is taken to be more or less uniformly distributed.

For energy loss to those phonons where the coupling is a real macroscopic electric field (polar optical and piezoelectric) the coulomb field energy extends from the uncertainty radius outward. Figure 2 shows schematically how this coulomb energy can, in the case of polar optical phonons where ω and β are constants independent of the λ of the radiated energy, be divided into a series of equivalent shells (in Figure 2, $\beta = K = 1$). The rate of energy loss for each of these shells is $\beta(e^2\omega^2)/(Kv)$. Summing up over the shells yields the following

$$\frac{dE}{dt} \approx \beta\frac{e^2\omega^2}{Kv}\ln\frac{r_o}{r_i}$$

$$\approx \beta\frac{e^2\omega^2}{Kv}\ln\frac{mv^2}{\hbar w}, \qquad (9)$$

so that the effect of the summation is to introduce a logarithmic factor. The outer radius is defined by $2r_o = v\omega^{-1}$ and is that radius beyond which the medium is slowly and reversibly polarized and depolarized

Table III—Time Constant (ω_a) for Rate of Change of Energy Density in Sound Waves

Phenomenon	ω_a	Source
Polar Optical	$\left[\dfrac{\epsilon_0 - \epsilon_\infty}{\epsilon_0}\right] \omega f(\omega_r, \omega_c, \omega_D)$	Gunn[14] Woodruff[15]
Piezoelectric Acoustic	$\left[\dfrac{\epsilon_p^2}{KC}\right] \omega f(\omega_r, \omega_c, \omega_D)$	Hutson, McFee and White[16]
Deformation Potential	$\left[\dfrac{KB^2\omega^2}{4\pi\rho e^2 v_s^4}\right] \omega f(\omega_r, \omega_c, \omega_D)$	Parmenter[17] Weinreich[18]
Nonpolar Optical	$\left[\dfrac{\pi K D^2}{\rho e^2 w^2 \lambda^2}\right] \omega f(\omega_r, \omega_c, \omega_D)$	
Intervalley Deformation Potential	$\left[\dfrac{nB^2}{\rho v_s^2 kT}\right] \omega f(\omega_r, \omega_c)$	Weinreich[19] Pomerantz[20]
Metals	$\left[1\right] \omega f(\omega_r, \omega_c)$ or $\omega^2 \tau_c$ for $\omega_r = \omega$ and $\omega \tau_c \ll 1$	Pippard[21] Levy[22]

Note that these expressions are valid for the mean free path of the electrons less than the wavelength of the sound wave.

---

[14] J. B. Gunn, "Traveling-Wave Interaction between the Optical Modes of a Polar Lattice and a Stream of Charge Carriers, "*Physics Letters,* Vol. 4, p. 194, 1 April 1963.

[15] T. O. Woodruff, "Interaction of Waves of Current and Polarization," *Phys. Rev.,* Vol. 132, p. 679, 15 Oct. 1963.

[16] A. R. Hutson, J. H. McFee, and D. L. White, "Ultrasonic Amplification in CdS," *Phys. Rev. Letters,* Vol. 7, p. 237, Sept. 15, 1961.

[17] R. H. Parmenter, "The Acousto-Electric Effect," *Phys.* Rev., Vol. 89, p. 990, March 1, 1953.

[18] G. Weinreich, "Ultrasonic Attenuation by Free Carriers in Germanium," *Phys. Rev.,* Vol. 107, p. 317, July 1, 1957.

[19] G. Weinreich, T. M. Sanders, Jr., and H. G. White, "Acoustoelectric Effect in n-Type Germanium," *Phys. Rev.,* Vol. 114, p. 33, April 1, 1959.

[20] M. Pomerantz, "Amplification of Microwave Phonons in Germanium," *Phys. Rev. Letters,* Vol. 13, p. 308, 31 Aug. 1964.

Definitions for Table III

$$\omega_a = \frac{1}{E}\frac{dE}{dt};\ E = \text{energy density of acoustic wave}$$

$$f(\omega_r, \omega_c, \omega_D) = \frac{\omega_r/\omega_c}{\left(1 + \dfrac{\omega_D}{\omega_c}\right)^2 + \left(\dfrac{\omega_r}{\omega_c}\right)^2}$$

$$f(\omega_r, \omega_c) = \frac{\omega_r/\omega_c}{1 + (\omega_r/\omega_c)^2}$$

$$\omega_r = \frac{v_d - v_s}{v_s}\,\omega$$

$$\omega_D = \frac{4\pi^2 kT\mu}{e\lambda^2}$$

$\omega_c = 4\pi\sigma/K$, or $\omega_c = \tau_c^{-1}$ for metals and intervalley deformation where τ_c is the time for an electron to come to thermal equilibrium

v_d = drift velocity of electrons

v_s = phase velocity of sound

ϵ_o = low frequency dielectric constant

ϵ_∞ = high frequency (optical) dielectric constant

K = dielectric constant

ϵ_p = piezoelectric constant

C = elastic modulus

B = deformation potential (electron volts in ergs/unit strain)

D = optical deformation potential (electron volts in ergs per centimeter relative shift of sublattices)

---

[21] A. B. Pippard, "Ultrasonic Attenuation in Metals," *Phil. Mag.*, Vol. 46, p. 1104, Oct. 1955.

[22] M. Levy, "Ultrasonic Attenuation in Superconductors for $ql < 1$," *Phys. Rev.*, Vol. 131, p. 1497, 15 Aug. 1963.

without significant energy loss. The same argument holds for energy loss to plasmons, in which case $\beta = K = 1$.

In the case of acoustic phonons coupled by piezoelectric fields the major loss is due to the innermost shell, and the logarithmic factor becomes unity. The outer shells by virtue of their larger dimensions excite longer wavelength radiations and hence are associated with smaller values of ω. Since ω enters in as ω^2, the contributions of the outer shells are small in comparison with the innermost shell.

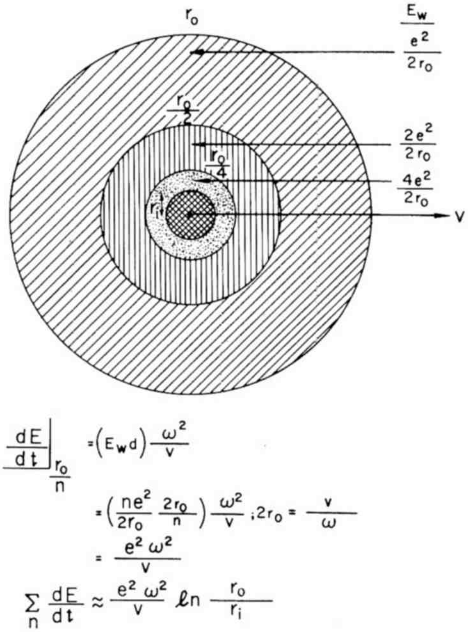

Fig. 2—Resolution of the rate of energy loss into a series of equivalent shells ($\beta = K = 1$ and $\omega =$ constant).

The energy loss to phonons coupled by a deformation potential can be cast in the same form as the other interactions in which the electric field plays a clearly identifiable role. To do so, the available coulomb energy is taken to be of the order of $e^2/(Kd)$ where d is the uncertainty diameter of the electron. While it is true that the concept of the deformation potential is not related in any direct or simple way to the coulomb field and energy, it may be more than accident that this particular value of the available coulomb energy is needed to satisfy the formalism.

The energy well for deformation potential coupling can also be obtained directly from balancing the interaction energy gained by an electron in a strained lattice with the energy needed to produce the strain;

$$\frac{1}{2}BS \approx \frac{1}{2}CS^2\left(\frac{4\pi}{3}r^3\right).$$

Here B is the deformation potential, S the strain, C an elastic constant, and r the uncertainty radius. The energy well is, therefore,

$$\frac{1}{2}BS \approx \frac{3B^2}{8\pi Cr^3}. \tag{10}$$

This value is inserted into Equation (3) to obtain the rate of energy loss.

Note that the inner radius enters only into the rather insensitive logarithmic factor for polar optical phonons. For the other phonons the inner radius has a first-order effect in determining the smallest wavelength or largest frequency (ω) phonon that can be emitted.

5. OTHER PROBLEMS

Equation (5) has also been applied to the rate of loss of energy to phonons via intervalley scattering; the computation is similar to that for loss to intravalley phonons coupled by a deformation potential. The difference is that the momentum required to emit the high-momentum phonons connecting the two valleys is obtained from the change in crystal momentum when the electron makes a transition between valleys, as well as from the local momentum of the electron in its valley.

Equation (5) is a useful approximation for computing energy loss via impact ionization across a forbidden gap, particularly if the forbidden gap is larger than the width of the valence band. The problem then approaches that for excitation of deep-lying atomic levels having a spread in excitation energies.

6. POLAR OPTICAL PHONONS

The rate of energy loss to polar optical phonons* is given by Equation (9) combined with the value for β taken from Part I*:

---

* See H. Fröhlich and N. Pelzer. "Polarization of Dielectrics by Slow-Particles," E.R.A. Report No. L/T184 (1948), for classical treatment of this problem.

* See *RCA Review*, March 1966, pp. 98-139.

$$\frac{dE}{dt} = \left[\frac{\epsilon_0 - \epsilon_\infty}{\epsilon_0}\right] \frac{e^2\omega^2}{\epsilon_\infty v} \ln \frac{mv^2}{\hbar\omega}. \tag{11}$$

According to Callen's[12] result, the logarithmic factor should have a factor of 2 in the numerator. Equation (11) is valid for $mv^2/2 > \hbar\omega$. Callen's factor is

$$\ln \frac{1 + \left(1 - \frac{\hbar\omega}{E}\right)^{1/2}}{1 - \left(1 - \frac{\hbar\omega}{E}\right)^{1/2}},$$

where $E = mv^2/2$. At $E = 2\hbar\omega$, this factor is already within 20% of $\ln(2mv^2/\hbar\omega)$.

It is instructive to also obtain Equation (11) directly from Equation (3), the primitive equation for rate of energy loss. The coulomb energy in a spherical shell of radius r and thickness dr is, in general,

$$dE = \frac{e^2}{Kr^2}\, dr. \tag{12}$$

Consider an electron moving slowly enough to polarize both the ionic and electronic parts of the surrounding lattice. Equation (12) then reads

$$dE = \frac{e^2}{\epsilon_0 r^2}\, dr. \tag{13}$$

Now let the electron move fast enough to polarize only the electronic part. Equation (12) becomes

$$dE = \frac{e^2}{\epsilon_\infty r^2}\, dr. \tag{14}$$

The difference between Equations (13) and (14) is then the energy per unit volume assignable to the polar optical modes. It is the energy well in a shell of diameter $2r$ and thickness dr. We insert this difference in Equation (3) for $d(E_w)$ and obtain

$$\frac{dE}{dt} = \int_{r_i}^{r_0} 2r \frac{\omega^2}{v} d(E_w)$$

$$= \frac{\epsilon_0 - \epsilon_\infty}{\epsilon_0 \epsilon_\infty} \frac{e^2\omega^2}{v} \int_{r_i}^{r_0} \frac{dr}{r}$$

$$= \left[\frac{\epsilon_0 - \epsilon_\infty}{\epsilon_0} \right] \frac{e^2\omega^2}{\epsilon_\infty v} \ln \frac{r_0}{r_i}, \qquad (15)$$

which is the same result as Equation (11).

The maximum rate of loss of energy occurs near $mv^2/2 = \hbar\omega$ and is, as pointed out in Equation (2), the product of the polaron energy well $\alpha\hbar\omega$ and the optical frequency ω.

7. PIEZOELECTRIC ACOUSTIC PHONONS

The rate of energy loss to acoustic phonons coupled by a piezoelectric field is, from Equation (5) with $\beta = \epsilon_p{}^2/(KC)$;

$$\frac{dE}{dt} \approx \frac{\epsilon_p{}^2}{K^2C} \frac{e^2\omega^2}{v}. \qquad (16)$$

This result is within a factor of 2 of a quantum mechanical calculation by perturbation theory,* namely,

$$\frac{dE}{dt} = \frac{2\epsilon_p{}^2}{K^2C} \frac{e^2\omega^2}{v}. \qquad (17)$$

The Cerenkov-type calculation by Tsu[2] matches Equation (17) except for a numerical constant of order unity.

The highest frequency phonon that can be emitted is given by

---

* G. D. Whitfield, private communication.

the condition for conservation of momentum[†];

$$\frac{\hbar w}{v_s} = 2mv. \tag{18}$$

Equation (18) inserted in Equation (17) yields

$$\frac{dE}{dt} = \frac{2}{C}\left(\frac{2\epsilon_p e v_s}{\hbar K}\right)^2 v. \tag{19}$$

8. DEFORMATION-POTENTIAL ACOUSTIC PHONONS

The rate of energy loss to acoustic phonons coupled by a deformation potential is most readily calculated using the primitive Equation (3). The expression for the energy well from Equation (10) is inserted into Equation (3) to obtain

$$\frac{dE}{dt} = \frac{3B^2\,\omega^2}{4\pi\, C\, r^2\, v}. \tag{20}$$

We use the relations[‡]

$$r \approx \frac{\hbar}{mv} \tag{21}$$

$$\frac{\hbar\omega}{v_s} = 2mv \tag{22}$$

and

$$C = \rho v_s^2 \tag{23}$$

to convert Equation (20) into

$$\frac{dE}{dt} = \frac{3}{\pi}\frac{B^2\, m^4}{\rho\hbar^4} v^3. \tag{24}$$

This is a factor of 3 larger than the result obtained by Seitz[1] and by Conwell[5] from perturbation theory.[#]

[†‡#] When the allowed transitions are weighted by a density of states factor, a more realistic value for the right hand side of Equations (18) and (22) is between mv and $2mv$. This refinement brings Equation (24) into substantial agreement with the literature and converts the numerical coefficients in Table II to values close to unity.

Equation (24) can also be obtained using Equation (5) and the value of β given by Equation (37) in Part I†;

$$\beta = \frac{B^2\omega^2 K}{4\pi e^2 \rho v_s^4}. \tag{25}$$

Substituting the expression for β into Equation (5) yields

$$\begin{aligned}\frac{dE}{dt} &= \beta \frac{e^2\,\omega^2}{Kv} \\ &= \frac{B^2\omega^4}{4\pi\,\rho v_s^4\,v} \\ &= \frac{4}{\pi}\,\frac{B^2\,m^4}{\rho\,\hbar^4}\,v^3. \end{aligned} \tag{26}$$

The fact that Equation (5) yields the same result as Equation (3) means that the electron acts *as if* its available energy for interacting with the lattice had the coulomb value $e^2/(Kd)$.* Whether or not this has physical significance, it does point up the fact that the available energy for forming an energy well has the same numerical value for interactions both by deformation potential and by macroscopic coulomb fields.

If one should read physical significance into the use of Equation (5) for deformation-potential coupling, he would be led to conclude that β, by its definition, cannot exceed unity. This would, by Equation (25), put an upper limit on the value of the deformation potential B, particularly at the highest values of ω. For example, as shown in Part I,† a value of 10 eV for B already leads to values of β in excess of unity at $\omega \approx 10^{14}$/sec.

9. NONPOLAR OPTICAL PHONONS

The rate of energy loss to nonpolar optical phonons is computed from Equation (3) in the same way as for acoustic phonons coupled by a deformation potential. The energy well follows from equating the electrical energy gained by the electron in deforming the lattice

---

† See *RCA Review*, March 1966, pp. 98-139.

* While the electronic charge does not appear explicity in Equation (26), it is contained implicitly in the magnitude of the deformation potential B.

to the elastic work done on the lattice. The deformation potential D for nonpolar optical phonons is defined as the shift in energy of the band edge per centimeter relative displacement of the two sublattices. (For acoustic phonons, B was defined in terms of the energy shift per unit strain.) Hence

$$\frac{1}{2} D\Delta x \approx \frac{1}{2} C(\Delta x)^2 \left(\frac{4}{3}\pi r^3\right) \tag{27}$$

and

$$\text{energy well} = \frac{1}{2} D\Delta x = \frac{3}{8\pi}\frac{D^2}{Cr^3}, \tag{28}$$

where Δx is the relative displacement of the sublattices, C is an elastic constant (per unit displacement), and r is the uncertainty radius.

Insertion of Equation (28) into Equation (3) yields

$$\frac{dE}{dt} = \frac{3}{4\pi}\frac{D^2\omega^2}{Cr^2v}. \tag{29}$$

Use of the relations

$$r \approx \frac{\hbar}{mv}$$

and

$$C = \rho\omega^2 \tag{30}$$

converts Equation (29) to

$$\frac{dE}{dt} = \frac{3}{4\pi}\frac{D^2m^2}{\rho\hbar^2}v. \tag{31}$$

Equation (31) is to be compared with Conwell's[5] result for $mv^2/2 \gg \hbar\omega$ and an isotropic effective mass,

$$\frac{dE}{dt} = \frac{1}{2\pi}\frac{D^2m^2}{\rho\hbar^2}v. \tag{32}$$

The complete form of Conwell's published result is

$$\frac{dE}{dt} = \frac{m_t m_l^{1/2} D^2}{2^{1/2}\pi\hbar^2\rho}\left[(\bar{n}+1)\left(\frac{1}{2}mv^2 - \hbar\omega\right)^{1/2} - \bar{n}\left(\frac{1}{2}mv^2 + \hbar\omega\right)^{1/2}\right] \tag{33}$$

where $\bar{n} = (\exp\{\hbar\omega/kT\} - 1)^{-1}$ = density of thermal phonons.

Equation (31) can also be obtained, as was done in the preceding section for acoustic phonons, from Equation (5) using the value of β obtained in Part I.* This formulation is shown in Table II. The implication, as before, is that the energy available for interacting with the lattice is the coulomb energy $e^2/(Kd)$.

10. INTERVALLEY SCATTERING

In the case of a many-valleyed band structure, an electron can lose energy to the lattice by making a transition from one valley to another (Herring[3]). For valleys widely separated in momentum space, the emitted phonons have a narrow spread in momentum around some high value of momentum. The phonons may be either acoustic or optical. An appropriate deformation potential is defined for each, just as in the preceding two sections, which is a measure of the relative energy shift of the two valleys per unit strain (per unit displacement of the two sublattices).

For energy loss to optical phonons the argument is the same as that used in the preceding section on nonpolar optical phonons and leads to the same result, namely,

$$\frac{dE}{dt} \approx \frac{3}{4\pi}\,\frac{D^2 m^2}{\rho\,\hbar^2}\,v. \tag{34}$$

For energy loss to acoustic phonons, the argument follows that already used for intravalley scattering and leads to Equation (20):

$$\frac{dE}{dt} = \frac{3}{4\pi}\,\frac{B^2}{Cr^2}\,\frac{\omega^2}{v}. \tag{35}$$

In the present case, however, ω has a large and relatively constant value obtained by matching $\hbar\omega/v_s$ with the change in crystal momentum suffered by the electron in making the transition between two valleys. This is in contrast to the argument in Section 8, where $\hbar\omega/v_s$ was equated to the local momentum at the electron in its valley. Hence we use only the two relations

---

* See *RCA Review*, March 1966, pp. 98-139.

$$r \approx \frac{\hbar}{mv}$$

and

$$C = \rho\, v_s^2$$

to obtain

$$\frac{dE}{dt} = \frac{3}{4\pi} \frac{B^2 m^2 \omega^2}{\rho\, v_s^2\, \hbar^2} v. \tag{36}$$

Equation (36) has the same dependence on v as Equation (34). Moreover, for large values of ω the coefficients of the two expressions have the same order of magnitude insofar as

$$\frac{B\omega}{v_s} = \frac{2\pi B}{\lambda} \approx D. \tag{37}$$

11. PLASMONS AND X-RAY LEVELS

The treatment of energy loss to plasmons and to the deeper-lying atomic levels (x-ray levels) follows closely that of energy loss to polar optical phonons. In all three cases ω is substantially a constant, independent of wavelength, so that the problem approximates that of a set of independent oscillators. Hence, in this limit, they can be treated (for energy-loss calculations) either as independent oscillators (Bohr) or formally as a set of collective modes of oscillation (Bohm and Pines). Furthermore, since the condition for Equation (3) is $\omega\tau < 1$, the incident electron makes its transit in times short compared with the reaction time ω^{-1} of the medium. Thus, even the local oscillators "look" like free particles.

We begin with Equation (15) which was derived from Equation (3):

$$\frac{dE}{dt} = \frac{K_1 - K_2}{K_1 K_2} \frac{e^2\omega^2}{v} \ln \frac{r_o}{r_i}. \tag{38}$$

Here the real part of the dielectric constant that the electron sees is K_1 when its energy is less than $\hbar\omega$ and K_2 when its energy exceeds $\hbar\omega$.

For plasmons, K_1 is the usual electronic part of the dielectric constant and K_2 is close to unity. The $\hbar\omega$ of the plasmon appropriate to a filled valence band is taken to be of the order of 10 eV. Hence

$$\frac{K_1 - K_2}{K_1 K_2} \doteq \frac{K_1 - 1}{K_1} \doteq 1, \qquad (39)$$

and Equation (38) becomes

$$\frac{dE}{dt} = \frac{e^2\omega^2}{v} \ln \frac{r_o}{r_i}. \qquad (40)$$

The outer radius, as before, is given by $2r_o = v\omega^{-1}$ and is that distance beyond which the medium is reversibly polarized and depolarized with negligible energy loss. The inner radius is normally taken to be a Debye screening length $v_F\omega^{-1}$ where v_F is the Fermi velocity. For shorter distances, the incident electron excites individual electrons rather than collective oscillations. Since, however, the individual excitations follow the same form as Equation (40) (see below), we can take r_i to be the uncertainty radius in order to write the total energy loss to plasmons and electron–electron collisions as

$$\frac{dE}{dt} = \frac{e^2\omega^2}{v} \ln \frac{mv^2}{\hbar\omega}. \qquad (41)$$

Equation (41) can also be obtained by an elementary treatment of particle-to-particle interactions. The momentum imparted to an electron at a distance r from the path of the incident electron is approximately

$$\begin{aligned}\Delta p &= \frac{e^2}{r^2} \Delta t \\ &\doteq \frac{e^2}{r^2} \frac{2r}{v} \\ &= \frac{2e^2}{rv}. \qquad (42)\end{aligned}$$

The energy imparted is

$$\frac{(\Delta p)^2}{2m} = \frac{2e^4}{mv^2r^2}. \qquad (43)$$

The total energy imparted per unit time to a density of n electrons/cm^3 is

$$\begin{aligned}\frac{dE}{dt} &= \frac{2ne^4}{mv^2}\int_{r_i}^{r_0}\frac{1}{r^2}(2\pi r)\,dr\\ &= \frac{4\pi ne^4}{mv}\int_{r_i}^{r_0}\frac{dr}{r}\\ &= \frac{e^2\omega_p{}^2}{v}\int_{r_i}^{r_0}\frac{dr}{r}\end{aligned} \tag{44}$$

where $\omega_p{}^2 \equiv 4\pi ne^2/m =$ (plasma frequency)^2. The inner radius has the uncertainty value $\hbar/(mv)$. The outer radius is the adiabatic radius $v\tau$ where τ is the time for the electron gas to relax an electric field. By elementary considerations, $\tau = \omega_p{}^{-1}$. Hence Equation (44) becomes

$$\frac{dE}{dt} = \frac{e^2\omega_p{}^2}{v}\ln\frac{mv^2}{\hbar\omega_p}. \tag{45}$$

It is worth noting that the loss to polar optical phonons can be treated in the same way, namely as a particle-to-particle interaction between the incident electron and a gas of free ions. The result is a close match to Equation (11), since ω_p (ions) $\approx \omega_{optical\ phonon}$.

In the case of energy loss to the deeper-lying atomic levels, we make use of the following relation for the lower frequency dielectric constant K_1:

$$K_1 = 1 + \frac{\omega_p{}^2}{\omega_e{}^2}, \tag{46}$$

where $\omega_p{}^2 = 4\pi ne^2/m$ and $\hbar\omega_e$ is the excitation energy for the deep level and is larger than $\hbar\omega_p$. K_2 as before is near unity. Hence,

$$\frac{K_1 - K_2}{K_1K_2} \doteq \frac{\omega_p{}^2}{\omega_e{}^2}, \tag{47}$$

and Equation (15) for these deeper levels becomes

$$\begin{aligned}\frac{dE}{dt} &= \left[\frac{\omega_p{}^2}{\omega_e{}^2}\right]\frac{e^2\omega_e{}^2}{v}\ln\frac{mv^2}{\hbar\omega_e}\\ &= \frac{e^2\omega_p{}^2}{v}\ln\frac{mv^2}{\hbar\omega_e}.\end{aligned} \tag{48}$$

The factor ω_p^2/ω_c^2 is the fraction of the coulomb energy of the incident electron that is used in forming an energy well by polarizing the electrons in the deep-lying levels.

12. IMPACT IONIZATION

In the case of the deeper-lying atomic levels, the ground state energy was well defined and common to all of the electrons. The electrons in the valence band of a semiconductor are, by contrast, spread over a range of energies. Thus, as the energy of an impinging electron is increased, it is at first able to ionize only the electrons in the top edge of the valence band. Further increase in energy allows the impinging electron to reach deeper into the valence band. A first-order estimate of the rate of energy loss by the impinging electron can be obtained using the concepts already applied to polar optical phonons, plasmons, and the deeper atomic levels. In brief, we compute the real part of the dielectric constant as a function of the energy of the incident electron and use the relation

$$\frac{dE}{dt} = \left(\frac{1}{K_1} - \frac{1}{K_0} \right) \frac{e^2 \omega^2}{v} \tag{49}$$

to compute the rate of energy loss. This is Equation (15) with the logarithmic factor taken to be unity since $mv^2/2 \approx \hbar\omega$. K_0 is the dielectric constant when the incident electron is just at the threshold of impact ionization, namely when its energy is equal to the energy E_g of the forbidden gap. K_1 is the dielectric constant for a somewhat higher incident energy $E = E_g + \Delta E$. We use the approximation that K_1 is proportional to the number of electrons in the valence band that are *too deep* to be ionized. Hence

$$\frac{K_1}{K_0} = \frac{n_0 - A(\Delta E)^{3/2}}{n_0}$$

and

$$\frac{K_0 - K_1}{K_0} = \frac{A(\Delta E)^{3/2}}{n_0}$$

$$= \left(\frac{\Delta E}{E_0} \right)^{3/2}, \tag{50}$$

where $n_0 =$ total number of electrons in the valence band and E_0 is an energy comparable with the width of the valence band and defined by $n_0 = AE_0^{3/2}$. We take $\hbar\omega \approx E = E_g + \Delta E$ and $v = (2E/m)^{1/2}$. With these relations Equation (49) becomes

$$\frac{dE}{dt} = \frac{e^2 m^{1/2}}{2^{1/2}\hbar^2 K_1} \left[\frac{(\Delta E)(E_g + \Delta E)}{E_0} \right]^{3/2}. \tag{51}$$

For $\Delta E \ll E_g$, Equation (51) matches the $(\Delta E)^{3/2}$ dependence obtained by Motizuki and Sparks.[6] It is worth noting also that if we were to let E_g become small in comparison with ΔE in order to approach the conditions of a metal, the dependence on ΔE becomes $(\Delta E)^3$, which is that found by Quinn[23] for metals.

13. CERENKOV RADIATION

When the velocity of a high-speed electron exceeds the velocity of light in a solid, a new channel for energy loss, namely electromagnetic radiation, is opened up. There are various conceptual approaches to the analysis of Cerenkov radiation. Quantum mechanically, the radiation may be looked upon as induced by the zero point fluctuations in the radiation field. The radiation may also be computed classically by resolving the pulse of electric field, as seen by an element of the medium when the electron passes nearby, into its Fourier components.

What we wish to show here is that the expression for the total Cerenkov radiation matches Equation (5) for velocities close to the velocity of light in vacuum. The expression for the total Cerenkov radiation (see e.g. Schiff[13]) is

$$\frac{dE}{dt} = \int_0^{\omega} \frac{e^2 \omega^2 v}{c^2} \left(1 - \frac{c^2}{\bar{n}^2 v} \right) d\omega. \tag{52}$$

Here v is the velocity of the electron, c is the velocity of light in vacuum, $\bar{n}$ is the index of refraction and is a function of ω. The upper limit of integration is the highest frequency for which the index of refraction exceeds unity. In the limit for $v \rightarrow c$, and using the approximation of a constant index n, Equation (52) becomes

---

[23] J. J. Quinn, "Range of Excited Electrons in Metals," *Phys. Rev.*, Vol. 126, p. 1453, 15 May 1962.

With these substitutions Equation (55) becomes

$$\frac{dE}{dt} = 4\pi\beta E_t \frac{ne^2\tau_c}{Km}\frac{v_s}{v}, \tag{56}$$

and the energy loss per electron is

$$\frac{dE_1}{dt} \equiv \frac{1}{n}\frac{dE}{dt} = 4\pi\beta E_t \frac{e^2\tau_c}{Km}\frac{v_s}{v}. \tag{57}$$

Equation (57) is a classically derived expression for which

$$\text{mean free path of electron } l \ll \frac{\lambda}{2\pi}. \tag{58}$$

On the other hand, the perturbation treatment of the emission of phonons by individual electrons is valid for $l > \lambda/(2\pi)$. If the two have a common region, it should be near $l = \lambda/(2\pi)$. Hence we evaluate Equation (57) at the junction:

$$l = \frac{\lambda}{2\pi}$$

or

$$\tau_c \equiv \frac{l}{v} = \frac{\lambda}{2\pi v}. \tag{59}$$

Equation (59) inserted in Equation (57) gives

$$\frac{dE_1}{dt} = 2\beta E_t \frac{e^2\lambda}{Km}\frac{v_s}{v^2}. \tag{60}$$

E_t is normally the total energy density of a coherent sound wave. In the present argument the only available energy is that of the incoherent zero-point vibrations. Their energy density in the interval $\lambda \pm \lambda/2$ and resolved along the axis of electron motion is

$$E_t = \frac{1}{3}\frac{8\pi\,\hbar\omega}{\lambda^3}. \tag{61}$$

With this value for E_t, Equation (60) becomes

$$\frac{dE_1}{dt}=\frac{16\pi}{3}\frac{\beta e^2\hbar\omega v_s}{Km\lambda^2v^2}. \tag{62}$$

We use the momentum condition

$$2mv=\frac{\hbar\omega}{v_s}$$

and the definition

$$\lambda=\frac{2\pi v_s}{\omega}$$

to convert Equation (62) to

$$\frac{dE_1}{dt}=\frac{8}{3\pi}\beta\frac{e^2\omega^2}{Kv}. \tag{63}$$

This is the essential form of all of the expressions for rates of loss of energy in Table II.

16. GENERAL REMARKS

A. The Role of Quantum Constraints

The core of the argument for energy loss, Equations (3) and (5), is classical. Quantum effects are introduced as constraints.

For example, the major contribution of quantum mechanics in the case of polar optical phonons, electronic excitations, and plasmons is to determine an energy threshold $mv^2/2 > \hbar\omega$ at which significant energy loss sets in. A secondary contribution in each case is to determine a momentum-controlled inner radius, as opposed to the classical energy-controlled inner radius, in the logarithmic factor.

In the case of piezoelectric phonons, the maximum value of ω is constrained quantum mechanically to a value satisfying the momentum relation

$$2mv=\frac{\hbar\omega}{v_s}.$$

The energy relation is less restrictive,

$$\frac{mv^2}{2}=\hbar\omega.$$

The momentum relationship reduces the highest phonon frequency ω with which an electron can interact to values of the order of v_s/v times smaller than that allowed energetically. The same is true for the acoustic phonons coupled by deformation potentials.

In the case of nonpolar optical phonons, the quantum constraints impose both an energy threshold, as for polar optical phonons, and an upper limit to the wave vector of the dominant phonon interaction, as for acoustic phonons.

Note that in the classical model the incident electron moves in a straight line emitting energy symmetrically and simultaneously around its line of flight. It is, by definition, not scattered. Scattering is introduced by imposing the quantum constraint that this same average rate of emission of energy takes place via the emission of a *sequence* of *individual* phonons.

B. Summary of Rates of Energy Loss

Figure 3 summarizes the rates of loss of energy to the various types of phonons as a function of electron energy. Representative values were chosen for the bracketed factors in Table II. The factors are the ratios of electrical to total energy for the several phonons.

To represent energy loss to polar optical phonons in the alkali halides the following values were used:

$$\frac{\epsilon_0 - \epsilon_\infty}{\epsilon_0} = 0.5,$$

$$\epsilon_\infty = 2.5,$$

$$\omega = 5 \times 10^{13}/\text{sec},$$

$$\frac{m}{m_o} = 1.$$

At the other extreme, the following values were used to approximate energy loss to polar optical phonons in a material such as InSb:

$$\frac{\epsilon_0 - \epsilon_\infty}{\epsilon_0} = 0.05,$$

$$\epsilon_\infty = 20,$$

$$\omega = 5 \times 10^{13}/\text{sec},$$

$$\frac{m}{m_o} = 10^{-2}.$$

For piezoelectric phonons a value of ϵ_p^2/KC of 0.05 was used to approximate CdS.

For deformation-potential acoustic phonons, B was chosen to be 10 eV or 1.6×10^{-1} erg. This value is of the order of that found in germanium. For nonpolar optical phonons, D was taken to be 4×10^8 eV/cm. This value is quoted by Conwell for germanium.

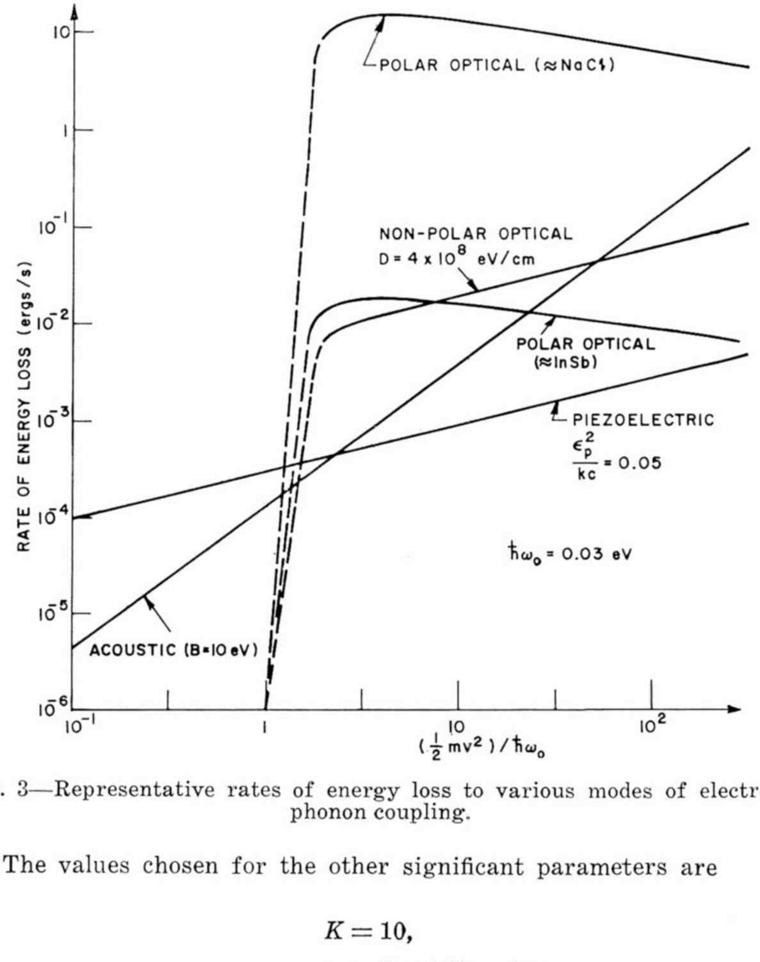

Fig. 3—Representative rates of energy loss to various modes of electron–phonon coupling.

The values chosen for the other significant parameters are

$$K = 10,$$

$$v_s = 3 \times 10^5 \text{ cm/sec},$$

$$\rho = 10 \text{ gms/cm}^3,$$

$$\frac{m}{m_o} = 0.2,$$

$$\omega_{\text{optical}} = 5 \times 10^{13}/\text{sec}.$$

The energy scale for the emitting electron is plotted in units of $\hbar\omega_{optical}$ where $\hbar\omega_{optical} = 0.03$ eV. The width of the conduction band is taken to be 10 eV.

For comparison, the order of magnitude of the rate of loss to Cevenkov radiation is 10^3 ergs/sec and to plasmons is 10^5 ergs/sec.

One virtue of expressing the rates of energy loss in the format of Table II is that the upper limit to the rate of energy loss to any type of radiation is clearly defined by

$$\frac{dE}{dt} = \frac{e^2\omega^2}{v} \ln \frac{2mv^2}{\hbar\omega}. \tag{64}$$

This is the maximum rate of energy loss obtained by setting $\beta = 1$ and $K = 1$. In effect, all of the vacuum coulomb energy of the electron is used to form an energy well.

The entries in Table II can be used to compute the mean free path for emitting a quantum of radiation, since

$$\begin{aligned} l &\equiv \frac{\hbar\omega}{dE/dx} = \frac{\hbar\omega v}{dE/dt} \\ &\approx K \frac{r_H}{\beta} \frac{mv^2}{\hbar\omega} \frac{m_o}{m} \times \left\{ \begin{array}{c} 1 \\ \text{or} \\ 1/[\ln\,(2mv^2/\hbar\omega)] \end{array} \right. \end{aligned} \tag{65}$$

where r_H is the Bohr radius of the hydrogen atoms and m_0 is the mass of a free electron.

Insertion of the values of β, taken from Table II, into Equation (65) yields the following dependencies of the mean free path on the velocity of the electron when the thermal density of phonons is negligible:

polar optical	$l \propto \dfrac{v^2}{\ln\,(2mv^2/\hbar\omega)}$
non-polar optical	$l \propto$ constant
acoustic (piezoelectric)	$l \propto v$
acoustic (deformation potential)	$l \propto v^{-1}$

ACKNOWLEDGMENTS

The concepts outlined in this paper have been developed over a period of several years. During this time I have had the generous guidance and criticism of many of my colleagues. By far, the major guidance has come from Professor George Whitfield of Pennsylvania State University to whom I am deeply indebted for the patience and insight needed to bridge the gap between my elementary classical concepts on the one hand and the formal rigor of perturbation theory on the other.

This work was supported by the U. S. Army Research Office—Durham, Durham, North Carolina under Contract No. DA-31-124-ARO(D)-84 and by the U. S. Army Engineer Research and Development Laboratory, Fort Belvoir, Virginia, under Contract No. DA44-009-AMC-1276(T); and by RCA Laboratories, Princeton, N. J.

SYNCHRONIZATION DURING BIASED PCM CONDITIONS

By

E. D. Bloedel

RCA Service Company
Camden, N. J.

Summary—*In this paper the effects of the transmission of heavily biased information on pulse-code-modulation (PCM) data systems are investigated. The following three areas are considered: (1) the time required for synchronization, (2) the binary digit composition of the sync code, and (3) the amount of information associated with the act of synchronizing. In the telemetry example cited there are twice as many zeros as ones in the transmitted information. An extension is made from this bias to show that if a priori knowledge is available concerning the statistical distribution of ones and zeros, an improved synchronization code can be designed. Pseudo-random and the classical Barker codes are reviewed to determine their usefulness for sync codes under biased data conditions.*

It is shown that for the synchronization process described, no apparent advantage is gained by selecting one of these codes over an arbitrarily selected random sync pattern. It is further shown that the best method for minimizing the synchronization time in a biased-data environment is to bias the sync pattern in an opposite fashion. In the telemetry example cited, the bias knowledge is derived from the characteristics of the transducer measurements; in the digital television illustration, the bias is determined by the expected picture signature and the encoding techniques employed. The information associated with the synchronization process is shown to be primarily influenced by the knowledge of when the synchronization signal is to be transmitted and by the channel equivocation.

INTRODUCTION

DIGITAL COMMUNICATION systems normally require synchronization between the transmitter and receiver. Transmission of a serial train of binary ones and zeros in itself contains no information unless some technique is provided to unscramble, decode, or decommutate the serial data. The role of the synchronizer, located at the receiving station, is to properly unscramble this data and subsequently provide a smooth flow of coherent information. The synchronization process normally requires two phases before coherency is established; (1) bit sync and (2) frame (or message) sync. It is assumed that an adequate circuit is provided for bit sync. Only synchronization of the prime or main frame is considered here, since other data frames that have been sub or super commutated are but a special case of the analysis discussed in this paper.

The analysis of PCM synchronization usually assumes one of two forms. The first method investigates single-look statistics to determine the probability that true sync will occur at the very first passage of the sync code, which is concealed within the frame of data. The second approach determines the statistical average of the number of frames that pass before true sync occurs. In this report the latter method is chosen because the results are more meaningful, especially in determining the amount of data that is lost if synchronization is not properly maintained.

Group or frame synchronization for PCM telemetry and digital television is not a serious problem at high S/N. However, under conditions of antenna wobble, rocket plume attenuation, multipath, Faraday rotation, phase jitter, or other conditions producing signal fading, a low S/N may result either for short or sustained durations of time. Under such conditions synchronization is more difficult to maintain, and it may be that the data being transmitted at that time is most important.

While in many instances the statistical distribution of binary digits may be random $(P(0)=P(1)=1/2)$, conditions do exist in which the distribution of binary digits may be heavily biased, e.g., $(P(0)=0.2$, $P(1)=0.8$. Consider a 10-bit sync code, and let it be assumed that on the average eight out of ten data bits are "ones." Let us therefore select approximately eight out of ten sync bits to be "zeros." Under these circumstances, the probability that 10 data bits may be arranged as a sync pattern is $(0.2)^8\ (0.8)^2 = 1.6 \times 10^{-6}$. If the data bits are equally probable, then this probability is simply $(1/2)^{10} \cong 10^{-3}$. This corresponds to nearly three orders of magnitude decrease in probability for this simple example, and represents a certain amount of increased performance; the conditions under which this increase is significant or marginal are investigated in subsequent sections.

The requirement, when such a scheme for synchronization is considered, of a priori knowledge concerning the statistical distribution of binary data will also be discussed in later sections.

SYSTEM CONFIGURATION

PCM telemetry, digital television, and other communications systems require that airborne and ground-based equipment be in synchronization at all times. During those instances in which synchronization is lost, data is unusable. Experience has indicated that a unique code or word, inserted within the airborne data, provides sufficient information to enable the ground PCM installation to recognize the precise time at which airborne data words, lines, and frames are generated, and therefore allows proper decommutation. Consider the generalized

PCM data system illustrated in Figure 1. The sensors may consist of strain, temperature, pressure or other transducers, optical devices, or audio sensors. Each channel is sampled and subsequently converted into a data word by the A/D converter. The sampling rate (or frequency) of the analog input voltages from each channel is slightly higher than the Nyquist sampling rate $(2Wc)$[*] to reduce errors associated with imperfect filtering (aliasing errors). Normally, the digital word describing the amplitude of the sampled analog data is 5 to 10 bits in length, depending upon the quantization accuracy or contrast level required. For the television application, the eye can theoretically distinguish about 100 gray levels; however, it is common practice to use only a five-bit code, or 32 contrast levels. For a picture frame with 300 × 300 resolution elements, each line contains 1500 bits and, therefore, 0.45 megabit per frame.

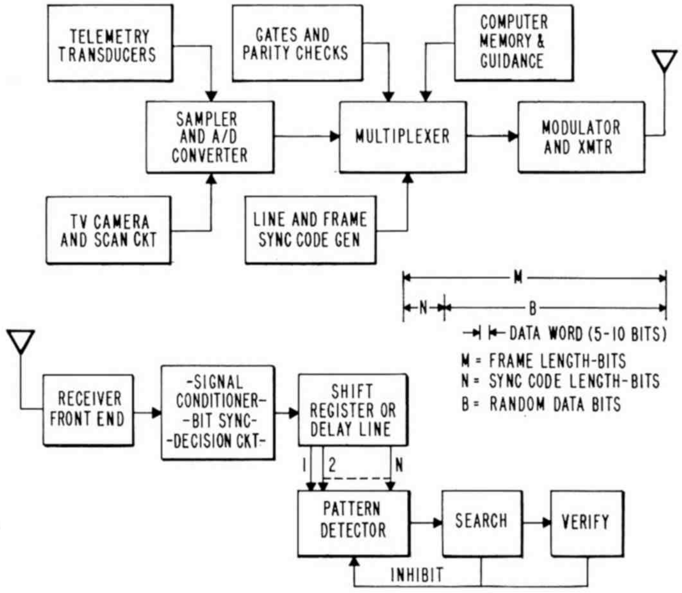

Fig. 1—PCM generalized data system.

At the output of the A/D converter, other digital inputs are usually inserted, as shown in Figure 1, including the sync code. Although the length of the synchronization code may vary depending upon several system parameters, the minimum length is given from information

[*] It is assumed the signal is band limited to Wc Hz.

theory as $\log_2 m$, where m is the frame length. Another important property of the sync code, in addition to the length, may be its actual sequence of ones and zeros. Present theories concerning the best or optimum sequence are somewhat at variance; however, the finite time autocorrelation (FTA) or cyclic autocorrelation function, defined as $\int_0^T f(t)\, f(t+\tau)\, dt$, is considered a valuable measure of the "goodness" of a sequence. A good FTA function in the above sense is one with a high central peak and low clutter values. It is usually such a sync code, in conjunction with the sampled data bits, that modulates the airborne transmitter as shown in Figure 1.

One frame of m bits having n sync bits, may correspond to one revolution of the airborne telemetry prime commutator or one television line, the length of which usually varies from 300 to 3000 bits. The fraction of the total data transmission capacity devoted to synchronization is, therefore, the ratio n/m (for a typical data system $30/1000 = 3\%$). Upon reception the data passes into the synchronizer, which searches for the proper identification code, provides verification of this code, and initiates the necessary control functions to the decommutator network.

Actual PCM-telemetry-data tapes from missile test programs at Cape Kennedy were evaluated to determine the distribution of binary ones and zeros. The telemetry data transmitted via the r-f link originated as sampled and digitized outputs of power, pressure, strain, temperature, displacement, and other miscellaneous transducers. Analysis of about 50 million data bits from several test flights showed twice as many zeros as ones in the transmitted data. Since no strong correlation was noted (see Reference (5)) between one bit position and the next, the channel was assumed zero order Markov (independent bits). In all probability a similar result would be experienced in the analysis of the binary digits being transmitted from a digital television system. As the camera scans across a dark object, the majority of resolution elements will be of low contrast, and consequently each will be encoded into nearly all zeros.

TIME REQUIRED FOR SYNCHRONIZATION

The mean value for the numbers of frames that will pass the synchronizer before a true sync pattern is reached is the quantity that describes the average time required for synchronization. This mean value is given by the product of the probability of a true decision in each frame of data times the number of frames required to reach that decision. The appendix contains a brief derivation and summary of the significant equations required to establish the mean time required to sync. This is a standard approach and the reader is referred to References (5)-(8) for a more detailed analysis. It is found that the mean number of frames to arrive at true synchronization depends upon the frame length (m), sync code length (n), the number of ones (r), and zeros (s) in the sync code $(r+s=n)$, bit error probability (p_g), probability of a binary one (p) and zero (q) at the channel output, and finally the numbers of errors (e) allowed in the search and check modes. A computer program has been written to solve the equations that appear in this appendix, and whose results appear in this paper.

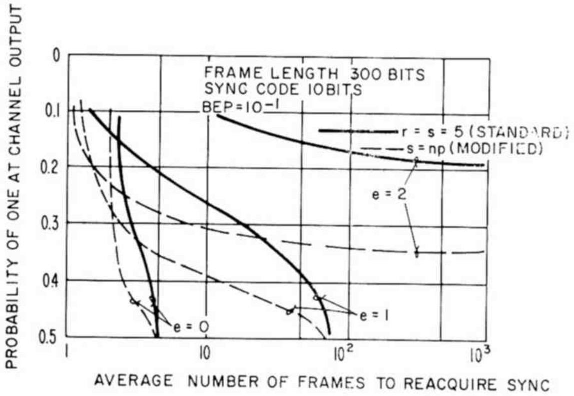

Fig. 2—Mean time to sync versus data bias.

Consider the case of a data system that utilizes 3% of its capacity for synchronization and contains a prime frame length of 300 bits and a sync code length of two five-bit data words, or ten bits. Under normal operating conditions it can be shown that there is an optimum setting for the numbers of errors to be allowed in the pattern recognizer when S/N is low. A rule of thumb for the number of errors to allow might be of the order of 10 to 20% of the sync code length. Figure 2 shows the mean time required to sync for different amounts of bias in the data and is plotted for three different values of errors allowed in the pattern recognizer.

The solid curve illustrates the normal condition when the number of ones and zeros in the sync code remain the same, and the dotted curve depicts the difference when the code is chosen to complement the amount of bias in the data. The curve is plotted for the lower limit of usable data at a bit error probability of 0.1. It is important to note that in all cases (except $p=0.5$) it is possible to improve performance if a priori knowledge is available regarding p, the probability of a binary one. While in some instances the improvement is marginal, other cases reveal an extremely large improvement.

CODE STRUCTURES

The previous section considered synchronization from the point of view of certain system parameters, but did not include the actual sequence of ones and zeros. In this section, an attempt is made to determine whether any particular sequence is more desirable than any other. This brief discussion is not rigorous, but rather a heuristic explanation of some fundamental concepts that affect PCM synchronization. In determining the desirability of one code with respect to any other, it is paramount that the application of the data system be considered. The two primary applications considered have been PCM telemetry and digital television. Both examples require that a unique code be inserted within the data to instruct the terminal conversion equipment to properly decommutate or unscramble the encoded information. To accomplish this objective successfully, it is desirable that the sync code possess some property that will distinguish it from the encoded information. The amount of likeness or resemblance between the sync code and the encoded information is measured by the correlation between the two. It would seem reasonable, therefore, that the correlation properties of a particular sync code would be of interest.

Feedback-shift-register-generator (SRG) sequences have been chosen to demonstrate the correlation property we seek to investigate. The properties of SRG sequences are well known to most communication engineers; an excellent treatment of this subject is provided in Reference (2).

Two approaches are available to determine the properties of SRG sequences; the first is to construct in the laboratory the necessary shift registers and feedback connections, and physically generate the given sequence. Perhaps a more convenient technique is to use matrix theory to represent the shift register or generator, and the theory of algebraic polynomials and their factors to determine the properties of sequences from such a generator. The latter technique was used to generate the SRG sequences for purposes of this paper. Table I is a summary of all maximal length SRG sequences up to and including length 31. All sequences listed in this table, some of which are not SRG, have the good (high central peak and low clutter values) finite time autocorrelation found in the classical Barker Codes.

Consider a group of Barker seven-bit code words (1110010) trans-

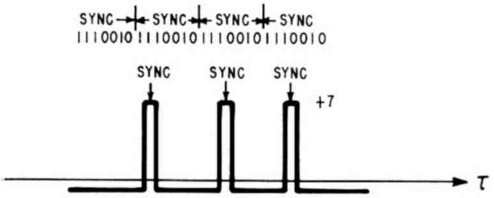

Fig. 3—Correlation of 7-bit SSRG sequence (Barker) with itself.

mitted one after the other. Figure 3 illustrates the correlation of this code with itself (autocorrelation). In essence, what this graph signifies is that there is 100% positive likeness or correlation when the code is aligned with itself and negative correlation for all other times. The above format does not, however, represent an actual data system, since there normally is a large amount of random data between sync codes. Consider this same seven-bit Barker code, which is also a maximal-length simple-shift-register-generator (SSRG) code, inserted in the

Table I—Unique Codes Up to Length 31

Length	SRG Feedback Connection*	Sequence
3	(2,1,0)	110 (Barker)
4	B NA	1101
5	B NA	11101
7	(3,1,0)	1110100
7	(3,2,0)	1110010 (Barker)
11	NA	11100010010 (Barker)
13	B NA	1111100110101
15	(4,1,0)	111101011001000
15	(4,3,0)	111100010011010 (Ref. (8))
19	NA	1111001001100001010
23	NA	11110000010100110011010
31	(5,2,0)	1111100110100100001010111011000 (Ref. (8))
31	(5,3,0)	1111100011011101010000100101100
31	(5,3,2,1,0)	1111101110001010110100001100100
31	(5,4,3,2,0)	1111100100110000101101010001110
31	(5,4,2,1,0)	1111101100111000011010100100010
31	(5,4,3,1,0)	1111101000100101011000011100110

* See Reference 2 for a complete explanation.

B = Sometimes referred to as Barker codes but do not fulfill original Barker Conditions

NA = Not a maximal length SRG sequence

random 50% data.* As depicted in Figure 4, the correlation between this code and the random data no longer contains the above-illustrated unique autocorrelation property. In fact, for this particular sample of random data, it is seen that a false alarm is nearly generated in the +5 response, ten shift positions from sync. This is but one example illustrating that the application must be carefully considered before the unique properties of Barker or pseudo-random codes are used.

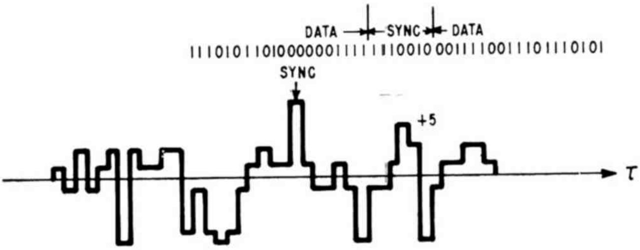

Fig. 4—Correlation of 7-bit Barker code with random 50% data.

While it may be true that such codes can be used in radar applications to improve the ambiguity surface, or in spread-spectrum communication concepts to match the receiver bandpass to the transmitted waveform, there appears to be less evidence for their applicability for PCM synchronization. Nevertheless, these codes are as good as any other for random 50% data bits.

We now seek to investigate correlation properties of sync codes containing an uneven distribution of ones and zeros. Consider a system in which seven out of 10 data bits are ones. The previous section, covering the mean time to sync, indicated it would be desirable to use sync codes containing more zeros than ones under these circumstances. One such code is a 17-bit impulse response SSRG sequence. This code is simply a special form of a truncated pseudo-random code (see Reference (2)) that contains more zeros than ones. The correlation of this code with data biased to a value of $P(0) = 0.3$ is shown in Figure 5. It is seen that at shifts far from the true sync position, there is strong negative correlation. At shift positions closer to true sync, the correlation, although positive, is still at acceptable levels. Spot checks of random biased data, complemented with a biased sync code, shows similar acceptable performance even if the sync code is simply picked from a set of independent random bits.

---

* All random data, whether biased or unbiased, have been taken from the random-number table of Reference (4).

INFORMATION CONTENT

The previous sections have dealt with both the length of the synchronization code and its structure with regard to the composition of binary digits. One question that arises as a result of these considerations is how much information actually is conveyed by the act of synchronization. This quantity, measured by its entropy, depends upon the a priori knowledge of when the sync code is most likely to be received. The condition that exists in the reception of each successive digit is described by the following: of the previous n digits received, y agree with the sync code and x do not. We ask if the last digit received is to signify the synchronization instant. It has been established in the previous two sections that it does indicate sync if $x \leqq e$, the number of errors allowed in the pattern detector.

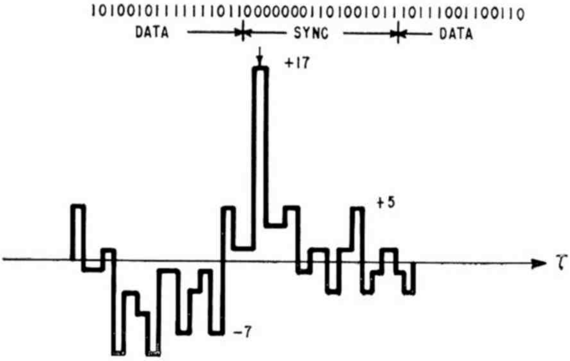

Fig. 5—Correlation of 17-bit impulse response SSRG sequence with biased $P(0) = 0.3$ data.

The equivocation, as defined by Shannon, measures the uncertainty about the input when the output is known (and vice versa) and is a measure of the amount of information lost in the communication channel. In this application, the output is known to the extent that y out of n digits agree with the synchronizing pattern, and there is a corresponding uncertainty as to whether the synchronizing signal is at this position. By the application of Bayes theorem, the a posteriori probability $P(x)$ that the present signal received with x errors is false can be approximated by (see Reference (3)):

$$\frac{(1-S)\,2^{-n}}{(1-S)\,2^{-n} + Sp_g^{\,x}\,(1-p_g)^{y}}$$

where $S =$ a priori probability that the n-bit code is the true sync code, and $p_g =$ bit error probability. This expression illustrates that increasing the code length reduces the probability of false sync, as would be expected. To illustrate, let us take a particular example of the average value of x, which is np_g (assumed to be an integer). Furthermore, let it be assumed that synchronization has been lost and the receiver is in the process of reacquiring sync ($S \ll 1$). When $x = np_g$ and $S \ll 1$,

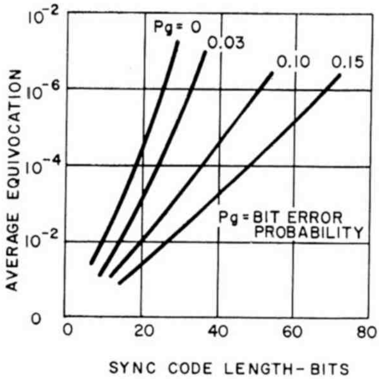

Fig. 6—Average equivocation, R_L, versus sync length in bits.

$$P(x) = \frac{1}{1 + S\ (p_{g0})^n}$$

where $p_{g0} = 2\ (p_g)^{p_g}\ (1 - p_g)^{1-p_g}$. The actual value of equivocation depends upon the amount of agreement between the digits received and those of the pattern expected. This value of $P(x)$ may be used to calculate the mean value of equivocation R_L,

$$R_L = P(x)\ \log_2 P(x) + [1 - P(x)]\ \log_2 [1 - P(x)].$$

Figure 6 shows the manner in which R_L varies with p_g and n.

Consider now the case of no transmission errors and let n_0 represent the code length when $p_g = 0$ and n represent the code length when $p_g \neq 0$. Then the ratio of these two code lengths is a measure of the increase in digits required when transmission errors are present. This ratio, given as $n/n_0 = 1/\log_2 p_{g0}$ (see Reference (3) for more details), is plotted in Figure 7. It illustrates the manner in which the number of digits must be increased in order to convey the same amount of information in the presence of errors.

ACKNOWLEDGMENT

The author wishes to thank D. W. Lytle for his helpful suggestions and review of the original manuscript, of which this paper is a summary.

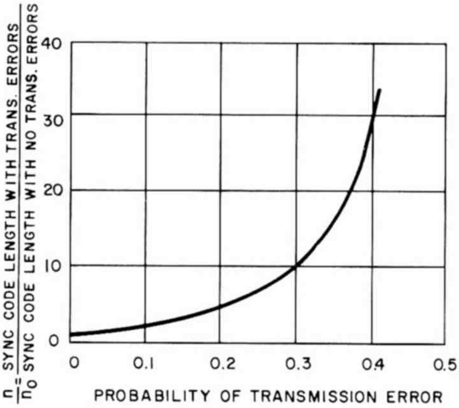

Fig. 7—Ratio n/n_0 versus p_g.

APPENDIX

Consider a binary sync pattern of length n that is inserted in independent data bits. Let

$n = r + s =$ length of sync pattern in bits

$r =$ number of ones in the sync pattern

$s =$ number of zeros in the sync pattern

$p =$ independent probability of a one in data bits

$q =$ independent probability of a zero $= 1 - p$

$e =$ number of errors allowed (by the pattern recognizer) in a sync pattern and still have it be recognized as a true pattern by the ground PCM terminal equipment

$P_f =$ probability that a group of n independent data bits be recognized as a sync pattern.

For $e = 0$, i.e., no errors allowed in the sync pattern, $P_{f0} = p^r q^s$.

For $e = 1$, i.e., one error allowed in the pattern, there are $\binom{n}{1}$ ways of one error and these can occur in two ways:

$$P_{f1} = s\, p^{r+1}\, q^{s-1} + r\, p^{r-1}\, q^{s+1}.$$

For $e = 2$, i.e., exactly two errors allowed in the pattern, there are $\binom{n}{2}$ ways of two errors and these can occur in three ways:

$$P_{f2} = \binom{s}{2}\, p^{r+2}\, q^{s-2} + \binom{r}{2} p^{r-2}\, q^{s+2} + rs\, p^r\, q^s.$$

Now, if *e or less* errors are allowed in the pattern detector, an extension of the above process yields the following double summation:

$$P_f = \sum_{j=0}^{e} \sum_{i=0}^{j} \binom{r}{j-1} \binom{s}{i} p^{r-j+2i}\, q^{s+j-2i}.$$

The probability of false sync P_f can now be used (see Reference (5)) as one quantity required to calculate the average number of frames to sync (M):

$$M = \frac{P_t}{P_c(1-P_t)} \left[\frac{1}{1-P_f} + \frac{1 - P_c \left(1 - \frac{1}{P_t}\right)}{1 - P_n} \right] \text{frames,}$$

The other quantities used in this equation are as follows. Defining p_g as bit error probability, P_c is the probability of recognizing a sync pattern,

$$P_c = \sum_{i=0}^{e} \binom{n}{i} p_g{}^i\, (1-p_g)^{n-i},$$

P_t is the probability of false sync decision in one frame,

$$P_t = \sum_{i=1}^{b} \binom{b}{i} P_f^{\,i} \, (1 - P_f)^{b-i},$$

P_n is the probability of no decision in first frame,

$$P_n = (1 - P_t)\,(1 - P_c).$$

REFERENCES

[1] A. Viterbi, *Coding Theory and Its Applications to Communication Systems,* JPL/CIT Technical Report Number 32-67, 31 March 1961.

[2] T. G. Birdsall and M. P. Ristenbatt, *Introduction to Linear Shift Register Generated Sequences,* The University of Michigan, Cooley Electronics Laboratory, Technical Report Number 90, Oct. 1958.

[3] R. H. Barker, "Group Synchronizing of Binary Digital Systems," *Communications Theory* (W. Jackson, Editor), Academic Press, Inc., pp. 273-287, 1953.

[4] J. Owen, *Handbook of Statistical Tables,* Addison and Wesley, p. 519.

[4a] J. L. Weblemoc and E. R. Hill, "Synchronization Methods for PCM Telemetry," *1961 National Telemetering Conference,* pp. 11-87.

[5] E. D. Bloedel, *Optimum Synchronization in the Presence of Biased PCM Data,* MSEE thesis, University of Washington, July 1965.

[6] G. Goode and J. Phillips, "Optimum PCM Frame Synchronization," *1961 National Telemetering Conference,* pp. 11-15.

[7] M. W. Willard, "Mean Time to Establish PCM Synchronization," *1963 National Telemetering Conference.*

[8] G. E. Goode, "A New Method of Frame Synchronization Using Linear Sequential Feedback Generators," *1963 National Telemetering Conference,* pp. 3-4.

[9] E. R. Hill, "Techniques for Synchronizing Pulse-Code-Modulated Telemetry," *1963 National Telemetering Conference,* pp. 3-3.

CORRECTIONS

[1] In the paper, "Response of Low-Power Nuvistors to Pulsed Nuclear Radiation," by I. F. Stacy and F. J. Feyder, the text on page 413 gives gamma exposure rates in units of gamma/sec, when they should be given as roentgen/sec. Also, the headings in Table I on page 413 should be corrected as follows:

Table I—Effects of Grid-Resistor Type and Value

Operation	Distance from Shroud	Heater Voltage	Max. Shift in DC Plate Current Level (milliamperes) Metal-film 1 megohm	Carbon 1 megohm	Carbon 100,000 ohms
Dynamic	0	6.3	3.2	3.5	1.3
Dynamic	0	6.3	3.1	3.4	1.3
Dynamic	0	6.3	3.2	3.6	2.1
Static	0	6.3	5.7	6.8	2.4

2. On page 382 of the September 1966 issue of *RCA Review,* the curve given in Figure 5 of the paper, "Measurements on the Properties of Microstrip Transmission Lines for Microwave Integrated Circuits," by M. Caulton, J. J. Hughes, and H. Sobol, has been incorrectly plotted. The corrected figure is shown below.

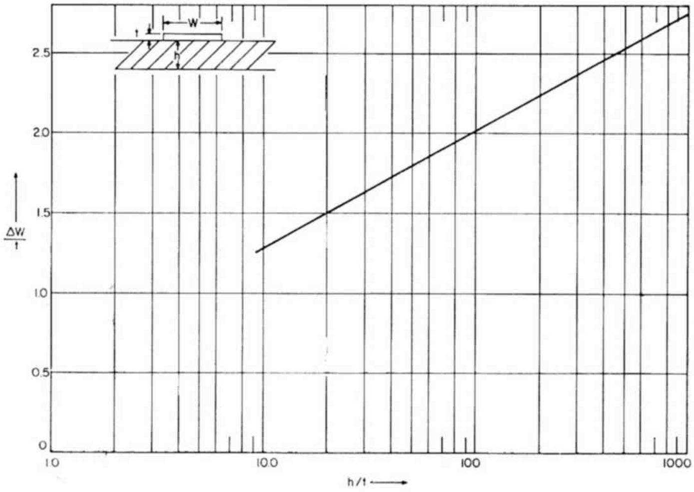

FIG. 5

Fig. 5—Line-width correction for finite-thickness substrates.

RCA Technical Papers

Third Quarter, 1966

Any request of copies of papers listed herein should be addressed to the publication to which credited.

"Automatic Display of C-V Curves for Metal-Insulator-Semiconductor (MIS) Structures," K. H. Zaininger, *Proc. IEEE* (Letters) (July) 1966

"Characteristics of Waveguides with a Semiconductor Side Wall," R. D. Larrabee, *Trans. IEEE PTGMTT* (July) 1966

"A Comparison of Color TV Cameras for NTSC and PAL Color Standards," A. H. Lind, *Trans. IEEE PTGBTR* (July) 1966

"Decoration of Semiconductor Surfaces for Electron Microscopy by Displacement Deposition of Gold," M. D. Coutts and A. G. Revesz, *Jour. Appl. Phys.* (July) 1966

"Design of Comb-Line Band-Pass Filters," R. M. Kurzrok, *Trans. IEEE PTGMTT* (Correspondence) (July) 1966

"A Developmental 15-Inch Transistorized Color Receiver," W. E. Babcock, *Trans. IEEE PTGBTR* (July) 1966

"Electromagnetic Behavior of Thin-Film Structures," J. Pearl, *Jour. Appl. Phys.* (July) 1966

"Integrated Circuits in Television Receivers," J. Avins, *Trans. IEEE PTGBTR* (July) 1966

"Integration of Technical Facilities in Black-and-White and Color TV Programming," E. P. Bertero, *Jour. SMPTE* (July) 1966

"Introduction to a Panel Discussion of Color Television Systems," C. J. Hirsch, *Trans. IEEE PTGBTR* (July) 1966

"Performance of Room Temperature GaAs Lasers at High Pulse Repetition Rates (50 kc/s)," G. C. Dousmanis and H. E. Gross, *Proc. IEEE* (Letters) (July) 1966

"On 'Secant Correction for Tracking Pedestals,'" R. F. Wood, Jr., *Trans. IEEE PTGAC* (Correspondence) (July) 1966

"Taxonomy of Electric Charges in Metal-Insulator-Semiconductor Systems," A. G. Revesz, *Proc. IEEE* (Letters) (July) 1966

"Total Value Concepts in the Contract Definition Phase," S. Robinson, *Trans. IEEE PTGAES* (July) 1966

"Tunnel Diodes," R. M. Minton, *Electronics World* (July) 1966

"Conductivity and Crystal Phase Change in Phthalocyanines," S. E. Harrison and K. H. Ludewig, *Jour. Chem. Phys.* (1 July) ... 1966

"Messages Sent in Symbols Will Link Multilingual Troops," H. R. Gutsmuth, *Electronics* (July 25) 1966

"Determination of Deep Centers in Conducting Gallium Arsenide," R. Williams, *Jour. Appl. Phys.* (August)	1966
"Effect of Neutron-Induced Defects on the Current-Carrying Behavior of Vapor-Deposited Niobium Stannide," G. W. Cullen and R. L. Novak, *Jour. Appl. Phys.* (August)	1966
"Experimental Demonstration and Theory of a Corrective to Second Breakdown in Si Power Transistors," D. Stolnitz, *Trans. IEEE PTGED* (August/September)	1966
"Origin of Metric Prefixes," S. M. Sherman, *IEEE Spectrum* (Tech. Corresp.) (August)	1966
"Photoemission of Electrons from Metals into Silicon Dioxide," A. M. Goodman and J. J. O'Neill, Jr., *Jour. Appl. Phys.* (August)	1966
"Paramagnetic-Resonance Absorption in the Optically Populated State $^2F_{5/2},E_{5/2}$ of Tm^{2+} in CaF_2," E. S. Sabisky and C. H. Anderson, *Phys. Rev.* (5 August)	1966
"Integrated Circuits Make a Low-Cost F-M Receiver," R. L. Sanquini, *Electronics* (August 8)	1966
"Electrical and Optical Properties of High-Resistivity Gallium Phosphide," B. Goldstein and S. S. Perlman, *Phys. Rev.* (12 August)	1966
"Direct Observation of Lithium-Defect Interaction in Silicon by Electron Paramagnetic Resonance Measurements," B. Goldstein, *Phys. Rev. Letters* (22 August)	1966
"Analysis of Multiple-Signal FM Detection System," T. Murakami, *RCA Review* (September)	1966
"Automatic Display of MIS Capacitance Versus Bias Characteristics," K. H. Zaininger, *RCA Review* (September)	1966
"Automatic Plotting of Conductance and Capacitance of Metal-Insulator-Semiconductor Diodes or Any Two Terminal Complex Admittance," J. Shewchun and A. Waxman, *Rev. Sci. Instr.* (September)	1966
"Avalanche and Tunneling Currents in Gallium Arsenide," R. Williams, *RCA Review* (September)	1966
"Can Traveling-Wave Tubes Be Scaled?," M. J. Schindler, *Microwave Jour.* (September)	1966
"A Comparison of the Theoretical and Observed Cutoff Frequency of High Voltage GaAs Varactors," G. Kupsky, *Proc. IEEE* (Letters) (September)	1966
"Designing Silicon-Transistor Hi-Fi Amplifiers, Pt. 1. Performance Objectives," R. D. Gold and J. C. Sondermeyer, *Electronics World* (September)	1966
"Efficiency of Complex Projects," H. B. Brooks, *Trans. IEEE PTGEM* (September)	1966
"Efficiency vs. Size of Research Teams," J. T. Wallmark and Coauthor, *Trans. IEEE PTGEM* (September)	1966
"Efficient Sequential Detection in the Presence of Strong Localized Signal Interference," H. M. Finn and R. S. Johnson, *RCA Review* (September)	1966
"Gallium-Arsenide Electro-Optic Modulators," T. E. Walsh, *RCA Review* (September)	1966
"A Magnetostrictive Device for Use in Scanning," T. N. Chin, *Proc. IEEE* (Letters) (September)	1966
"Measurements on the Properties of Microstrip Transmission Lines for Microwave Integrated Circuits," M. Caulton, J. J. Hughes, and H. Sobol, *RCA Review* (September)	1966
"Response of Low-Power Nuvistors to Pulsed Nuclear Radiation," I. F. Stacy and F. J. Feyder, *RCA Review* (September)	1966
"A Theorem for Generating the Inverse Integral Transform Given Its Direct Transform," A. A. Wolf, *Trans. IEEE PTGAES* (Correspondence) (September)	1966

"Three-Wire Cryoelectric Memory Systems," A. R. Sass, E. M. Nagle, L. L. Burns, *Trans. IEEE PTGMAG* (September) 1966

"Use of Superconductors with Varied Characteristics for Optimized Design of Large-Bore High-Field Magnets," E. R. Schrader and P. A. Thompson, *Trans. IEEE PTGMAG* (September) .. 1966

"Vidicon Performance in Extreme Thermal Environments," R. E. Johnson, *RCA Review* (September) 1966

"Electron Paramagnetic Resonance and Electrical Properties of the Dominant Paramagnetic Defect in Electron-Irradiated p-Type Silicon," N. Almeleh and B. Goldstein, *Phys. Rev.* (16 September) 1966

"Enhancement of Superconductivity in Metal Films," B. Abeles, R. W. Cohen, and G. W. Cullen, *Phys. Rev. Letters* (19 September) 1966

AUTHORS

A. Acampora (See *RCA Review*, Vol. XXVII, June 1966, p. 318.)

E. D. **Bloedel** received the B.S. degree in Engineering Physics at Portland University in 1960, and the M.S.E.E. from University of Washington in 1965. From 1960 to 1962 he was associated with the General Electric Company in Syracuse, N. Y., where he was engaged in microelectronic research and radar system analysis. From 1962 to 1965 he was a staff engineer with the Boeing Company, Seattle, Wash., responsible for system analysis of homing and command guidance, telemetry, and communication systems. Mr. Bloedel joined RCA in 1965 and is presently assigned to the TRADEX Radar facility on Kwajalein Island.

John T. **Frankle** received the BSEE degree from the Massachusetts Institute of Technology in June 1958 and the MSEE degree from the Polytechnic Institute of Brooklyn in June 1962. In the summer of 1957 he worked as a Junior Engineer in the Electronics Division of Curtiss-Wright Corporation on the development of an airborne radar simulator. He was appointed a Teaching Fellow at the Polytechnic Institute of Brooklyn in 1958 and a Graduate Research Assistant at the Microwave Research Institute (M.R.I.) of the Polytechnic in 1959. While there, he performed basic research in FM and FM noise. Mr. Frankle joined RCA's Communications Systems Division in 1960 where he has been involved in many diverse programs. Among these are studies of the spectra and extraction of timing information from random digital signals, the RCA Diphase Data Modem, and FM threshold improvement techniques.

Mr. Frankle is a member of the Institute of Electrical and Electronic Engineers.

F. H. Lefrak received the AB degree in 1957 and the MS degree in 1959 from Columbia University in physics and electrical engineering, respectively. He joined RCA Laboratories, Princeton, N. J., in 1959 and transferred to RCA Communications Systems Division in 1963. Since 1963, he has devoted most of his time to advanced analog communication techniques, particularly FM threshold extension. He has worked on the design and development of a 600-channel FDM solid-state phase-locked demodulator, a microwave phase-locked FM exciter, a 240-channel FMFB demodulator, the FM feedback demodulator for the Lunar Orbiter ground station, and, presently, a 60-600 channel FM demodulator for the Communications Satellite Corp. Mr. Lefrak is a member of the Institute of Electrical and Electronics Engineers and of Eta Kappa Nu.

Harold A. Moore obtained the degree of BSEE from Michigan State University in 1929. After graduation he joined the RCA Communications Research Group at Riverhead, Long Island. For the next ten years Mr. Moore was actively engaged in the design, development, and testing program for the RCA commercial diversity receiver. He was involved in many areas of work in long range HF radio-propagation studies, earth current measurements, rhombic and fishbone antenna characteristics, multipath-jitter measurements, long RF transmission-line phase shift, HF-oscillator stabilization and frequency-measuring equipment. In 1961 he transferred to the RCA Communications Systems Division, where he is currently working in several programs, including the AN/PRC-25 test program, solid-state radio-relay techniques program, and the Lunar Orbiter Satellite FMFB demodulator program, for which he developed a high-sensitivity and very linear voltage-controlled oscillator.

Mr. Moore is a member of the Institute of Electrical and Electronics Engineers.

Arnold Newton received a diploma from the Mathematics-Physics Lyceum, Krakow, Poland in 1941, completed the T-3 course at the RCA Institutes, and did graduate work at the City College of New York in 1963. He joined RCA Industry Service Laboratories in 1944, where he worked on circuits for projection-television receivers until 1947. He subsequently held engineering positions with Polytechnic Research and Development Co., FXR and Polarad Electronics Corp. Mr. Newton returned to RCA, Communications Systems Division, in 1958, where he engaged in the study and development of Electronic Counter Measures systems. He was appointed Group Leader in 1961 with responsibility for several projects that led to the development of FMFB and phase-locked demodulators for 120 and 600 channels, respectively. He was also in charge of the Lunar-Orbiter Ground Station demodulator program, threshold improvement program for tactical radio and tropo sets, and an Advanced ECCM program for the Signal Corps. He is currently in charge of the 600-channel modulator-demodulator program for the Communication Satellite Corp.

Mr. Newton is a Senior Member of the Institute of Electrical and Electronics Engineers and Member of AAAS.

LAIMONS OZOLINS obtained the EE Degree in 1931 from the University of Latvia. From 1932-1949, in Europe, he did design and development work on broadcast, power-transmitting, receiving, and test equipments, and on audio systems. He joined the Reiner Electronics Co., New York City, in 1950. From 1952-1956, he worked at Elsin Electronics Co., New York City. Mr. Ozolins joined RCA in 1956, where he has had project responsibilities in a variety of programs, including a time-division data link employing FM modulation and detection, wide-frequency-range universal ECM system, investigation of FDM intermodulation distortion in solid-state systems, development work on a microwave FM system based on the phase-lock principle, and the Lunar Orbiter Satellite program.

EDWARD G. RAMBERG received the A.B. degree from Cornell University in 1928 and the Ph.D. degree in theoretical physics from the University of Munich in 1932. After working on the theory of x-ray spectra as research assistant at Cornell, he joined the Electronic Research Laboratory of the RCA Manufacturing Company in Camden in 1935. He has been associated with the RCA Laboratories in Princeton since their establishment in 1942. He has worked primarily on electron optics as applied to electron microscopy and television, various phases of physical electronics, thermoelectricity, and optics. In 1949 he was visiting professor in physics at the University of Munich and, in 1960 and 1961 Fulbright Lecturer at the Technische Hochschule, Darmstadt.

Dr. Ramberg is a Fellow of the Institute of Radio Engineers and the American Physical Society and a member of Sigma Xi and the Electron Microscope Society of America.

A. ROSE (See *RCA Review*, Vol. XXVII, March 1966, p. 174.)

FRED STERZER received the B.S. degree in physics from the College of the City of New York in 1951, and the M.S. and Ph.D. degrees in physics from New York University in 1952 and 1955, respectively. From 1952 to 1953 he was employed by the Allied Control Corporation, New York, New York. During 1953 and 1954 he was an instructor in physics at the Newark College of Engineering, Newark, New Jersey, and a research assistant at New York University. He joined the RCA Electron Tube Division in Harrison, New Jersey, in October, 1954, and transferred to the Princeton, New Jersey branch in 1956, where he is now Manager of the Microwave Applied Research Group. His work has been in the field of microwave spectroscopy, microwave tubes, parametric amplifiers, tunnel-diode microwave amplifiers, frequency converters and oscillators, microwave computing circuits, and light modulators and demodulators.

Dr. Sterzer is a member of Phi Beta Kappa, Sigma Xi, the American Physical Society, and the Institute of Electrical and Electronics Engineers.

RCA REVIEW

a technical journal

INDEX

VOLUME XXVII

TABLE OF CONTENTS

March

June

September

December

AUTHORS, VOLUME XXVII